DNA Directed Self-Assembly of Carbon Nanotube Structures

Thesis by

Si-ping Han

In Partial Fulfillment of the Requirements

for the Degree of

Doctor of Philosophy

California Institute of Technology

Pasadena, California, USA

2011

(Defended August 13, 2010)

For my family,

Who has been there for me as only family can.

For Jackie,

Who has brought me more happiness than I can imagine.

For Bill Goddard,

Who taught me to appreciate the dance of electrons, atoms and molecules.

Acknowledgements

Robert Barish and Hareem Maune have not only been wonderful colleagues but also wonderful friends. Without them I would not have stepped away from my computer to undertake actual experiments.

Paul Rothemund, Marc Bockrath, and Erik Winfree have been great sources of advice, feedback and inspiration.

I've been a frequent visitor to the Winfree lab for the past three and half years, taking up a bench, the PCR machines, and especially, the AFM. This would not have been possible if it wasn't for the generosity and friendship of all the members of the Winfree and Rothemund labs, who made the lab feel like a home away from home. I especially appreciate the many fruitful discussions with Rizal Hariadi, and Sungwook Woo and Karolyn Knolls' tireless resolution of problems large and small.

Many summers ago, Julie Norville came to me to talk about using DNA to assemble carbon nanotubes. Before that I had not been very interested in DNA or carbon nanotubes. Those ideas have come a long way but I owe her a debt of gratitude for the initial seed.

I'd like to thank the fellow members of the Goddard group for giving a great deal of support, advice and assistance of all manners. Shirley Feng, has been indispensible as our group administrator and provider of solutions. Tahir Cagin, Alejandro Strachan and Adri van Duin were wonderful teachers who taught me how to do molecular simulation. I enjoyed many stimulating discussions Tod Pascal, and Ravinder Abrol. Yvonne Goddard has been a wonderful and gracious host and it's always been a pleasure to see her at our annual group banquet.

Brent Fultz has been a warm and open minded option representative for Material Science who has lent me a hand at the crucial stages in my graduate career and I owe him a debt of gratitude.

Finally, none of this would be possible without Bill Goddard, the best advisor and mentor I could possibly ask for.

Abstract

Production of pure carbon nanotube species and organization of nanoscale structure are two fundamental barriers to the utilization of CNTs in nanoelectronics. We have developed new methods to characterize double walled carbon nanotube (DWNT) structure by Raman spectroscopy and organize single walled carbon nanotube (SWNT) constructs using DNA.

First, using atomistic force fields calculations, we have shown that the radial breathing modes (RBM) of double walled carbon nanotubes can be accurately modeled as two uniform concentric cylindrical elastic shells coupled by a van der Waals interaction. This model leads to a simple equation which can be solved to give accurate RBMs (given diameters) or diameters (given RBMs).

Secondly, we have developed a method for using DNA origami to template the assembly of complex SWNT structures. In this process, SWNTs are modified with non-covalently attached DNA linkers that present duplex labeling domains for base pairing to complementary single stranded hooks on customized DNA origami. We show that the SWNTs attach at positions and in orientations specified by their labeling sequence, and that nanotube cross-junctions assembled from two different SWNTs in this manner can behave as field effect transistors.

Finally, we have devised a method for using DNA linkers to organize arrays of parallel SWNTs with uniform and selectable inter-nanotube separation of <20 nm. SWNTs are first dispersed in aqueous solution with DNA linkers-spacers that non-covalently anchor onto their sidewalls. When the modified SWNTs are then deposited on mica or polar lipid bilayers and allowed to diffuse *on the surface*, they form parallel

arrays of SWNTs in which different domains of the DNA linker-spacers act to maintain array cohesion and enforce uniform separation. Thus, the use of 7 bp, 20 bp, and 60 bp DNA spacer domains result in ~3 nm, ~8.5 nm, and ~22 nm inter-nanotube separations. We further use the spacer domains as rigid scaffolds for the positioning of Streptavidin proteins between adjacent nanotubes, and give a simple method for transfer of intact arrays onto adhesive glass substrates. Further development of this technology could lead to wafer scale organization of dense parallel SWNT decorated with heterogeneous nanoscale objects.

Table of Contents

Page

Figures and Tables

Page

Chapter 1

Chapter 2

Chapter 2S

Chapter 3

Chapter 1

Coupling of Raman Radial Breathing Modes in Double Wall Carbon Nanotubes and Bundles of nanotubes

The chapter was adapted from the following paper with William A. Goddard III

Han SP, Goddard WA, *J. Phys. Chem. B* **113** (20) 7199-7204 (**2009**)

1.1 Abstract

Measurements of the radial breathing modes from Raman Spectroscopy have been most useful in characterizing the diameters of single-wall carbon nanotubes (SWNT), where there is a simple monotonic relationship between frequency and diameter. Similar correlations have also been used to predict sizes for double and multiple wall nanotubes and for bundles of SWNT. However this can lead to significant errors because the relationship between frequencies and diameter is much more complicated for DWNT. This is because of couplings between the vibrations of various walls. To provide guidance in such assignments we used the GraFF atomistic force field to predict the in-phase and counter-phase radial breathing modes (RBMs) of double wall carbon nanotubes (DWNTs) over a broad range of inner and outer diameters and chiralities. We then developed an analytical model to describe the RBMs of dispersed DWNTs. This enables the inner and outer shell diameters to be extracted from pairs of RBM peaks. We find that nanotubes bundles show significant dependent peak broadening and shifting compared to dispersed nanotubes. For bundles of SWNT and DWNT, the relationships are much more complicated

1.2 Introduction

High quality double wall carbon nanotubes (DWNT) can now be produced in quantity using catalytic chemical vapor deposition[1], arc discharge[2], and a variety of other methods[3]. The unique two layer structure of DWNTs confers advantages such as defect free inner shells[9], and better field emission properties than single and multi-wall carbon nanotubes[4]. Recent density functional theory calculations suggest that, for small diameter DWNTs with closely spaced shells, inter-shell electronic structure coupling

could lead a pair of semiconducting shells to act collectively as a single metallic wire. Thus, it may be possible to produce uniformly metallic DWNTs by constraining diameter[5].

Further development of DWNTs' technological potential would benefit from better characterization of their inner and outer chiralities and diameters. A commonly used and relatively simple method for diameter characterization is assignment based on the radial breathing mode (RBM) peaks in the Raman spectra. However, for DWNT, calculations show that when the inter-shell separation approaches the graphite inter-layer distance (~ 3.4 Å [10]) the inner and outer walls interact to split the RBMs. Thus the common assumption that each shell in a DWNT vibrates independently with the RBM appearing at the same places as for the corresponding single wall carbon nanotube (SWNT) produces systematic errors

To predict the RBM for DWNTs, we have used atomistic force field simulations to map the in-phase and counter-phase RBMs of dispersed individual commensurate and incommensurate DWNTs over a broad range of inner and outer diameters and chiralities. We find that a continuum model treating the DWNT as two concentric uniform elastic shells coupled by a van der Waals force [7] accurately fits our results using four free parameters. This simple formulation allows rapid solutions for both the forward problem of calculating RBMs from given diameters and the inverse problem of getting diameters from pairs of given RBMs. (A simple Python script for doing these calculations is included in the supplementary materials). Since many DWNT samples are probed in a form where the nanotubes are bundled, we also simulated homogeneous DWNT bundles, which showed diameter dependent broadening and shift of RBM peaks from those of

individual nanotubes due to inter-nanotube dispersive coupling. Collectively, our results should enable more accurate interpretation of RBM data for DWNTs.

1.3 Definitions

In this paper, we will refer to the chirality of the inner wall as (n_i, m_i) and that of the outer wall as (n_o, m_o). We define the inner (d_i) and outer (d_o) diameters as the diameters of the imaginary cylindrical shells drawn through the centers of the carbon atoms in the inner and outer walls. The separation between the inner and outer shells is $\Delta = \frac{d_o - d_i}{2}$. To good approximation, the diameter of each shell, d, is determined by its chirality: $d = c\sqrt{n^2 + m^2 + n*m}$ where c is the C-C equilibrium bond distance in graphene. For $\Delta < 3.0$ Å, our simulations show that repulsion between the inner and outer shells distorts C-C bond distances, leading d_i and d_o to deviate slightly from the simple relation given above.

1.4 Simulation of carbon nanotubes

All carbon nanotubes were simulated in vacuum using an atomistic graphite force field. [6] This force field provides a simplified model of SP2 carbon bond energies as a function of atom center positions. It has a Morse type potential for bond stretches, cosine type potential for the angles between adjacent bonds, and two fold torsion terms. In addition, it has a Lennard-Jones 12-6 expression for the van der Waals energy. [6] Although the force field does not explicitly describe electronic wavefunctions, its accurate prediction of the properties of C60 and C70 fullerene crystal[6] establishes confidence for the accurate description of DWNT properties. In particular, it should give

accurate geometries, energies, elastic constants and inter-shell rotational and translational barriers for both large and small diameter DWNTs.

Optimal geometries for carbon nanotubes were obtained by energy and force minimization resulting in C-C bond distances of approximately 1.43 Å. The enthalpy of formation of a (10,10) SWNT was 2.50 kcal/(mole atoms) when compared to graphite. The vibrational normal modes of nanotubes were calculated from optimized geometries by diagonalization of the systems' Hessians. The (10,10) SWNT's radial breathing mode in vacuum was 173.15 cm^{-1}.

As a test, we calculated the RBMs of individual SWNTs. These modes obey the following equation:

$$f = \frac{a}{diameter} + b \qquad \textbf{(1)}$$

Fitting of a and b using thirty-four armchair, zigzag, and chiral SWNTs gave $a = 237.5\ cm^{-1}$ and $b = 0.0\ cm^{-1}$. Data plotted in figure 1 shows that our values for a and b lie between experimental results for individual SWNTs dispersed on SiO_2 substrate ($a = 248\ cm^{-1}$ and $b = 0.0\ cm^{-1}$)[12] and those dispersed in fluid with sodium dodecyl sulfate surfactant ($a = 223.5\ cm^{-1}$ and $b = 13.5\ cm^{-1}$)[11]. Therefore, there is good agreement between experimental values and our calculations.

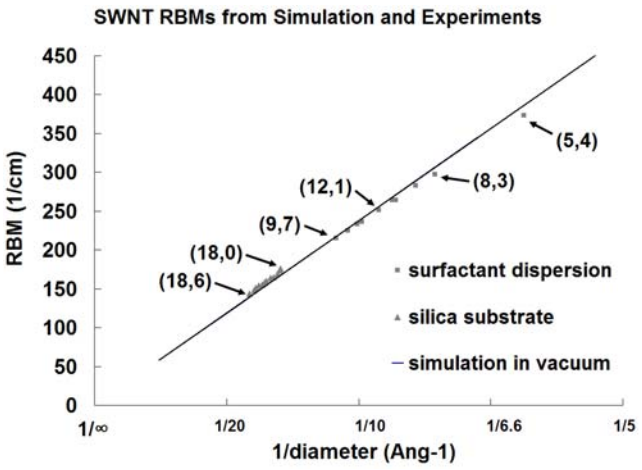

Figure 1. Comparison of the experimentally observed RBMs data for SWNTs of various chiralities with diameter. The diameters are calculated from the reported chiralities using the simple formula $d = a*(m^2 + n^2 + m*n)^{1/2}$. The black line is the best fit to the results of our atomistic simulations. There is good agreement between our calculations and experimental data.

Commensurate zigzag DWNTs with $(n_i,0)$ inner and $(n_o,0)$ outer shells were constructed with $n_i = 10, 15, 20$ and $n_o=n_i+5$ *to* n_i+13. This allowed fine grained sampling of the range of diameters and separations obtained from selective synthesis methods while minimizing the number of atoms in the unit cell. Each nanotube was periodic in the axial direction and effectively isolated in the transverse directions. Optimal geometries were again obtained by force and energy minimization. A comparison of inner and outer shell diameters to corresponding SWNT diameters showed that the change in diameter due to inter-shell coupling was less than 1 % for $\Delta > 3.1$ Å, and approximately 2% for 3.0 Å $\leq \Delta \leq$ 3.1 Å. DWNTs with $d_i \leq 10$ Å were more distorted than those with larger inner diameters. For incommensurate DWNTs, unit cells were lengthened until the length mismatch between the inner and outer shells was less than 1%.

In-phase and counter-phase RBMs for our DW NT models are plotted in figure 2. They show that, for $\Delta < 3.7$ Å, there was significant deviation of both types of RBMs from the RBMs of cor responding SW NTs. For exam ple, the (15,0)@(23,0) nanotube with $\Delta = 3.22$ Å had an in-phase RBM of 146.03 c m^{-1} and a counter-phase mode of 235.11 cm^{-1}. On the other hand, the (23,0) SWNT's RBM was 130.51 cm^{-1} and the (15,0) SWNT's RBM was 199.31 cm^{-1}.

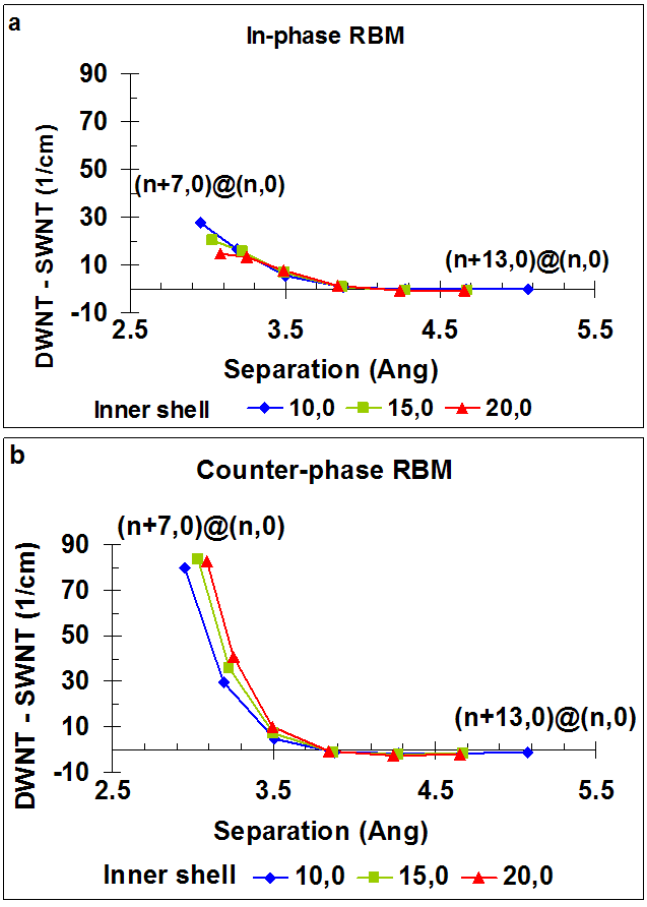

Figure 2. 2a shows the di fference when the RBM o f the outer sh ell's corresponding SWNT is subtracted from the in-phase R BM of a DWNT. 2b shows the difference w hen the inner shell SWNT RBM is subtracted from the counter-phase DWNT RBM.

1.5 Analytical model of DWNTs

Our simulations show that the distortion of bond lengths in the outer shell is minimal (Supplementary Table 1), and cannot account for the calculated change in the RBM frequencies. Therefore, van der Waals coupling is the main cause for the RBM shift. A question then arises. For nanotubes with similar inner and outer diameters, does RBM depend on the chiralities of each shell? Since experimental studies have shown that the friction between concentric shells of multi-wall carbon nanotubes should be small[13] and that there is no correlation between the chiralities of the inner and outer shells in a DWNT[15], we assumed that the chiralities were unimportant, and constructed the continuum model for the DWNT as two concentric smooth cylindrical elastic shells with homogeneous mass density and van der Waals interaction density. Using this model, we derived functions for calculating the RBMs using d_i and d_o as input. A subsequent review of the literature showed that Wu, Zhou, and Dong had reported a similar model[7]. Here, we briefly explain our derivation.

We can write the following eigenvalue equations for the normal modes of the coupled shells in mass weighed coordinates.

$$\begin{pmatrix} \dfrac{k_{ii}}{m_i} & \dfrac{k_{io}}{\sqrt{m_i}\sqrt{m_o}} \\ \dfrac{k_{oi}}{\sqrt{m_o}\sqrt{m_i}} & \dfrac{k_{oo}}{m_o} \end{pmatrix} \begin{pmatrix} \dfrac{r_i}{\sqrt{m_i}} \\ \dfrac{r_o}{\sqrt{m_o}} \end{pmatrix} = -\omega^2 \begin{pmatrix} \dfrac{r_i}{\sqrt{m_i}} \\ \dfrac{r_o}{\sqrt{m_o}} \end{pmatrix} \qquad \textbf{(2a)}$$

Where r_i and r_o are the radii and m_i and m_o the masses per unit length of the inner and outer shells. This has solutions

$$\omega_-^2 = \alpha - \beta$$
$$\omega_+^2 = \alpha + \beta$$
$$\alpha = \frac{1}{2}\left(\frac{k_{oo}}{m_o} + \frac{k_{ii}}{m_i}\right) \qquad \textbf{(2b)}$$
$$\beta = \frac{\sqrt{4(k_{io}k_{oi} - k_{ii}k_{oo})m_i m_o + (k_{oo}m_i + k_{ii}m_o)^2}}{2m_i m_o}$$

ω_- is the in-phase RBM with lower frequency and ω_+ is the counter-phase RBM with higher frequency.

The potential energy of the nanotube is just the energies of the corresponding SWNTs plus the van der Waals coupling. We can thus separate each elastic constant k_{xy} into components due to the inherent elasticity of the inner and outer shells and components due to van der Waals coupling.

$$k_{ii} = m_i \omega_i^{\,2} + \frac{\partial^2 E_{vdW}}{\partial r_i^{\,2}}$$
$$k_{oo} = m_o \omega_o^{\,2} + \frac{\partial^2 E_{vdW}}{\partial r_o^{\,2}}$$
$$k_{oi} = k_{io} = \frac{\partial^2 E_{vdW}}{\partial r_o \partial r_i} \qquad \textbf{(2c)}$$
$$\omega_i = \frac{a}{2 * r_i} + b$$
$$\omega_{oi} = \frac{a}{2 * r_o} + b$$

ω_i and ω_o are the RBM frequencies of SWNT corresponding to the inner and outer shells. The ir free parameters a and b are already determined by fitting to our SWNT RBM calculations. The mass per unit length m_i and m_o of the inner and outer shells are

$$m_i = 2\pi R_i \rho$$
$$m_o = 2\pi R_o \rho \qquad \textbf{(2d)}$$

where R_i and R_o are the relaxed radii of the inner and outer shells and ρ is a constant mass density.

Raman spectra are given in wavenumbers with units of cm^{-1}. One can trivially convert between frequencies and wavenumbers using the relationship

$$w = \frac{1}{\lambda} = \frac{\omega}{c_o} \quad \textbf{(2e)}$$

where c_o is the speed of light in vacuum.

The van der Waals interaction energy E_{vdW} is calculated by integrating a Lennard-Jones expression over the two shells in cylindrical coordinates. The radial symmetry of the system gives a simplified expression:

$$E_{vdW} = \frac{N_i N_o}{2\pi}\int_0^{2\pi}\int_{-\infty}^{\infty} LJ\, dl_o\, d\theta_i$$
$$LJ = \varepsilon\left[\left(\frac{\alpha}{R}\right)^{12} - 2\left(\frac{\alpha}{R}\right)^{6}\right] \qquad \textbf{(3a)}$$
$$R = \left|\sqrt{l_i^2 + r_i^2 + r_o^2 - 2r_i r_o Cos(\theta_i)}\right|$$

where N_i and N_o are the numbers of atoms per unit length in the inner and outer shells, α is the distance at which $LJ = 0$ and ε is the van der Waals well depth. Direct integration of LJ yields a closed form expression for E_{vdw}.

$$E_{vdW} = \frac{N_i N_o \varepsilon \alpha^6}{640(r_i - r_o)^{10}(r_i + r_o)^9} *$$
$$\{-8(r_i - r_o)^2[-40(r_i^2 - r_o^2)^6 + \alpha^6(r_i^2 + r_o^2)(31r_i^4 + 194r_i^2 r_o^2 + 31r_o^4)] * K\left(\frac{4r_i r_o}{(r_i + r_o)^2}\right) +$$
$$[-1280(r_i - r_o)^6(r_i + r_o) + \alpha^6(563r_i^8 + 7604r_i^6 r_o^2 + 16434r_i^4 r_o^4 + 7604r_i^2 r_o^6 + 563r_o^8)] *$$
$$E\left(\frac{4r_i r_o}{(r_i + r_o)^2}\right)\}$$

(3b)

Where $E(\frac{4r_i r_o}{(r_i+r_o)^2})$ is the complete elliptic integral, and $K(\frac{4r_i r_o}{(r_i+r_o)^2})$ is the complete elliptic integral of the first kind. Substituting the results of 3b into 2b thus gives a complicated closed form expression for the two RBMs (see supplementary materials). This expression has four free parameters, *a, b, α,* and ε. Since *a* and *b* are predetermined by fitting to SWNT data, only *α,* and ε are truly free. To find their optimal values, we used Nelder-Mead type numerical optimization to minimize the squared difference between the calculated RBMs and the simulated RBMs for zigzag DWNTs. This gave α*=3.742 Å*, and ε *=0.09090 kcal/mole*. For comparison, the *LJ* parameters for the atomistic graphite force field are α*=3.8050 Å* and ε *=0.0692 kcal/mole.* Our parameters differ from the force field's because the uniform surface used in the continuum model does not have atom centers placed in positions that minimize the van der Waals energy.

1.6 Comparison between atomistic and analytical models

Figure 3 compares RBMs calculated using the optimized analytical expression with RBMs calculated using atomistic simulations. For all zigzag, armchair, and incommensurate DWNTs in this data set, the difference between the atomistic and analytical counter-phase frequencies is ~ 1% or less. The errors for most in-phase frequencies are also less than 1% (Supplemental Table 2). However, errors are over 2% for the (5,0)@(12,0), (5,0)@(13,0), and (10, 0)@(17,0) DWNTs. In these nanotubes, greater distortion of the inner and outer shells from their SWNT geometries (Supplemental Table 1) and the greater importance of atomic granularity due to smaller numbers of atoms and closer inter-shell separation contribute to greater systematic error. In general, we expect the analytical model to be accurate for DWNTs with inter-shell

separation greater than ~3.0 Å but sm aller than ~ 6 Å. At large r inter-shell separations, the inner nanotube m ay move to m ake better van der W aals contact with a portion of the outer nanotube, thus destroying the concen tric cylind rical sym metry assum ed f or the present model.

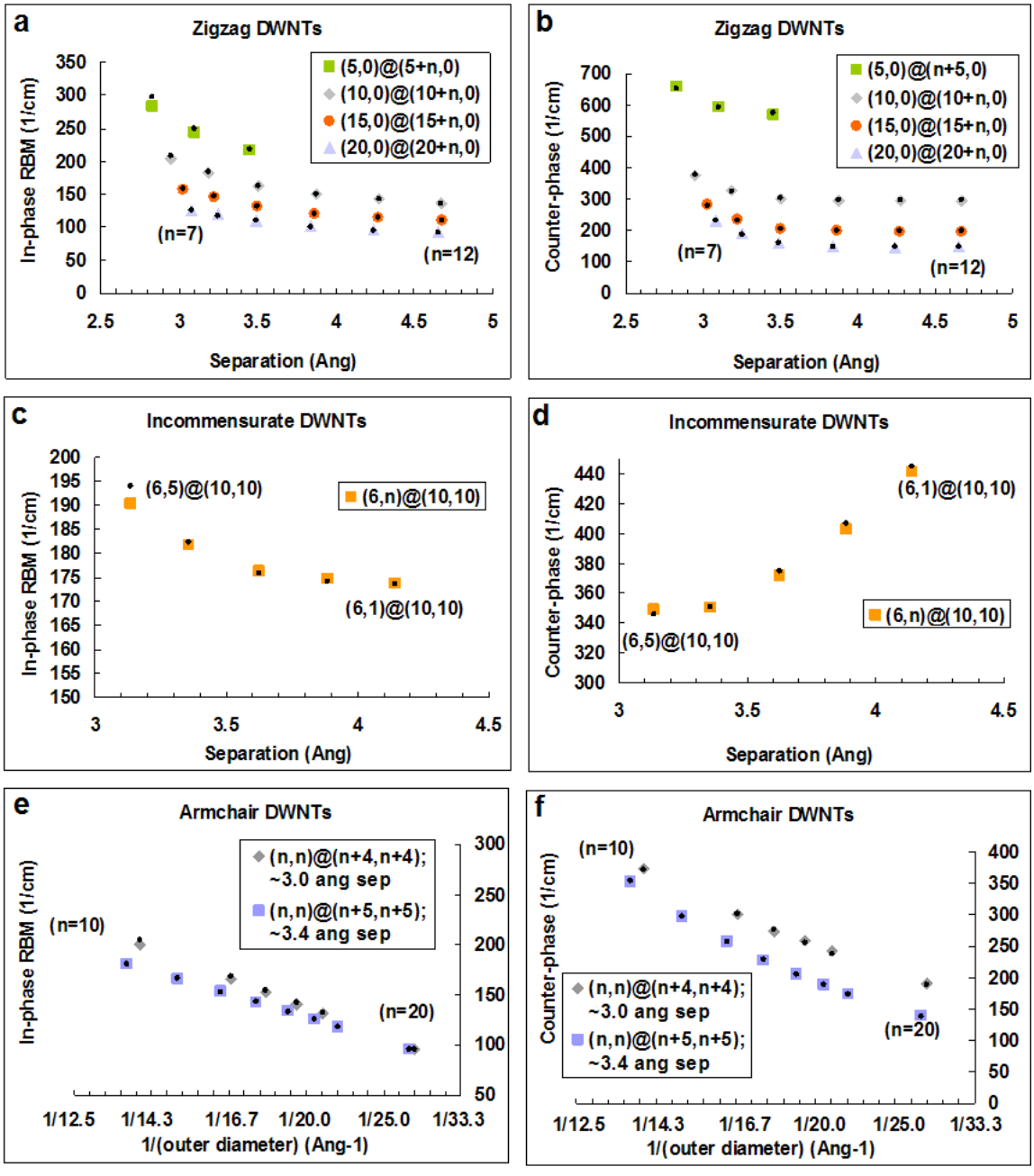

Figure 3. In-phase radial breathing modes are on the left and counter phase modes on the right. The DWNTs in figures a and b have zigzag inner and outer walls, those in c and d have chiral inner walls and armchair outer walls, and those in e and f have armchair inner and outer walls. In a, b, the inner shell was kept constant and the outer shell changed. For c, and d, the outer shell was constant and the inner shell varied. For e and f, the inter-shell spacing was kept constant while the overall diameter of the DWNTs was varied. All DWNT models were optimized using energy and force minimization. The results show good reproduction of atomistic simulations, shown in color, by the analytical results, shown in black.

An interesting point from figure 3 is that the analytical expression using α and ε optimized from zigzag DWNT data accurately predicts the RBMs of armchair and incommensurate chiral DWNTs. This demonstrates that the chiralities of the inner and outer shells do not shift RBMs appreciably for DWNTs with the same inner and outer diameters.

1.7 Bundled DWNTs

Although our study gives a simple way of calculating RBMs for individual DWNTs, most experimental RBM data reported in the literature are taken on nanotube bundles where inter-nanotube van der Waals interactions couple the RBMs of bundled carbon nanotubes together. To study the effects of these interactions, we optimized the geometries of homogeneous SWNT and DWNT bundles in vacuum and calculated their RBMs. Each bundle contained seven identical carbon nanotubes, leading to seven RBMs for SWNTs and fourteen RBMs for DWNTs. Two representative geometries are shown in figure 4.

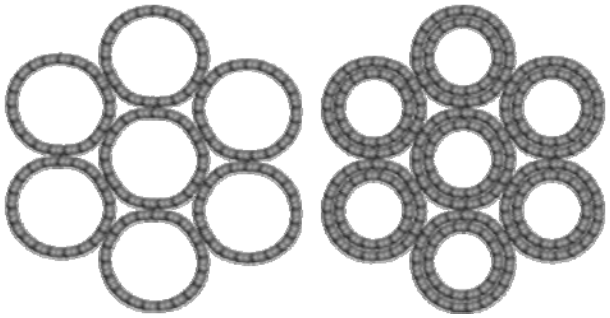

Figure 4. A bundle of seven (20, 20) SWNTs on the left shows distortion as a result of bundling. On the right, seven (20, 20)@(15, 15) nanotubes show similar, but much smaller distortion. The diameter for a individual (20, 20) SWNT was 27.3 Angstroms.

Data from bundled SWNTs are shown in figure 5. For nanotubes smaller than 16.5 Å, each RBM is consistent with equation 1 with an added constant *b* between 0 cm^{-1} to 10 cm^{-1}. For nanotubes bigger than 16.5 Å, there is a slight deviation from equation 1 due to distortion of the nanotube sidewall from a radial to a hexagonal shape. See figure 4a.

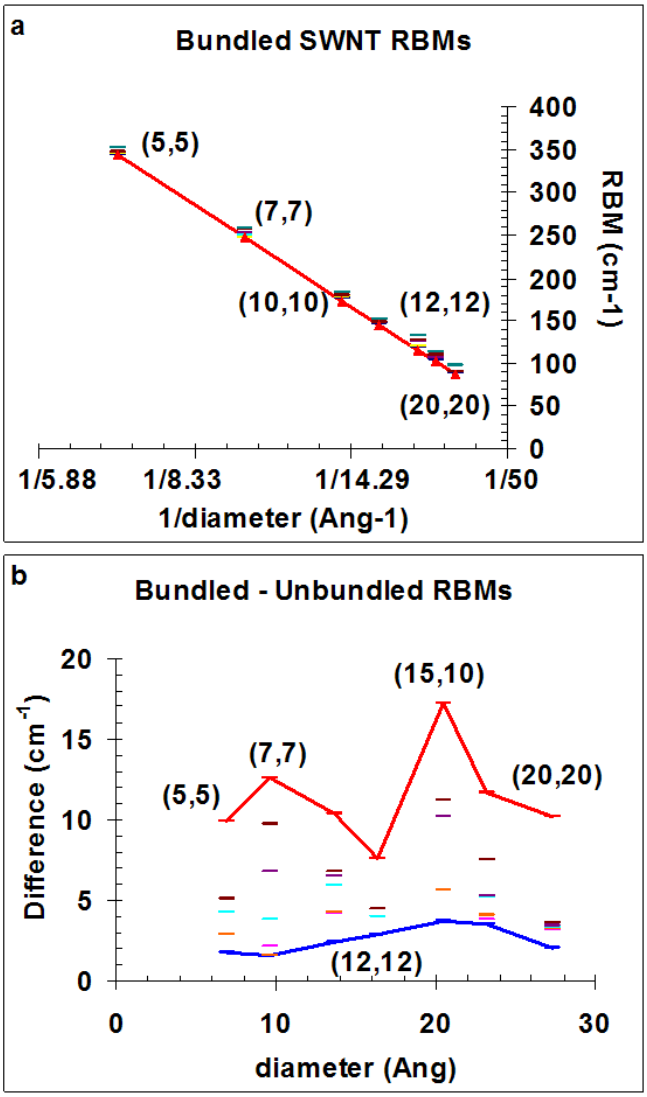

Figure 5. 5a shows the RBM of SWNTs in 7 nanotube homogeneous bundles as points while the RBMs of individual nanotubes are shown as a red line. 5b shows the difference of the individual SWNT RBM subtracted from the 7 modes.

For DWNT bundles, two series of geometries were considered. Both series have *(n,n)* armchair inner shells with either *(n+5,n+5)* or *(n+4,n+4)* outer shells. In each series, the sizes of the inner and outer shells were increased in single increments of chirality and their RBMs calculated. The resulting RBM shifts follow a complicated trend due to the progressive deformation of outer shells into increasingly hexagonal

geometries as nanotube size is increased. See figure 6 for the shift of RBMs in bundled versus unbundled DWNTs.

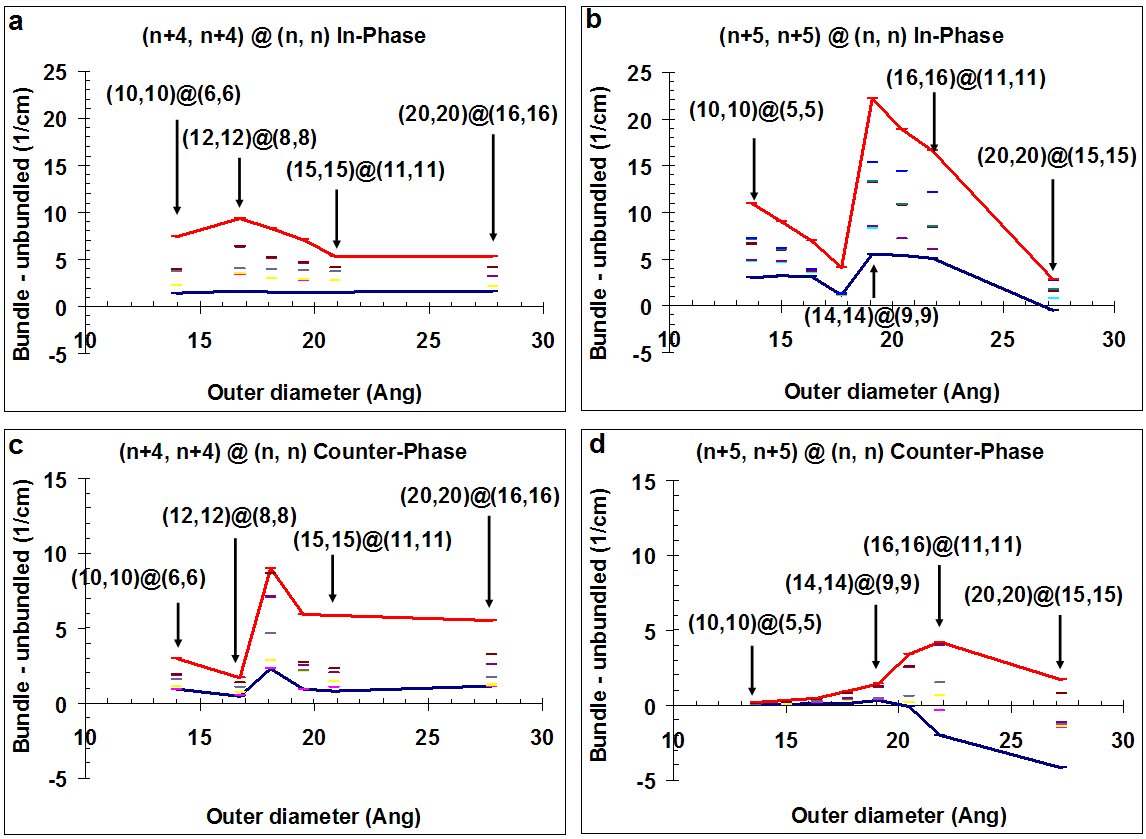

Figure 6. The differences between bundled and unbundled DWNT in-phase and counter-phase radial breathing modes are plotted. Select points are labeled with the outer and inner chiralities of the DWNT. For (n+5, n+5)@(n, n) nanotubes, the inter-shell spacing was around 3.4 angstroms. The largest deviation from dispersed values of in-phase RMBs was 16.55 % while the largest deviation for counter-phase RBM was -3.02 %. For (n+4, n+4)@(n, n) nanotubes, the inter-shell separation was around 3.0 to 3.1 angstroms. The largest in-phase deviation was 5.66% while the largest counter-phase deviation was 3.29%.

The counter-phase RBMs of DWNT bundles shifted less than 3.5% compared to corresponding unbundled nanotubes. For in-phase RBMs, the (*n+4,n+4)@(n,n)* DWNT

bundles, whose nanotubes have 3.0 to 3.1 Å inter-shell separation, experienced 3 % to 6 % increases while the *(n+5,n+5)@(n,n)* DWNT bundles, whose nanotubes had inter-shell separations of around 3.4 Å, had shifts from 5% to 16.55%. In the *(n+5,n+5)@(n,n)* bundles, there was a rapid increase of the RBM shift from 5 % to over 15 % when the outer diameter was increased from 17 Å to 19 Å, and a rapid fall back to below 5 % with further increases in diameter.

The range of carbon nanotubes sizes and separations tested here are reasonable geometric parameters for real world DWNTs. Experimenters interpreting RBM data on nanotubes of these approximate sizes need to be mindful of these large frequency shifts if their sample nanotubes are bundled.

1.8 Solving the inverse problem

Our results give an analytical expression that allows the numerical solution of the inverse problem, namely, finding d_i and d_o for a given pair of in-phase and counter-phase RBMs. An examination of the diameter and separation contour maps for the counter-phase RBM ω_+ and the in-phase RBM ω_- reveals a simple optimization landscape conducive to numerical methods such as simplex optimization. The examination also shows, however, that there are two pairs of inner and outer shell diameters for each pair of radial breathing modes. Further complications arise because it is unknown whether both in-phase and counter-phase RBMs will show up at the same excitation energy. Finally, there is the effect of inter-nanotube coupling inside nanotube bundles.

As a test, we applied our method to analyze RBMs reported by Liu, Yu, and Zhang for small diameter DWNTs grown on MgO supported Fe-Co catalyst [8]. The

authors conducted HRTEM studies showing in ter-layer separation ranging from 0.35 nm to 0.42 nm. We believe that two factors complicate interpretation of their HRTEM data. First, HRTEM could sam ple only a very small portion of the nanotubes produced. Second, the exact thickness of each shell and therefore the separation of shells seen in their HRTEM picture is not unambiguous in light of possible associated am orphous carbon contam inants, defects, and nontrivial scattering of the el ectron beam . For a broader look at their sample, the authors re ported RBM data at 488 nm excitation. The data showed peaks at 150 cm $^{-1}$, 158 cm $^{-1}$, 197 cm $^{-1}$, 227 c m^{-1}, 257 cm $^{-1}$ and 385 cm $^{-1}$. Based on the assum ption of independently vibr ating she lls, the authors interp reted this data as showing that the nanot ubes they grew had a narrow d_i distribution from 0.6-1.2 nm and a narrow d_o distribution from 1.3-2.0 nm.

Table 1. RBM data from reference 8 analy zed u sing the cont inuum model for dispersed and bundled DWNT RBMs.[a]

Application of RBM analysis to experimental data				
Counter-phase (cm^{-1})	In-phase (cm^{-1})	d_i (Å)	d_o (Å)	Δ (Å)
385	150	6.15994	15.7382	4.78913
		13.15222	18.77304	2.81041
	158	6.15792	14.92034	4.38121
		12.3228	17.95668	2.81694
	197	6.4182	12.91342	3.24761

		9.00318	14.75078	2.8738
	227	no solution		
	257	no solution		
257	150	9.4856	16.4328	3.4736
		12.28984	18.4547	3.08243
	158	10.17638	16.66472	3.24417
		10.79442	17.12882	3.1672
	197	no solution		

[a] The most plausible counter-phase RBM candidate peaks from analysis of raw data are circled in dashed lines and shaded in gray, and plausible dimensions of inner and outer nanotubes are circled. Nanotubes with inter-shell separation smaller than 3.0 Å have high energetically unfavorable.

Table 1 shows an analysis of Liu et al's data. Because we could not determine which peaks correspond to in-phase modes and which ones to counter-phase modes, we began by taking the highest frequency mode and matching it one by one with lower frequency modes. Then we moved to the next highest frequency mode, and so forth, until all modes were accounted for. We assumed that that inter-shell separation should be greater than 2.5 Å but less than 6.0 Å, and used multiple Nelder-Mead numerical optimization runs to obtain the two converged solutions for each wave number pairing. The best solutions are circled using dashed lines.

Simulation results (fig. 6) show that, in DWNT bundles, inter-nanotube coupling shifts the observed RBM wave-numbers. Is this significant for the determination of inner

and outer diameters? Assuming the observed RBM is the average value of the coupling induced peaks, we recalculated diameters after shifting the observed wave numbers by amounts consistent with the simulation. If the 385 cm^{-1} peak remains constant and the 197 cm^{-1} peak is shifted to 191 cm^{-1}, one could get a DWNT with 13 Å outer diameter and 3.34 Å inter-shell separation. Similarly, shifting the 257 cm^{-1} peak to 254.5 cm^{-1} and the 158 cm^{-1} peak to 154 cm^{-1} would give two solutions: a 16.6 Å DWNT with 3.34 Å inter-shell separation, and a 17.8 Å nanotube with 3.12 Å inter-shell separation. In each case, the RBM shifts due to inter-nanotube coupling changed the calculated inter-shell separation by 0.1 Å, which could affect expected inter-shell electronic coupling.

Whether or not inter-nanotube coupling is taken into account, our analysis of the Liu, Yu, and Zhang data suggests that their sample contained significant number of DWNTs with inter-shell separation between 3.1 Å an 3.4 Å and outer diameters from 13 Å to 18 Å. This is consistent with their HRTEM pictures considering the ambiguities discussed earlier. Interestingly, the small inter-layer separation in these nanotubes could result in a greater proportion of metallic nanotubes due to inter-layer electronic structure coupling[5].

1.9 Conclusion

In this paper we have calculated the RBMs of a variety of DWNTs. The results of our atomistic simulations show that inter-layer and inter-nanotube dispersive coupling significantly affect observed RBMs. We also demonstrate that RBM of DWNTs do not depend explicitly on the chiralities of the inner and outer shells. Instead, an analytical model treating the two shells as homogeneous elastic cylinders coupled by a van der

Waals force is sufficient to account for th e observed RBM data. Our analytical model gives accurate predictions of RBMs for isolat ed DW NTs in an experimentally relev ant parameter space, and w e can us e it to pred ict RBMs for nanotubes g iven inner and outer diameters, o r extract po ssible inner and outer diam eters gi ven pairs of in-phase and counter-phase RBMs. Finally, we show that the effects of inter-nanotube coupling in DWNT bundles could affect the calculated inter-shell separa tion. As these effects are more difficult to analy tically address, a m ore accurate assessm ent of the nanotube diameters and separations m ay require disper sal of the nanotubes using agents such as single s tranded DNA[14] and sodium dodecyl sulf ate. W e expect th at co llection of RBM data on individual DWNTs could thus give id entifying structural data that could allow correlation between electronic structure and geometric structure of DWNTs.

Supporting Information Available: A Mathematica 7.0 notebook source code for the calculation of RBMs from diameters and of diameters from RBMs is provided under the GPL license. Supplemental tables are also provided. This material is available free of charge via the Internet at http://pubs.acs.org/doi/suppl/10.1021/jp805828g

1.10 References

[1] Lyu, S. C.; Liu, B. C.; Lee, C. J. *Chem. Mater.* **2003**, *15,* 3951-3954

[2] Hutchingson, J. L.; Kiselev, N. A.; Krinichnay a, E. P.; Krestinin, A. V.; Loutf y, R. O.; Morawsky, A. P.; Muradyan, V. E.; Obraztsova, E. D., Sloan, J.; Terekhov, S. V.; Zakharov, D. N. *Carbon*, **2001**, *39*, 761

[3] Bandow, S.; Chen, G.; Sumanasekera, G. U.; Gupta, R.; Yudasaka, M.; Iijim a, S.; Eklund, P. C.; *Phys. Rev. B*, **2002**, *66*, 075416

[4] H. Kurachi *et al, Proceedings of 21st International Display Research Conference/8th International Display Workshops*; Society for Inform ation Display: San Jose, CA, **2001**, 1245-1248

[5] Deng, W.; Goddard, W. A. III; in preparation.

[6] Guo, Y.; Karasawa, N.; and Gooddard, W. A. III *Nature*, **1991**, *351*, 464

[7] Wu, G.; Zhou, J.; Dong, J. *Phys. Rev. B*, **2005**, *72*, 115418

[8] Liu, B. C.; Yu, B.; Zhang, M. X. *Chem. Phys. Lett.*, **2005**, 407, 232

[9] Simon, F.; Kukovecz, A.; Kenya, Z.; Pfeiffer, R.; Kuzmany, H. *Chem. Phys. Lett.,* **2005**, *413*, 506-511

[10] Rahmani, A.; Sauvajol, J.-L.;Cambedouzou, J.; Benoit, C. *Phys. Rev. B*, **2005**, *71*, 125402

[11] Bachilo, S. M.; Stran o, M. S.; Kittr ell, C.; Hauge, R. H.; Sm alley, R. E.; Weisman, R. B. *Science,* **2002** *298*, 2361

[12] Jorio, A.; S aito, R.; Ha fner, J. H.; Lieber, C. M.; Hunte r, M.; McC lure, T.; Dresselhaus, G.; Dresselhaus, M. S. *Phys. Rev. Lett.*, **2001**, *86*, 1118–1121.

[13] Deshpande, V. V.; Chiu, H.-Y.; Postm a, H. W . Ch.; Miko, C.; Forro, L .; Bockrath, M., *Nano Letters,* **2006**, *6*, 1092

[14] Zheng, M.; Jagota, A.; Se mke, E. D.; Dine r, B. A.; McLea n, R. S.; Lustig, S. R.; Richardson, R. E.; Tassi, N. G. *Nature Materials,* **2003**, *2*, 338

[15] Hashimoto, A.; Suenaga, K.; Urita, K.; Shimada, T.; Sugai, T.; Bandow, S.; Shinohara, H.; Iijima, S. *Phys. Rev. Lett.*, **2005**, *94*, 045504

Chapter 2

Self-assembly of Carbon Nanotubes into Two-dimensional Geometries using DNA Origami Templates

This chapter is adapted from the following paper with Hareem T. Maune, Robert D. Barish, Marc Bockrath, William A. Goddard III, Paul W.k. Rothemund, and Erik Winfree

Maune HT, Han SP, Barish RD, Bockrath M, Goddard WA, Rothemund PWK and Winfree E, *Nature Nanotechnology*, **5** (1): 61-66 (**2010**)

2.1 Introduction

A central challenge in nanotechnology is the parallel fabrication of complex geometries for nanodevices. Here we report a general method for arranging single-walled carbon nanotubes in two dimensions using DNA origami—a technique in which a long single strand of DNA is folded into a predetermined shape. We synthesize rectangular origami templates (∼75 nm × 95 nm) that display two lines of single-stranded DNA "hooks" in a cross pattern with ∼6 nm resolution. The perpendicular lines of hooks serve as sequence-specific binding sites for two types of nanotubes, each functionalized non-covalently with a distinct DNA linker molecule. The hook-binding domain of each linker is protected to ensure efficient hybridization. When origami templates and DNA-functionalized nanotubes are mixed, strand displacement-mediated deprotection and binding aligns the nanotubes into cross-junctions. Of several cross-junctions synthesized by this method, one demonstrated stable field-effect transistor-like behaviour. In such organizations of electronic components, DNA origami serves as a programmable nanobreadboard; thus DNA origami may allow the rapid prototyping of complex nanotube-based structures.

Single walled carbon nanotubes (SWNTs) have exceptional electronic properties that suggest their use in nanoscale information processing devices. Towards this goal, there have been advances in SWNT synthesis [1], dispersion [2], sorting by electronic property [3] or length [4], and modification [5]. Methods for the parallel alignment of SWNTs have allowed the creation of lithographically-defined high-performance electronic devices [6]. But the arrangement of individual SWNTs into complex nanoscale geometries is an open challenge. Lithographic methods which produce the smallest arbitrarily complex patterns, such as dip-pen [7] and e-beam [8], are serial processes; nanoimprint lithography can replicate such patterns [9] but methods for solving chal-

lenges such as alignment are still being developed [10]. Thus while organization of SWNT by lithographically-patterned affinity templates [11] or electrodes [12] could allow creation of complex circuits, scaling up production remains difficult. Approaches based on protein and/or DNA self-assembly potentially provide parallelism. Many such methods have only created one-dimensional (1D) SWNT structures [13, 14] and devices [15, 16] in which a single SWNT positioned between a pair of electrodes is switched by the substrate back-gate. One method has created structures where DNA linkers define the connectivity between three carbon nanotubes [17], however the angles between the nanotubes are uncontrolled. Two-dimensional (2D) control over SWNT organization is necessary to deterministically and reproducibly create circuits of many devices in which SWNTs gate other SWNTs directly.

DNA nanotechnology [18, 19] provides simultaneously parallel and geometrically-complex nanofabrication by exploiting the binding specificity and structural predictability of nucleic acids. Over two decades ago, it was proposed [20] that DNA nanostructures could be used to template a three-dimensional memory. So far, DNA has been used to organize gold nanoparticles [21] into arrays and self-assemble 1D SWNT electronic devices [15]. Scaffolded DNA origami [22] enables construction of arbitrary, $\sim$ 100 nm, 2D shapes that can display desired patterns of 200 chemical modifications with $\sim$6 nm resolution. Trillions of origami can be self-assembled in milliliter reaction volumes in a single step. These properties suggest that DNA origami could be used to organize SWNTs into desirable device architectures [23, 24, 25]. Interfacing such circuits with the macroscale may require some top-down lithography, but the goal of using DNA templates is to shift more of the burden of creating complex geometries from lithography to self-assembly.

2.2 Cross-junction assembly scheme

Our approach is to align nucleic acid-labeled SWNTs (NL-SWNTs) along lines of

complementary single-stranded (ssDNA) "hooks" [26] on DNA origami. In principle, multiple populations of NL-SWNTs with different properties (e.g. semiconducting or metallic) could be labeled with different sequences, and self-assemble simultaneously into a complex geometry defined by the layout of lines on an origami. Fortuitously, when single-stranded DNAs (ssDNAs) are sonicated with SWNTs, they attach via physisorption of DNA bases to SWNT sidewalls [3] and cause the SWNTs to disperse [2] in aqueous solution. This non-specific interaction allows noncovalent attachment of DNA labels to SWNTs without disrupting their electronic properties [27] and provides a simple route to NL-SWNTs.

It is difficult, however, to design a DNA molecule that both disperses SWNTs and serves as a efficient label, since any ssDNA label it carries can also bind the SWNTs and either crosslink the SWNTs or become unavailable for binding hooks. Such SWNT-bound labels are capable of partial desorption and hybridization to free DNA hooks, but they do so prohibitively slowly [28]. In many applications such as those in which SWNT are purposefully aggregated by DNA labels [29], it is only necessary that a fraction of DNA labels bind cognate hooks. However, to bind and align a SWNT with high fidelity to a row of relatively few DNA hooks on an origami it seems important that a high fraction of the SWNT's labels bind. This suggests any DNA label intended to attach to the hooks must be protected from sticking to the SWNT, for example by making it double-stranded DNA (dsDNA). But this presents the secondary challenge of removing the complementary "protection strand" at the right time so that the DNA label can attach to hooks while remaining attached to the SWNT. Previous work employing protecting strands [30] or other secondary strands [31] do not protect ssDNA labels during critical assembly steps; thus these schemes appear to lack the level of control required for 2D organization.

Here we prepare NL-SWNTs using a protection scheme borrowed from the construction of DNA nanomachines [32] and self-assemble them on DNA origami tem-

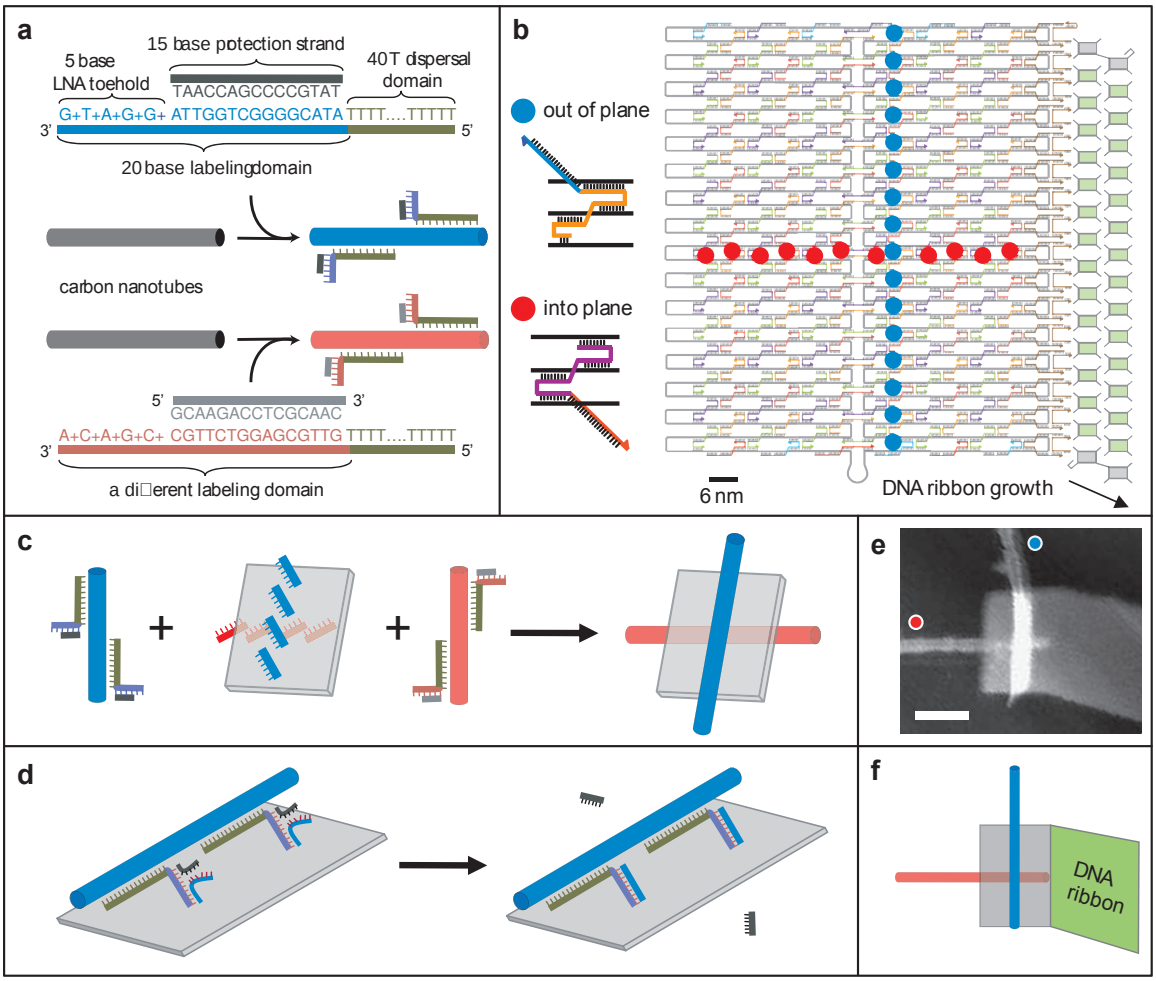

Figure 1: **Overview of cross-junction assembly.** **(a)** NL-SWNTs differ by linkers whose labeling domains have different sequences. To distinguish them, SWNTs labeled with one sequence have been colored red and those labeled with the other, blue. Dispersal domains bind linkers to SWNTs; labeling domains project into solution. **(b)** A ∼7000 base long scaffold strand (gray) and ssDNA staples (multicolored) form a a rectangular origami template. Adapter strands (brown) on the right edge of the origami serve as nucleation sites for growth of a DNA ribbon (green/gray tiles). Red and blue dots indicate a pattern of hooks projecting from the origami. Insets show how staples are modified to carry hooks complementary to NL-SWNT labeling domains of corresponding color; the scaffold is black. Red hooks project into the plane; blue hooks project out. **(c)** Red and blue NL-SWNTs are mixed with a DNA template. They self-assemble sequence specifically with programmed orientations, red NL-SWNTs horizontally and blue NL-SWNTs vertically. **(d)** The toehold on a linker initiates binding to a hook, leading to branch migration and release of the protection strand. Ribbons not shown in (c) and (d). **(e)** A typical AFM height image of a cross-junction on mica under buffer; red and blue dots indicate NL-SWNT type. Scale bar, 50 nm. **(f)** A schematic interpretation of (e) highlights the relationship of origami, ribbon, and SWNTs.

plates to create 2D cross-junctions. In this scheme, protection strands are removed by the process of labels hybridizing to the origami hooks. Thus throughout our method, ssDNA labels remain almost completely protected until they bind the DNA origami; only short "toehold" sequences are ever exposed as ssDNA. We created two types of NL-SWNTs (labelled "blue" and "red" for convenience) by using two different linkers to disperse separate aliquots of High Pressure CO Conversion (HiPco) SWNTs (Fig. 1a). (Each aliquot comprised a mixed population of semiconducting and metal SWNTs. In principle pure populations of semiconducting and metallic SWNT could be used to specify exclusive assembly of semiconductor-metal cross-junctions, the arrangement most likely to act as a FET.) Each linker is a two-stranded, partially-duplex complex that adsorbs onto a SWNT via a 40-base poly-thymine (poly-T) dispersal domain. Its 20 nucleotide labeling domain (design methods in Supplementary Information, Text S1 and [33]) has a sequence specific to its color and is complementary to similarly-colored hooks on a DNA origami template (Fig. 1b). A 15 base protection strand leaves 5 bases of the labeling domain unprotected. These 5 bases comprise the toehold, which is composed of locked nucleic acid (LNA). During dispersal, we expect the poly-T dispersal domain to adsorb on the SWNT while the protection strand prevents adsorption of the labeling domain. The relative instability of SWNTs dispersed by short ssDNA (4 or 6 nt) [34] suggests that the interaction of the short toeholds with the SWNT sidewalls is dynamic, making them available for binding hooks. (Short toeholds also appear important since the use of 7 or 10 nt ssDNA toeholds resulted in cross-linked SWNTs during dispersal.) At the same time, the toehold is long enough that initiation of deprotection is still fast (toeholds should be $\geq$ 4 bases to maximize reaction rate [35]). During assembly (Fig. 1c), a DNA hook complementary to all 20 labeling domain bases binds first to the 5 LNA base toehold and initiates branch migration (Fig. 1d); this allows the hook to displace the protection strand and bind to the entire labeling domain [32, 36]. We chose LNA for

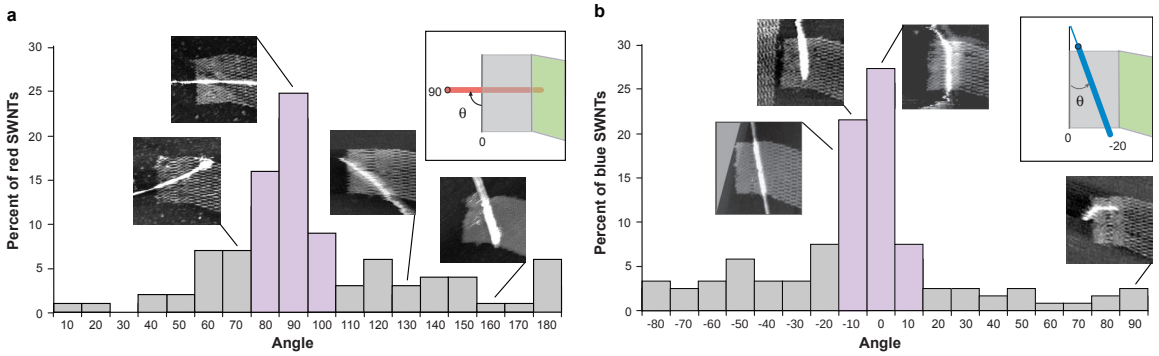

Figure 2: **Distributions showing sequence-specific attachment of NL-SWNTs to DNA templates and angular control over orientation.** Randomly selected origami templates incubated with red or blue NL-SWNTs were imaged by AFM. Of these, 100 red NL-SWNT/template constructs **(a)** and 121 blue NL-SWNT/template constructs **(b)** were intact and had a single SWNT bound, ∼50% of the total templates of each type. AFM images show examples of attachment at various angles. Insets in (a) and (b) show how SWNT angle was defined with respect to the origami's edge and ribbon orientation. Angles are defined similarly but the ranges are offset; angles of 100° to 180° in (a) corresponds to angles of −80° to 0° in (b). For both distributions ≥ 50% of tubes fall within ±15°(purple) of desired angle. The third image from left in (b) is flipped; unlike the others this structure landed blue face down.

toeholds because branch migration efficiency increases with toehold binding stability [37], and LNA-DNA duplexes are more stable than their DNA counterparts.

Our template design (Fig. 1b, Supplementary Information, Figs. S1–S3 and Text S2) is based on the "tall rectangle" origami [22], formed by ∼200 DNA staples that fold a long scaffold strand into the desired sheet of B-form helices. The sequence of each staple (typically 32 bases) determines its unique position in the sheet. Hence a DNA hook can be placed at any position by extending the 3' end of the appropriate staple. DNA helical twist (10.5 bases per turn) determines the angle of the backbone relative to the plane of the origami; this allows hooks to be added to either face. We added a row of eleven red hooks to the bottom, and a column of sixteen blue hooks to the top. In the original design, all staple ends fall on the bottom; thus, to project red hooks down, we concatenated the red hook sequence onto 3' ends of staples in the desired row. For each staple in the blue column, we shifted the staple's 3' end by half a turn (5 nucleotides) to position it on top and concatenated the blue hook sequence onto

the end. Between each hook and staple sequence, we inserted a four-thymine spacer.

Origami aggregate via stacking interactions between helix ends along their vertical edges. Thus we omitted the leftmost column of staples from the original design [22]; this resulted in a column of single-stranded loops that inhibited stacking (Fig. 1b). Also, we replaced the rightmost column of staples with DNA strands that nucleated growth of a ∼100 nm wide, typically > 500 nm long, DNA ribbon (Fig. 1b) via algorithmic self-assembly of DNA tiles [38, 39]. Addition of ribbons made image interpretation easier and appeared to increase the deposition rate of SWNT/DNA constructs.

2.3 Fidelity of alignment

To measure the efficiency, specificity, and orientation of attachment for red and blue NL-SWNTs (independently) we imaged > 200 SWNT/DNA constructs assembled using only red or blue SWNTs. Constructs were assembled by separately mixing either blue or red NL-SWNTs with templates displaying the cross pattern of red and blue hooks (Fig. 1b). In each case SWNTs had an opportunity to bind to either red or blue hooks. The desired outcome for each construct was a single SWNT aligned over the complementary hook array. Nonspecific attachment would result in incorrect alignment or binding of more than one tube. Constructs were deposited on mica and scanned under buffer; 86% of templates mixed with red SWNTs had ≥ 1 SWNTs attached, as did 80% of templates mixed with blue SWNTs. Of templates with attached SWNTs, ∼25% were distorted or aggregated. Overall, ∼50% of all templates were intact and had a single SWNT attached, as desired. Fig. 2 shows the distribution of alignments between templates and attached SWNTs. The angle of the ribbon with respect to the origami (Supplementary Information, Fig. S4a) allowed us to distinguish between red and blue faces and to define SWNT alignment angles. Fig. 2 shows that the angular distribution for blue SWNTs peaks at ∼0° (as expected) with 56%

oriented within ±15° of the peak. The distribution of red SWNTs peaks at ∼90°(as expected) with 50% within ±15°of the peak. These data suggest NL-SWNTs strongly prefer their complementary hook array and align parallel to it. The importance of the protection strands for binding efficiency was verified in a control experiment: when blue SWNTs were prepared without protection strands < 10% of DNA templates had SWNTs attached.

2.4 Cross-junctions

We assembled cross-junctions (Supplementary Information, Text S3) by mixing templates with both red and blue NL-SWNTs simultaneously and visualized them by AFM, (Fig. 1e,f and Supplementary Information, Fig. S5). Cross-junctions, like these examples, are frequently asymmetric as NL-SWNTs often bind near their ends (for unknown reasons), even appearing to align so that their ends are flush with the edge of the origami template. In the final constructs, red and blue NL-SWNTs are separated by a layer of DNA composed of their respective linkers (at least 1 nm where linkers attach due to the thickness of the poly-T dispersal domains, potentially up to a few nm depending on the detailed configuration of linkers) and the DNA origami (2 nm thick) that lies between them. AFM height measurements of the cross junctions (∼4 nm) provide a weak upper bound for the thickness of the layer (given that we cannot measure the thickness of naked SWNTs for the exact structures in question). In principle the intervening DNA layer is thicker with the SWNT on opposite sides of the origami, and we chose this geometry (over binding both SWNTs to the same side). We hypothesized that, if retained, a thicker intervening DNA layer might function as a better insulator so that in the randomly occurring cases where one SWNT of the cross junction was metallic and the other SWNT semiconducting, the metallic SWNT would more likely exert FET-type gating on the semiconducting SWNT. To look for possible FET-behavior, we electrically characterized several cross-junctions.

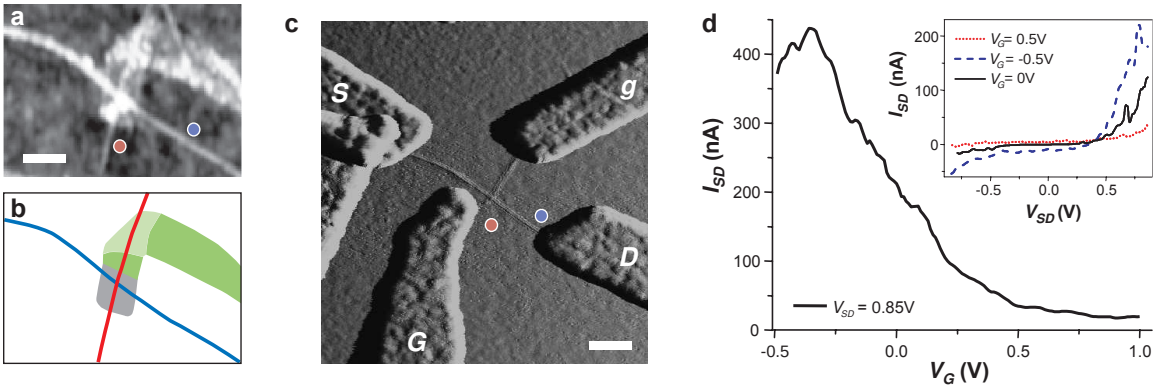

Figure 3: **Electrical characterization of a self-assembled SWNT cross-junction.** **(a)** AFM height image of an SWNT cross-junction on dry SiO_2 before electrode deposition. **(b)** Interpretation of (a) indicating red and blue SWNTs, origami (gray), ribbon (dark green) and a place where the ribbon has folded back on itself (light green). Origami and ribbon contours are approximate; the origami-ribbon boundary, ribbon orientation, and color of the top SWNT cannot be determined. **(c)** AFM amplitude image of cross-junction from (a) with e-beam patterned Pd/Au electrodes; the DNA template is no longer visible. Scale bars are 100 nm; red and blue dots indicate NL-SWNT type, determined from ribbon orientation. Electrode labels: S, D, G and g. **(d)** Source-drain current (I_{SD}) versus SWNT gate voltage (V_G) for a source-drain bias of 0.85 V. The current pre-amplifier used for measuring I_{SD} also served as a virtual ground. Inset shows the source-drain $I - V$ for different gate biases.

Cross-junctions were deposited on O_2 plasma-treated silicon wafers. Electrode fabrication and device measurement (Supplementary Information, text S5) was unreliable because the closely-spaced ends of cross-junctions often required electrode placement with sub-50 nm precision and HiPco SWNTs have high intrinsic resistance. SWNT ends were contacted by Pd/Au electrodes fabricated using electron beam lithography without post-fabrication thermal annealing (in an attempt to preserve the DNA template at the junction). DNA on SWNTs was selectively degraded in contact regions (but not at photoresist-protected cross-junctions) using an HCl rinse and "DNA-AWAY" (Molecular BioProducts) surface decontaminant. Electrode fabrication was attempted for 23 cross-junctions; of these, six exhibited electrical conductance across one or both SWNTs and were further characterized by re-imaging and electrical measurements. Because the 17 nonconducting trials were not re-imaged it is unknown whether contacts were successfully made to these junctions.

Three of the six fully-characterized devices exhibited FET-like behavior; two were short-lived (Supplementary Information, Fig. S9 shows FET behavior in a short-lived device) and one had electronic properties stable over tens of up-down voltage cycles (Fig. 3 and Supplementary Information, Fig. S8). For the stable device, the blue SWNT was used as the conduction channel and the red SWNT as the presumptive gate. Two-terminal I/V measurement across the source (S) and drain (D) electrodes of the blue SWNT (with $V_G = 0$) gave $\sim$2 MΩ resistance in the ohmic region (Supplementary Information, Fig. S8a). I/V measurements across the gate electrodes (G and g) of the red SWNT (with channel electrodes S and D left floating) gave $\sim$6 GΩ resistance (Supplementary Information, Fig. S8b). However the inter-SWNT tunneling current (I_{GD} with S and g floating) showed only $\sim$3 MΩ of resistance when $V_{GD} < -0.5$ V (Supplementary Information, Fig. S8c), indicating that the portion of the red SWNT leading from electrode G to the cross-junction is more conductive than implied by the measurement of I/V between G and g, and suggesting that the red SWNT-electrode g contact is responsible for the high resistance between G and g. (It is extremely rare for all four contacts in such devices to be low resistance [40].)

For V_{GD} between $\pm$0.5 V, the resistance was high (the inter-SWNT tunneling current was negligible, Supplementary Information, Fig. S8c) providing a region in which the red SWNT could serve as a gate. Our intent had been that the DNA layer between the SWNTs would act as an insulator/dielectric to create this effect. However, for this device, we did not find an intact template after liftoff of the resist—we do not know whether any DNA (from the linker or origami) remained at the cross-junction. Thus possible causes of the high resistance region include remnant DNA, a Schottky barrier between the two SWNTs [41] or defects in the conduction path from G to D. (In any case, an adequate conduction barrier was obtained.) Finally, to test for FET behavior, we swept the gate voltage V_{GD} ($\pm$0.5 V) at constant channel voltage ($V_{SD} = 0.85V$) and observed the that the channel current (I_{SD})

was consistent with field-effect gating of a p-type semiconducting SWNT (Fig. 3d). The transconductance (dI_{SD}/dV_{Gg}) may contain contributions from the electric fields of both the red SWNT and electrode G (G was ∼70 nm from the blue SWNT); quantification of these contributions and determination of gating mechanism will require more sophisticated experiments such as scanned gate measurements [42].

Previous electrical characterization of crossed carbon nanotubes [41, 43, 44, 45, 40, 46] includes the creation of CNT-gated CNT-FETs from crosses of semiconducting and metallic SWNTs with explicitly deposited SiO_2 dielectric layers [46] and the observation of rectification in cross-junctions formed by metal and semiconducting SWNTs [41]. Our stable device is not directly comparable to these devices because identification of the gate SWNT as a metal or semiconductor is ambiguous. However the behavior of the stable device falls within the range of behaviors previously reported.

2.5 Conclusions

We have demonstrated how DNA origami can be used to introduce 2D geometry to the self-assembly of SWNT structures; our method should apply straightforwardly to other DNA nanostructures [19]. We have shown that SWNT/DNA constructs can be transferred from solution to dry SiO_2 with their geometry and electronic function intact; thus our process may be compatible with other standard microfabrication techniques. High resolution lithographic techniques need multiple steps to incorporate multiple materials—here we have organized two populations of SWNTs in a single step. Our method should allow the simultaneous nanoscale positioning and alignment of multiple populations of SWNTs (each with different properties) based on the sequence of their DNA linkers. Similarly our process should allow the simultaneous incorporation of other materials that can be labeled by DNA (e.g. gold nanocrystals [21]); this may lead to composite structures with novel electronic, optical, or

electrochemical properties.

Many open questions (Supplementary Information, Text S6) and challenges remain—some that are unique to the specific cross-junction devices prototyped here, and others that more generally address the DNA-based self-assembly approach. With respect to creating 2D SWNT FETs there are two difficulties. The first is the low-yield of randomly occurring metal-semiconductor cross-junctions. Pre-sorting SWNTs by electronic property [3] before linker attachment should enrich for the desired junction type. Second is a requirement for reproducible electrical behavior at the junction. Reproducibility might be improved either through consistent removal of the DNA interlayer, or consistent preservation. DNA-wrapping of SWNTs has previously been shown to enhance performance of one-dimensional SWNT FETs when the DNA was used to direct the assembly of a high-κ dielectric [27]. A similar approach to dielectric fabrication might be combined with our method.

Perhaps more fundamentally, there are several challenges that limit the self-assembly yield of a desired geometry, limit our ability to make better-defined geometries, or limit our ability to integrate a device into the larger geometry of a circuit architecture. The first is to control the translation of SWNTs along the lines of DNA hooks. Currently, the DNA hooks only specify the angle and intersection points of SWNTs; SWNT ends occur at random positions which makes contacting to them difficult. Such control might be achieved by using end-functionalized SWNTs [13] and/or using length-sorted SWNTs [4] whose lengths match those of the lines. The second challenge is to reduce device aggregation. Aggregation occurs because the solution phase self-assembly of SWNTs and templates allows multiple DNA templates to bind individual long SWNTs; it may be avoided by attaching SWNTs to templates only after the templates have been deposited. Random deposition would serve this purpose, but brings up the third challenge, that of localizing the devices to specific positions so that they may be conveniently integrated and "wired up". Recent efforts

have demonstrated the localization of individual DNA origami on lithographically-patterned substrates [47]. With solution of these three challenges our method might be extended to the synthesis of multi-SWNT memory circuits [48] or logic gates [49].

2.6 Methods

A detailed description of the experimental procedure can be found in the Supplementary Information.

Synthesis and purification of NL-SWNTS. Ultrasonic dispersal (Branson 2510 sonicator, 100 W, 90 min) of SWNTs used ∼600 μL of 32 μM nucleic acid linker solution (0.1 M NaCl) for every 0.1 mg of SWNTs. After dispersal, the concentration of excess free linkers (which could poison later assembly) was reduced by electrodialysis, and monitored by spectrophotometry or gel electrophoresis. In one typical experiment the post-purification concentration of free linker was reduced to 120 nM while the concentration of desired SWNT-attached linkers was 420 nM, a ratio of <1:3 (Supplementary Information, Text S1). Batch variation was considerable, e.g. concentrations of SWNT-attached linkers varied from 100 nM to 1 μM.

Synthesis and purification of origami/ribbons. Origami/ribbons were assembled with a 5:1 excess of staples:scaffold strands in Mg^{2+} buffer (40 mM Tris-acetate, 1 mM EDTA, 12.5 mM magnesium acetate, pH 8.3, 0.22 μm filtered) and ligated to covalently link adjacent short strands in the origami and ribbon [50]. This reduced origami/ribbon template fragmentation during deposition. Ligation introduced ATP, ligase, and extra buffer components. These extraneous reactants were reduced by spin filtration and the Mg^{2+} buffer was exchanged to Na^{+} buffer (0.75 M NaCl, 0.01 M Na_2HPO_4, pH ∼8, 0.22 μm filtered) to avoid Mg^{2+}-dependent precipitation of NL-SWNTs in the next step. (We have observed that dispersal in Mg^{2+} buffers results in lower concentrations of SWNT than dispersal in Na^{+} buffers and that SWNT

dispersed in Mg^{2+} buffers appear to aggregate more quickly; this was previously observed by Ming Zheng, personal communication.)

Assembly of NL-SWNT/DNA constructs. To create NL-SWNT/DNA constructs, we mixed NL-SWNTs with ∼0.5 nM origami/ribbon templates. (The concentration of NL-SWNTs was not known but in this final assembly buffer the concentration of NL-bound linkers was 10–100 nM.) We tried a variety of buffers and incubation temperatures, achieving best results at 25°C, 0.75 M NaCl, 0.01 M Na_2HPO_4 (∼ pH 8). The fraction of templates with attached SWNTs increased with incubation time. However, incubation times > 30 minutes sometimes resulted in aggregates of many templates and SWNTs, perhaps due to attachment of long SWNTs to multiple templates.

Deposition on Si wafers. Cross-junctions were deposited on O_2 plasma-treated silicon wafers (capped by 0.3-1.0 μm thick SiO_2) from Mg^{2+} and Ni^{2+} salt solutions. Although the DNA origami/ribbons appeared twisted and folded under dry mode AFM, the cross-junction geometry of SWNTs was typically intact (Supplementary Information, Figs. S6–7). Within a 400 μm^2 area, we typically found 5-10 self-assembled cross-junctions.

2.7 References

[1] Hata, K. *et al.* Water-assisted highly efficient synthesis of impurity-free single-walled carbon nanotubes. *Science* **306**, 1362–1364 (2004).

[2] Zheng, M. *et al.* DNA-assisted dispersion and separation of carbon nanotubes. *Nat. Mater.* **2**, 338–342 (2003).

[3] Zheng, M. *et al.* Structure-based carbon nanotube sorting by sequence-dependent DNA assembly. *Science* **302**, 1545–1548 (2003).

[4] Huang, X., McLean, R. S. & Zheng, M. High-resolution length sorting and purification of DNA-wrapped carbon nanotubes by size-exclusion chromatography. *Anal. Chem.* **77**, 6225–6228 (2005).

[5] Deng, W.-Q., Matsuda, Y. & Goddard, W. A. Bifunctional anchors connecting carbon nanotubes to metal electrodes for improved nanoelectronics. *J. Am. Chem. Soc.* **129**, 9834–9835 (2007).

[6] Cao, Q. & Rogers, J. A. Ultrathin films of single-walled carbon nanotubes for electronics and sensors: A review of fundamental and applied aspects. *Adv. Mater.* **21**, 29–53 (2009).

[7] Piner, R. D., Zhu, J., Xu, F., Hong, S. & Mirkin, C. A. "Dip-pen" nanolithography. *Science* **283**, 661–663 (1999).

[8] Vieu, C. *et al.* Electron beam lithography: resolution limits and applications. *Appl. Surf. Sci.* **164**, 111–117 (2000).

[9] Chou, S. Y., Krauss, P. R. & Renstrom, P. J. Imprint lithography with 25-nanometer resolution. *Science* **272**, 85–87 (1996).

[10] Wu, W. *et al.* Sub-10 nm nanoimprint lithography by wafer bowing. *J. Am. Chem. Soc.* **8**, 3865–3869 (2008).

[11] Wang, Y., Maspoch, D., Zou, S. & Schatz, G. C. Controlling the shape, orientation, and linkage of carbon nanotube features with nano affinity templates. *Proc. Natl Acad. Sci. USA* **103**, 2026–2031 (2006).

[12] Diehl, M. R., Yaliraki, S. N., Beckman, R. A., Barahona, M. & Heath, J. R. Self-assembled, deterministic carbon nanotube wiring networks. *Angew. Chem. Int. Ed.* **41**, 353–356 (2002).

[13] Williams, K. A., Veenhuizen, P. T. M., de la Torre, B. G., Eritja, R. & Dekker, C. Nanotechnology: Carbon nanotubes with DNA recognition. *Nature* **420**, 761 (2002).

[14] Lyonnais, S. *et al.* A three-branched DNA template for carbon nanotube self-assembly into nanodevice configuration. *Chem. Commun.* 683–685 (2009).

[15] Keren, K., Berman, R. S., Buchstab, E., Sivan, U. & Braun, E. DNA-templated carbon-nanotube field effect transistor. *Science* **302** (2003).

[16] Hazani, M. *et al.* DNA-mediated self-assembly of carbon nanotube-based electronic devices. *Chem. Phys. Lett.* **391**, 389–392 (2004).

[17] Bourgoin, J. P. *et al.* Directed assembly for carbon nanotube device fabrication. *Proc. Int. El. Devices Meet. (IEDM)* 1–4 (2006).

[18] Seeman, N. C. Nucleic-acid junctions and lattices. *J. Theor. Biol.* **99**, 237–247 (1982).

[19] Seeman, N. C. An overview of structural DNA nanotechnology. *Mol. Biotechnol.* **37**, 246–257 (2007).

[20] Robinson, B. H. & Seeman, N. C. The design of a biochip: A self-assembling molecular-scale memory device. *Protein Eng.* **1**, 295–300 (1987).

[21] Pinto, Y. Y. *et al.* Sequence-encoded self-assembly of multiple-nanocomponent arrays by 2D DNA scaffolding. *Nano Letters* **5**, 2399–2402 (2005).

[22] Rothemund, P. W. K. Folding DNA to create nanoscale shapes and patterns. *Nature* **440**, 297–302 (2006).

[23] DeHon, A. Array-based architecture for FET-based, nanoscale electronics. *IEEE T. Nanotechnol.* **2**, 23–32 (2003).

[24] Dwyer, C. *et al.* Design tools for a DNA-guided self-assembling carbon nanotube technology. *Nanotechnology* **15**, 1240–1245 (2004).

[25] Avouris, Ph., Chen, J., Freitag, M., Perebeinos, V. & Tsang, J. C. Carbon nanotube optoelectronics. *Phys. Status Solidi B.* **243**, 3197–3203 (2006).

[26] Ke, Y., Lindsay, S., Chang, Y., Liu, Y. & Yan, H. Self-assembled water-soluble nucleic acid probe tiles for label-free RNA hybridization assays. *Science* **319**, 180–183 (2008).

[27] Lu, Y. *et al.* DNA functionalization of carbon nanotubes for ultrathin atomic layer deposition of high κ dielectrics for nanotube transistors with 60 mv/decade switching. *J. Am. Chem. Soc.* **128**, 3518–3519 (2006).

[28] Jeng, E. S., Barone, P. W., Nelson, J. D. & Strano, M. S. Hybridization kinetics and thermodynamics of DNA adsorbed to individually dispersed single-walled carbon nanotubes. *Small* **3**, 1602–1609 (2007).

[29] Chen, Y., Liu, H., Ye, T., Kim, J. & Mao, C. DNA-directed assembly of single-wall carbon nanotubes. *J. Am. Chem. Soc.* **129**, 8696–8697 (2007).

[30] Li, Y., Han, X. & Deng, Z. Grafting single-walled carbon nanotubes with highly hybridizable DNA sequences: Potential building blocks for DNA-programmed material assembly. *Angew. Chem. Int. Ed.* **46**, 7481–7484 (2007).

[31] Hwang, E.-S. *et al.* The DNA hybridization assay using single-walled carbon nanotubes as ultrasensitive, long-term optical labels. *Nanotechnology* **17**, 3442–3445 (2006).

[32] Yurke, B., Turberfield, A. J., Mills, A. P., Jr., Simmel, F. C. & Neumann, J. L. A DNA-fuelled molecular machine made of DNA. *Nature* **406**, 605–608 (2000).

[33] Seeman, N. C. *De novo* design of sequences for nucleic acid structural engineering. *J. Biomol. Struct. Dyn.* **8**, 573–581 (1990).

[34] Vogel, S. R., Kappes, M. M., Hennrich, F. & Richert, C. An unexpected new optimum in the structure space of DNA solubilizing single-walled carbon nanotubes. *Chem. Eur. J.* **13**, 1815–1820 (2007).

[35] Yurke, B. & Jr., A. P. M. Using DNA to power nanostructures. *Genet. Progr. Evol. Mach.* **4**, 111–122 (2003).

[36] Panyutin, I. G. & Hsieh, P. Kinetics of spontaneous DNA branch migration. *Proc. Natl Acad. Sci. USA* **91**, 2021–2025 (1994).

[37] Christensen, U., Jacobsen, N., Rajwanshi, V. K., Wengel, J. & Koch, T. Stopped-flow kinetics of locked nucleic acid (LNA)-oligonucleotide duplex formation:

studies of LNA-DNA and DNA-DNA interactions. *Biochem. J.* **354**, 481–484 (2001).

[38] Schulman, R. & Winfree, E. Synthesis of crystals with a programmable kinetic barrier to nucleation. *Proc. Natl Acad. Sci. USA* **104**, 15236–15241 (2007).

[39] Barish, R. D., Schulman, R., Rothemund, P. W. K. & Winfree, E. An information-bearing seed for nucleating algorithmic self-assembly. *Proc. Natl Acad. Sci. USA* **106**, 6054–6059 (2009).

[40] Gao, B., Komnik, A., Egger, R., Glattli, D. C. & Bachtold, A. Evidence for Luttinger-liquid behavior in crossed metallic single-wall nanotubes. *Phys. Rev. Lett.* **92**, 216804–1–216804–4 (2004).

[41] Fuhrer, M. S. *et al.* Crossed nanotubes junctions. *Science* **288**, 494–497 (2000).

[42] Bachtold, A. *et al.* Scanned probe microscopy of electronic transport in carbon nanotubes. *Phys. Rev. Lett.* **84**, 6082–6085 (2000).

[43] Postma, H. W. Ch., de Jonge, M., Yao, Z. & Dekker, C. Electrical transport through carbon nanotube junctions created by mechanical manipulation. *Phys. Rev. B* **62**, R10653–R10656 (2000).

[44] Ahlskog, M., Tarkiainen, R., Roschier, L. & Hakonen, P. Single-electron transistor made of two crossing multiwalled carbon nanotubes and its noise properties. *J. Appl. Phys.* **77**, 4037–4039 (2000).

[45] Park, J. W., Kim, J. & Yoo, K.-H. Electrical transport through crossed carbon nanotube junctions. *J. Appl. Phys.* **93**, 4191–4193 (2003).

[46] Lee, D. S., Svensson, J., Lee, S. W., Park, Y. W. & Campbell, E. E. B. Fabrication of crossed junctions of semiconducting and metallic carbon nanotubes: A CNT-gated CNT-FET. *J. Nanosci. Nanotechno.* **6**, 1325–1330 (2006).

[47] Kershner, R. J. *et al.* Placement and orientation of DNA nanostructures on lithographically patterned surfaces. *Nat. Nanotechno.* DOI: 10.1038/NNANO.2009.220 (2009).

[48] Rueckes, T. *et al.* Carbon nanotube-based nonvolatile random access memory for molecular computing. *Science* **289**, 94–97 (2000).

[49] Bachtold, A., Hadley, P., Nakanishi, T. & Dekker, C. Logic circuits with carbon nanotube transistors. *Science* **294**, 1317–1320 (2001).

[50] O'Neill, P., Rothemund, P. W. K., Kumar, A. & Fygenson, D. K. Sturdier DNA nanotubes via ligation. *Nano Letters* **6**, 1379–1383 (2006).

Chapter 2S

Supplementary Materials for

Self-assembly of Carbon Nanotubes into Two-dimensional Geometries using DNA Origami Templates

This chapter is adapted from the following paper with Hareem T. Maune, Robert D. Barish, Marc Bockrath, William A. Goddard III, Paul W.k. Rothemund, and Erik Winfree

Maune HT, Han SP, Barish RD, Bockrath M, Goddard WA, Rothemund PWK and Winfree E, *Nature Nanotechnology*, **5** (1): 61-66 (**2010**)

2S.1 Formation of and purificatio of NL-SWNTs

Design and formation of the linker complex. Oligos were purchased in lyophilized form from IDT DNA. Sequences are below. LNA nucleotides are written as +C+G+A, etc. All other nucleotide are DNA. Labeling domain sequences were computer-optimized (*31*) to minimize sequence complementarity, homology, and melting temperature differences with programs written in MATLAB available at:

http://www.dna.caltech.edu/DNAdesign/

Red linker main strand:

5′ TTTTTTTTTTTTTTTTTTTTTTTTTTTTTTTTTTTTTTTTTTGTTGCGAGGTCTTGC+C+G+A+C+A 3′

Red linker protection strand:

5′ GCAAGACCTCGCAAC 3′

Blue linker main strand:

5′ TTTTTTTTTTTTTTTTTTTTTTTTTTTTTTTTTTTTTTTTTTATACGGGGCTGGTTA+G+G+A+T+G 3′

Blue linker protection strand:

5′ TAACCAGCCCCGTAT 3′

Strands are separately dissolved in water purifie by a Milli-Q unit (Millipore) to form stock solutions at ∼300 μM. A 2 M NaCl stock solution is created and filte ed using 0.22 μm filte s. For the red (blue) linker complex, the main strand and the protection strand are mixed with NaCl stock solution and Milli-Q purifie water to obtain 600 μL of dispersal solution with $\sim$ 33 μM of the main strand, $\sim$ 36 μM of the protection strand, and 0.1 M NaCl; the concentrations of the main and protection strands were chosen to give a

10% excess of protection strand. This solution is put in a 0.6 mL PCR tube and annealed in an Eppendorf Mastercycler from 95°C to 20°C at 1°C per minute. The protection strand/main strand partial duplex has a melting temperature $T_{melting}$ ~50°C in our buffers.

Dispersal of SWNTs. To create the red (blue) NL-SWNTs, ~1 mg of dry HiPco SWNTs are added to 400-600 μL of the dispersal solution in a 1.7 mL PCR tube. The tube is then placed in an ice-water bath and sonicated for ~90 minutes in a Branson 2510 sonicator (100 W). The water level inside the sonication chamber and the position of the PCR tube is adjusted to apply maximum sonication power to the sample. The temperature of the water bath is maintained at ~15 °C. The SWNTs are sonicated until the solution turns a uniform gray color and all the SWNTs are completely solubilized. The solution is then centrifuged at 16,000 g for 90 min at 15°C. Following this step, the supernatant is retained while the insoluble condensate is discarded. This process yields a high concentration of well-dispersed NL-SWNTs as determined by AFM and TEM images.

Removal of excess linker complexes. The dispersal procedure for creating NL-SWNTs leaves a large excess of free linker complexes in solution that needs to be reduced before self-assembly. We apply electrodialysis using a Harvard Apparatus Electroprep system. A 500 μL Teflo fast dialysis tube is fille with NL-SWNT solution and capped at both ends with 50 kD MWCO cellulose ester dialysis membranes. The dialysis tube is then placed in the Electroprep tank. The tank is fille with 0.1 M Na_2HPO_4 buffer (filte ed with a 0.22 μm membrane).

A constant current of 15 to 20 mA is applied across the electrodes of the Electroprep tank. The current is run for 2 hours. The electrodes are then disconnected and the tank is washed. Fresh buffer is added, the direction of the dialysis tube is reversed such that the membrane facing the cathode now faces the anode, and the current is run for another two hours. Buffer exchange and current reversal are repeated two more times before retrieving the NL-SWNT solution (8 hours total of electrodialysis).

To retrieve the NL-SWNTs, the capped dialysis tube is washed using Milli-Q purifie water. It is placed in a beaker with 0.1 M Na_2HPO_4 buffer and ultra-sonicated for 30 seconds to 1 minute in a Branson 2510 sonicator. This releases any NL-SWNTs stuck on the membranes back into the solution contained inside the dialysis tube. The tube is then uncapped and the purifie NL-SWNT suspension is recovered using an appropriate pipette.

The UV absorbance at 260 nm is measured and compared to the absorbance of an unfil tered NL-SWNT sample. We fin that the self-assembly of NL-SWNTs on DNA origami is most efficien when the UV absorbance of the purifie solution at 260 nm is $< 5\%$ of that of the initial solution. If the UV absorbance is higher, or if assembly efficien y is poor, electrodialysis is repeated with fresh filte membranes and buffer. We usually repeat the 8 hour dialysis process three times on the same sample. Immediately after purification NL-SWNT solutions are divided into 50 μl aliquots and stored in a -80°C freezer where they are stable for months. Room temperature storage or 4°C storage causes aggregation and decreased binding to origami after a few days; -20°C might afford stability for weeks or months but we have not made a systematic study of NL-SWNT stability as a function of storage temperature.

The method we used to determine the stopping point for purifi ation only addresses the decrease of the excess linker and does not address the ratio of excess free linker to linkers bound to the SWNTs, which is the more important measure since it determines whether the remaining excess of free linkers is so high that it saturates the hooks on the origami and prevents NL-SWNTS from binding to origami. Thus we used gel-electrophoresis to evaluate this ratio for some batches of NL-SWNTs.

Non-denaturing polyarylamide gel electrophoresis (ND-PAGE) is used to estimate the amount of free linker DNA. Free linkers migrate into the gel where they may be quantified while bound linkers remain stuck on the carbon nanotubes that do not migrate from the well. We use 8% or 10% polyacrylamide (polymerized by 1% by volume of 10% ammonium persulfate (APS) and cross-linked by 0.075% by volume tetramethylethylenediamine

[TEMED]) in a $1\times$ TAE/Mg^{2+} buffer (40 mM Tris-acetate, 1 mM EDTA, 12.5 mM magnesium acetate, pH 8.3). A constant fiel of 8 V/cm is applied across the gel (80 V, 10 cm length, I$\sim$34 mA, 1 mm thick mini-gel) for 3-4 hours while the buffer temperature is kept at 15°C. A 10 base pair ladder (Invitrogen) is used in one of the gel lanes as a length reference. A lane of free linker complexes is included to allow quantitation. Finally, the gel is stained with Sybr Gold (Invitrogen) for 25 minutes and imaged using a Bio-Rad Molecular Imager FX.

Denaturing PAGE (8%, 7 M urea, 175 V, 17.5 V/cm, 60°C, stained similarly to ND-PAGE) was used to estimate the total amount of linker DNA in the sample after the electrodialysis procedure. The idea is that strong denaturing conditions and high temperature* detach the linkers from the nanotubes, so that the total can be measured. From the total and the free linker concentration, we estimate the amount of linker bound to the carbon nanotubes ($\mathrm{bound} = \mathrm{total} - \mathrm{free}$).

The amount of free and SWNT-bound linkers varies between different preparations of NL-SWNTs; bound linker typically ranged from $\sim$ 100 nM to 1 μM. As a specifi example, for the batch of blue SWNTs used in Fig. 2, we estimated that the concentration of linker bound to SWNTs was 420 nM and the concentration of free linker was 120 nM, even after it had undergone a few freeze thaw cycles (and been used in successful experiments). This represents a free:bound linker ratio of $\sim$1:3. If the ratio is too high, then presumably free linker will bind all hook sites and prevent SWNTs from binding. Because NL-SWNTs bind origami at multiple sites, some poisoning of these sites by free linker may be tolerated. We have not explored the highest ratio of free:bound linker that is acceptable.

*Here a fiel strength of 17.5 V/cm seemed to be more effective at detaching linkers than 8 V/cm. This could have been caused incidentally by greater heating, or perhaps the somewhat elevated fiel played a direct role since the carbon nanotubes do not migrate in the gel and are not free to move with the linkers.

2S.2 Design, assembly, and purificatio of the DNA template

Tall rectangle origami templates. The DNA origami used in our experiments is a modifie version of the "tall rectangle" designed by Rothemund (Supplementary Information Figs. S36 and S48 in (*20*)). The sequences for the original origami are shown in Fig. S48 of (*20*). We modifie the origami as shown in Fig. S1. Specificall , we replaced particular DNA staples with the strands listed in Figs. S2 and S3. Their names, listed in the "Position and sequence" columns, correspond to the names of the original staples shown in Rothemund's Fig. S48 (*20*)but have "FHook1" or "FHook2" added. In general their sequences differ from the original staples by the addition, on the 3' end, of (1) a 4 thymine fl xible linker and (2) an appropriate hook sequence.

The linker + red hook sequence is:

5′ TTTTTGTCGGCAAGACCTCGCAAC 3′

This corresponds to the red linker sequence:

5′ GTTGCGAGGTCTTGCCGACA 3′

The linker + blue hook sequence is:

5′ TTTTCATCCTAACCAGCCCCGTAT 3′

This corresponds to the blue linker sequence:

5′ ATACGGGGCTGGTTAGGATG 3′

The staples which are used for the blue column of hooks are actually not quite simple catenations of original staples with the linker and blue hook sequence. The domain by which these staples bind the origami scaffold strand is actually shifted 5 nucleotides with respect to the binding domain which is used for the original staples—this can be observed in Fig. S1. It means that (1) the scaffold binding domain of each staple in the blue col-

umn is actually a composite of two staples in the same column in the original origami, 5 nucleotides from one staple and 27 nucleotides from another and (2) one of the sequences (t1r0g-FHook2) does not actually bear a blue hook—instead it is a staple on the top edge of the origami that had to be modifie to accomodate the shift in strand ends implied by (1).

Origami-nucleated DNA/ribbon templates. We created a larger DNA template from the DNA origami by growing a periodic structure from the edge of the DNA origami using DNA tiles. The structures, known as zig-zag ribbons, were fi st described in (*34*) and their nucleation and growth from origami was shown in (*35*). The DNA tiles constituting the ribbon are each made from four single DNA strands: two long strands (37 nt) and two short strands (26 nt), which displaying 5-base sticky ends for binding with other tiles. A schematic for a tile attached to the origami is present at top, in Fig. S1. Tiles comprise of just two DNA helices and are much smaller ($\sim$12 nm$\times$4 nm) than a DNA origami ($\sim$ 95 nm $\times$ 75 nm), but they can assemble into a much larger periodic ribbons, which are typically from 4-16 tiles wide and hundreds of tiles long. The long edge of the tall rectangle origami has 32 helices, so up to 16 DNA tiles can be fi onto the edge of the origami by using a set of adapter strands (*35*). Here we used 16-tile wide ribbons everywhere except for an experiment documented by Fig. S5d,h which used an 8-tile wide ribbon. Because the origami forms at higher temperatures than the assembly of tiles into zig-zag ribbons, origami serve as good nuclei for the growth of zig-zag ribbons—a cooled mixture of their component strands forms products that are almost entirely composed of DNA origami with crystalline zig-zag ribbons grown from their edge. The resulting ribbons are $\sim$100 nm wide and typically 500 nm to 1 μm long.

Ribbons coupled to origami are a highly visible marker for the orientation of the DNA origami (red face up or blue face up), even when imaging resolution is low. Patterns of hairpins on the DNA origami could have served to disambiguate orientation, but experiments analysis would have been much more challenging since they require higher reso-

lution imaging. Qualitatively, more SWNT/DNA template structures were observed post-assembly when DNA origami/ribbon structures were used rather than origami alone; but we have not quantifie this effect nor explored its mechanism. (There are many possibilities—larger DNA nanostructures stick more strongly to mica, for example.)

DNA origami/ribbon template assembly and ligation. Short DNA strands were purchased from IDT DNA. Single-stranded M13mp18 bacteriophage DNA, T4 DNA Polynucleotide Kinase, and T4 DNA Ligase were purchased from New England Biolabs. DNA strands and buffers are mixed to obtain 50 μL of the following "assembly mixture". (Amounts of components are given as either the fina concentration of that component, or the volume of that component added.)

1× TAE Mg^{2+} (12.5 mM Mg-acetate, 40 mM Tris-acetate, 1 mM EDTA, filte ed with a 0.22 μm filte)
1×T4 DNA ligase buffer (50 mM Tris-HCl, 10 mM $MgCl_2$, 1 mM ATP, 10 mM Dithiothreitol)
10 nM M13mp18 bacteriophage DNA
50 nM of each origami staple
10 nM of each DNA ribbon adapter strand
100 nM of each zig-zag ribbon tile
3 μL T4 Polynucleotide Kinase

The above reaction mixture is placed in a 0.6 mL PCR tube and incubated using the following temperature profile

1) 37°C for 1 hour
2) 65°C for 20 minutes

3) 90°C for 5 minutes

4) 90°C to 40°C at 1°C per 1 minute

5) 40°C to 25°C at 1°C per 1 hour

The assembly mixture is then diluted and mixed with additional components to form 500 μL of the following "ligation mixture":

1× TAE Mg^{2+}

1× T4 DNA ligase buffer

25 μL T4 DNA ligase

50 μL assembly mixture

Ligation is allowed to proceed in the above solution at room temperature for 12 to 24 hours.

Purificatio of DNA origami/ribbon templates. Assembled and ligated templates are separated from other reaction products using Millipore Microcon YM-100 spin filte s (100 kD MWCO). 100 μL of the ligation mixture is gently mixed with 300 μL of sodium-based assembly buffer (0.75 M NaCl, 0.01 M Na_2HPO_4, pH ∼8 at 25°C, 0.22 μm filte ed) and transferred to a YM-100 spin filte according to the product's instructions. The filte is spun in an Eppendorf temperature-controlled centrifuge at 4°C and 1000 g for 12 min. 400 μL of assembly buffer is added to the retentate in the spin filte and gently mixed using a 1000 μL pipette. The filte is spun again at 4°C and 1000 g for 8 minutes. The retentate is then recovered according to the product's instructions. The recovery should yield about 100 μL of solution. (Note that the spin time for the second filt ation can be adjusted to obtain approximately the desired volume). The recovered solution contains ∼1 nM concentration of DNA templates in sodium buffer. We have found that without this buffer exchange, the presence of magnesium at millmolar concentrations causes precipitation of

NL-SWNTs when DNA templates are later mixed with the NL-SWNTs. The elimination of free assembly components was verifie using ND-PAGE analysis. (Origami/ribbons do not migrate in ND-PAGE gels, but excess staples which we are interested in measuring, do.) Ligated origami/ribbon templates remain stable in the sodium-based assembly buffer, as evidenced by subsequent AFM.

2S.3 Assembly of NL-SWNTs with origami-ribbon templates

We combined NL-SWNTs with origami-ribbon templates in two different types of experiments: (1) the binding of red NL-SWNTs or blue NL-SWNTs *independently* with origami-ribbon templates bearing cross patterns of red and blue hooks to measure the specificit of binding and fidelit of alignment to the hooks and (2) the binding of red NL-SWNTs and blue NL-SWNTS *simultaneously* with origami-ribbon templates bearing cross patterns of red and blue hooks to create cross-junctions. In both cases, the basic recipe (with amounts of components given as either the fina concentration of that component, or the volume of that component added) for combining NL-SWNTs with origami-ribbon templates is the same:

$\sim$0.75 M NaCl

$\sim$0.01 M Na_2HPO_4

10 μL of purifie DNA templates

0.5 to 3 μL of red NL-SWNTs

0.5 to 3 μL of blue NL-SWNTs

This mixture (pH $\sim$8) is kept at 25°C for 10 to 100 minutes and then deposited directly on the desired substrate for characterization. We have not systematically studied the kinetics but binding times between 30 and 35 minutes appear to give the best results under our conditions.

A couple comments:

1. Nanotubes probably attach to DNA templates via multiple hook-linker interactions, but the details of the attachment process remain uncertain. For example, multiple linkers could fi st attach to multiple DNA hooks via their toeholds before each hook-linker pair completes the branch migration process. Alternatively, branch migration could occur at a single attachment site followed by alignment via additional attachments. Further work is required to fully understand the attachment processes.

2. We do not have a direct method for quantifying the concentration of post-purificatio origami-ribbon templates and NL-SWNTs in the assembly solution. However, assuming every M13mp18 DNA strand results in an assembled template, and every template is retained durning purification then we would have $\sim$0.5 nM of origami-ribbon templates in the assembly mixture. $7\mu\mathrm{m}\times7\mu\mathrm{m}$ topographic flui mode AFM scans for origami/template/NL-SWNT constructs in experiments with a single type of tube (red or blue) typicially show 2 to 3 SWNTs for every visible DNA template on the mica surface. Thus it is plausible (if binding rates of NL-SWNTs and templates to the mica are similar) that the concentration of NL-SWNTs could be in the low (say 1-2) nanomolar range.

2S.4 Atomic force microscopy of constructs under flui

Deposition on mica substrates. After assembly, 5 μL of the assembly solution is added to a piece of freshly cleaved mica. Following this, a 40 μL drop of 1$\times$ TAE/Mg^{2+} was added on top. Finally, a 20 μL drop of 10 mM nickel (II) acetate (0.22 μm filte ed) was added. The sample was then immediately imaged with an AFM. Fig. S5 shows examples of SWNT cross-junctions deposited on mica and imaged using tapping mode AFM under fluid AFM characterization suggests that the asymmetry of the constructs may play a role

in deposition. In the same experiments we used to measure the alignment of red or blue nanotubes to their respective hook arrays, we also counted the number of occurences of DNA origami/ribbon constructs with their red face down or blue face down:

	undecidable	blue face down	red face down	total
red tubes attached	16 (11%)	29 (19%)	106 (70%)	151
blue tubes attached	9 (8%)	14 (12%)	97 (80%)	120

There is a bias (70–80%, when 50% was expected) for an origami/ribbon construct to have its red face down and its blue face up, regardless of whether it is bound by a blue or a red tube. While the origami are symmetric at the coarse scale of their overall shape, they are highly asymmetric at a smaller length scale; almost all of the nicks in the phosphate backbone (except for at the row of blue hooks) of the origami we used fall on the red face of the origami. Thus one might expect that the origami can assume a configu ation with the red face being convex much more easily that it can assume a configu ation with the blue face being convex; if the red face is convex, the nicks can open and relieve strain, if the blue face is convex, no such strain relief can occur. Perhaps this plays a role in the asymmetric deposition rate. Further work will be required to confi m and understand this deposition effect.

Collection of alignment statistics using atomic force microscopy. To collect alignment data, we prepared DNA origami/ribbon templates with the cross-junction hook pattern. The templates were mixed with either red or blue NL-SWNTs *independently*, and annealed according to the standard procedure, and deposited on mica (as described above). A Veeco Multimode AFM with a Nanoscope IIIa controller was operated in tapping mode with a flui cell. The imaging parameters were the same as described in (*30*). All images were collected at 512 $\times$ 512 pixel resolution using a scanning speed between 1.0 and 6.0 lines per second. A 10 μm $\times$10 μm or 7 μm $\times$7 μm area scan was fi st taken at a random

location on mica. Every visible DNA template in that area was scanned in greater detail until the template quality, template orientation and SWNT alignment angle could be clearly established (usually requiring a 500 nm$\times$ 500 nm or smaller scan area).

2S.5 Electronic characterization of cross-junctions

Deposition of SWNT/DNA template constructs on SiO_2 substrates. A $\sim$ 1 cm $\times$ 1 cm piece of p-doped Silicon wafer with a thermally grown SiO_2 layer (300 nm or 1 μm) was cleaned with dichloroethane (DCE) and isopropanol (IPA) in an ultrasonicator bath. The wafer was then exposed to O_2 plasma in an Anatech SP100 plasma system (Anatech) at 80 W, 200 mTorr for 3 minutes. A 5 μL solution containing SWNT/DNA template constructs was then immediately deposited onto the wafer surface followed by a 7 μL drop of 10 mM Ni^{2+} acetate solution and 40 μL drop of 1$\times$ TAE/Mg^{2+}. After 1 hour of incubation at room temperature, excess salt residue was washed away using 0.1 M ammonium acetate, (pH 6 at 25°C). The wafer was dried using compressed nitrogen gas. Deposited SWNT/DNA template constructs could then be imaged by tapping mode AFM on the dry silicon substrate (Fig. S6) and by scanning electron microscope (SEM) albeit with lower resolution. Although the ribbons on DNA templates appeared twisted and folded and under dry mode AFM, cross-junction geometry of SWNTs was typically intact (Fig. S6). Within a 400 μm^2 area of the silicon wafer, we typically found 5 to 10 self-assembled SWNT cross-junctions.

Lithographic fabrication of contacts to the SWNT cross-junctions. Positions of self-assembled SWNT cross-junctions are located on the Si/SiO_2 substrate, with respect to the pre-fabricated reference markers, using an AFM. Standard electron-beam lithography techniques are employed to make electrical contacts to the nanotubes. Briefl , a bi-layer resist consisting of 250 nm LOR 3B lift-off resist (MicroChem, baked at 190°C for 1–3 minutes) and 150 nm PMMA C2 (MicroChem, baked at 160°C for 10–15 minutes) are spun on

the sample. Electrode patterns are written using a Quanta 200F (FEI tools) equipped with nanometer pattern generation system (NPGS). After the development of the resist, the sample is rinsed in "DNA AWAY" (Molecular BioProducts) for 6 seconds, washed with DI water, rinsed with HCl for 6 seconds and washed again with DI water. The rinsing steps have three purpose: fi st, to prime the surface (HCl has been shown to improve the hydrophilic nature of the silicates by hydrolyzing them, therefore, priming the metal wetting properties of the substrate surface), second, to degrade substrate bound DNA so that it does not adversely affect the adhesion of metal electrodes to the substrate and third, to remove DNA from NL-SWNTs at contact regions so that it does not adversely affect the metal-SWNT junction. (Note that at this point in the process, NL-SWNTs near the cross-junction and DNA templates are presumably protected from the rinses by resist. However, we found that we could not resolve the DNA templates by AFM post-liftoff.) We do not know whether the DNA on the NL-SWNTs in the contact regions is fully degraded or whether the residue of degraded DNA is washed away. However, NL-SWNTs treated in this manner exhibit better conductivity, presumably due to better electrode-nanotube contact. Electrodes are then thermally evaporated via e-beam evaporator (Temescal BJD 1800). Each electrode has $\sim$5 nm thick Pd layer contacting the SWNT and and 40 nm Au layer protecting the Pd contact. (Palladium was chosen over gold or chromium because palladium has better wetting properties than gold and it has been shown to produce a smaller Schottky barrier at contacts with SWNT than does chromium because its work function better matches that of carbon nanotubes. Further, we chose not to apply a standard high temperature annealing protocol [*e.g.* 600°C for 30 minutes under argon] in attempt to preserve the DNA templates.) Finished devices are shown in Fig. 3 and supplementary Figs. S8 and S9.

After the resist lift-off process, the device is mounted in a chip holder and electrical contact between the bonding pads and holder are made using a wire bonder. The chip holder is inserted in a socket connected to our measuring setup.

In all, we attempted fabrication on 23 cross-junctions. Of these, six had measurable

conductance in one or both nanotubes, three had fiel effect transistor (FET) like behavior. Of the three FET-like devices, one had stable properties throughout the period of measurement.

Device characterization. All devices were characterized using similar procedures. Figs. 3 and S8 show the measurement setup and results of the stable FET-like device (giving similar results over tens of measurements). Fig. S9 shows the measurement setup and results for an additional FET-like device, which was short-lived (providing just the three sweeps in Fig. 9).

Outputs from a digital-to-analog converter (DAC) card (National instruments) in a PC were used to maintain voltages between different electrodes. Currents were measured via a current pre-amplifie which also served as a virtual ground. Our four-electrode setup allowed us to measure each SWNT independently and determine its room temperature properties. In general, for a given device, we fi st measured the two terminal current fl w across each nanotube as a function of voltage (the other nanotube is left floating to see if good contacts had been made. Then IV curves were measured as a function of back-gate voltage to determine if the SWNT was metallic or semiconducting (except in cases where the back-gate failed, as in the case of the stable device). Based on these IV curves (and if there was potential for FET-type behavior) we chose one SWNT as the channel, and the other as the gate channel, and assigned the four electrodes as source (S), drain (D), gate (G) and auxiliary gate (g) electrodes. After picking the channel and gate nanotubes, we then measured the inter-nanotube tunneling current as a function of applied gate voltage. Using this data, we pick a suitable range of gating voltage V_G and measure (a) I_{SD} at fi ed V_{SD} as a function of V_G and (b) I_{SD} at fi ed V_G as a function of V_{SD}. During these measurements, one terminal of the gate SWNT (G) is connected to the applied voltage while the other terminal (g) is left floating To protect the device from the gate's insulating layer breakdown etc., the voltage, V_G, is applied through a 100 MΩ resistor which, along

with the gate capacitance, acts as a low-pass filte .

In particular, Fig. 3 shows the stable device and its function as a FET; S8 shows more detailed data on its electronic properties. Two electrode measurements across each SWNT suggested that one SWNT (from source electrode S to drain electrode D) was a p-type semiconductor and the other SWNT (from gate electrode G to auxillary electrode g) was either metallic or semiconducting. (For this particular device, the back-gate was not functioning.) We chose the SWNT across electrodes S and D to be the conducting channel due the much lower apparent resistance of that channel ($\sim$2 MΩ, see Fig. 8). The SWNT across electrodes G and g was chosen to be the gate channel due to that channel's high resistance ($\sim$6 GΩ channel resistance, see Fig. 8b). However, the inter-nanotube current measurement between electrodes G and D indicates that the resistance ($\sim$3 MΩ resistance for $V_{GD} < -0.5\ V$, Fig. 8c) through the gate nanotube and electrode G (where the gating voltage is applied) may be far lower than 1 GΩ at negative gate voltages.

Measurement of the inter-nanotube tunneling current (Fig. S8c) also shows an insulating region between $V_{GD} \sim -0.5$ V to 0.5 V. This could be due to insulation by DNA or other organic residue or an inter-nanotube Schottkey barrier. We chose to sweep V_{GD} in this range to characterize FET-type gating of the current channel and confi med the identity of the blue SWNT as a p-type semiconductor.

The gate electrode G is in close proximity ($\sim$70 nm) to the conduction channel SWNT and may contribute to the current switching behavior shown in Fig. 8d. Further experiments are needed to understand the fiel effect gating mechanism and to decouple the contribution of the SWNT gate from that of gate electrode.

2S.6 Open questions.

The protocols described in this paper describe sufficien conditions for the creation of SWNT cross-junction devices. However, there remain open questions concerning what the simplest necessary procedure for creating cross-junction devices might be, as well as what

parts of the protocol are most important for success:

1. *LNA versus DNA toeholds.* We have found that, under the conditions reported above, 5 nucleotide LNA toeholds give good results. We have been unable to fin conditions under which 7 and 8 nucleotide DNA toeholds give good results; they resulted in cross-linking of SWNTs or aggregation. For some experiments, 5 nucleotide DNA toeholds were used and SWNT-origami binding and alignment was observed but with poor yield. However, conditions and sequences for the use of 5 nucleotide DNA toeholds were not optimized and so conditions under which less expensive, short, DNA toeholds (5 or 6 nucleotides) give good yields of cross-junctions may be found. In addition to its role as a stronger binding toehold, LNA may also be advantageous in this system because its constrained backbone may give it a lower intrinsic affinit for SWNTs; this idea has also not been tested.

2. *Plain origami versus origami with ribbons.* The use of ribbons with DNA origami appeared to increase the yield of observed structures. However we have not rigorously quantifie this effect, and we have obtained some aligned SWNTs and cross-junctions on origami alone. Other protocols may be better suited for the use of DNA origami alone, for example the deposition of DNA origami on surfaces before their assembly with SWNTs.

3. *Hooks with versus hooks without poly-T segments. Yield and alignment as a function of fl xibility.* We added poly-T segments between staples and hooks with the idea that they would facilitate SWNT alignment by acting as joints or spacers. However, we did not test the effica y of assembly without poly-T segments. This is part of a larger set of questions about the degree of alignment as a function of hook spacing, linker length, and hook length. The effects of such variables on the quality of alignment are not understood.

4. *Schemes using strand displacement versus other protected schemes without strand*

displacement. Here we use a protection strands to prevent the labeling domain from binding to the SWNT to which it is attached (via the linker domain) or from cross-linking this SWNT with other SWNTs. The 5-nucleotide toehold is available for binding the hook and initiation of strand displacement. The question is whether toe-hold binding to the hook is itself sufficien to align a SWNT on an origami (since multiple toeholds can bind an origami at once). Initial experiments using hooks that are composed of only the 5 nucleotide sequence complementary to the toehold (and are thus incapable of displacing the protection strand by branch migration) indicated that binding and alignment can occur without a complete 20 nucleotide labeling do-main but these experiments have not been optimized or compared quantitatively to results with the full labeling domain. Note that in these experiments with short hooks, the protection strand and duplex domain in the linker complex remain intact—thus while displacement of the protection strand may not be necessary, the rigid duplex it forms may be important in holding the toehold away from the SWNT.

5. *SWNT alignment as a function of NL-SWNT purity.* While preparations of NL-SWNTs with ratios of free linker to bound linker as high as ∼1:3 gave good align-ment of NL-SWNTs to origami templates, NL-SWNTs with a lower amount of free linker might give still better results, since free linkers presumably bind hooks on DNA origami and render them ineffective as binding sites for NL-SWNTs.

6. *Why are the ends of nanotubes so often flus with the edges of DNA origami?* In perhaps 25% of cases nanotubes bind their complementary hook arrays so that one end of the nanotube is at the end of a hook array. It will be interesting to know how statistically significan this effect is, and if it is a real effect, what is the the mechanism behind it. There are many instances where it would be desirable to have nanotube ends meet rather than having nanotubes cross and so harnessing the effect could be very useful.

7. *What is the detailed structure of the linkers on the SWNT and how does this affect alignment?* It is unclear what the density of the linkers are on the NL-SWNTs, whether they close packed or have gaps, whether their dispersal domains wrap the SWNTs helically or not, whether the linkers dynamically rearrange on the SWNT surface or not, what the number of labels available for binding hooks is, or how any of these variables ultimately effect the alignment of SWNTs on DNA origami.

8. *What is the nature of the barrier between SWNTs in our system? Can the intervening DNA layer act as a dielectric?* So far, the effect of the DNA linkers and DNA origami template between carbon nanotubes is unclear. In the device best studied, AFM showed no residual origami template at the junction and other explanations for the observed barrier (e.g. a Schottkey barrier) are possible. However, DNA residue from the origami may have remained between the tubes, and the SWNTs were themselves coated with DNA linker complex. Lithographic steps to add metal electrodes left visible DNA in some cases; this suggests that fabrication might be optimized to leave behind origami templates. An important geometry to test is that of crossed carbon nanotubes bound to the same side of the origami (which, in principle, should not be difficul to synthesize) that should have less DNA between them (only the DNA linkers) and should thus exhibit a different distribution of device characteristics than the case with crossed carbon nanotubes on opposite sides of the origami. An important control will be devices that have been intentionally stripped of DNA. Improvements in locating and wiring up devices seem necessary to collect enough device data to address this question.

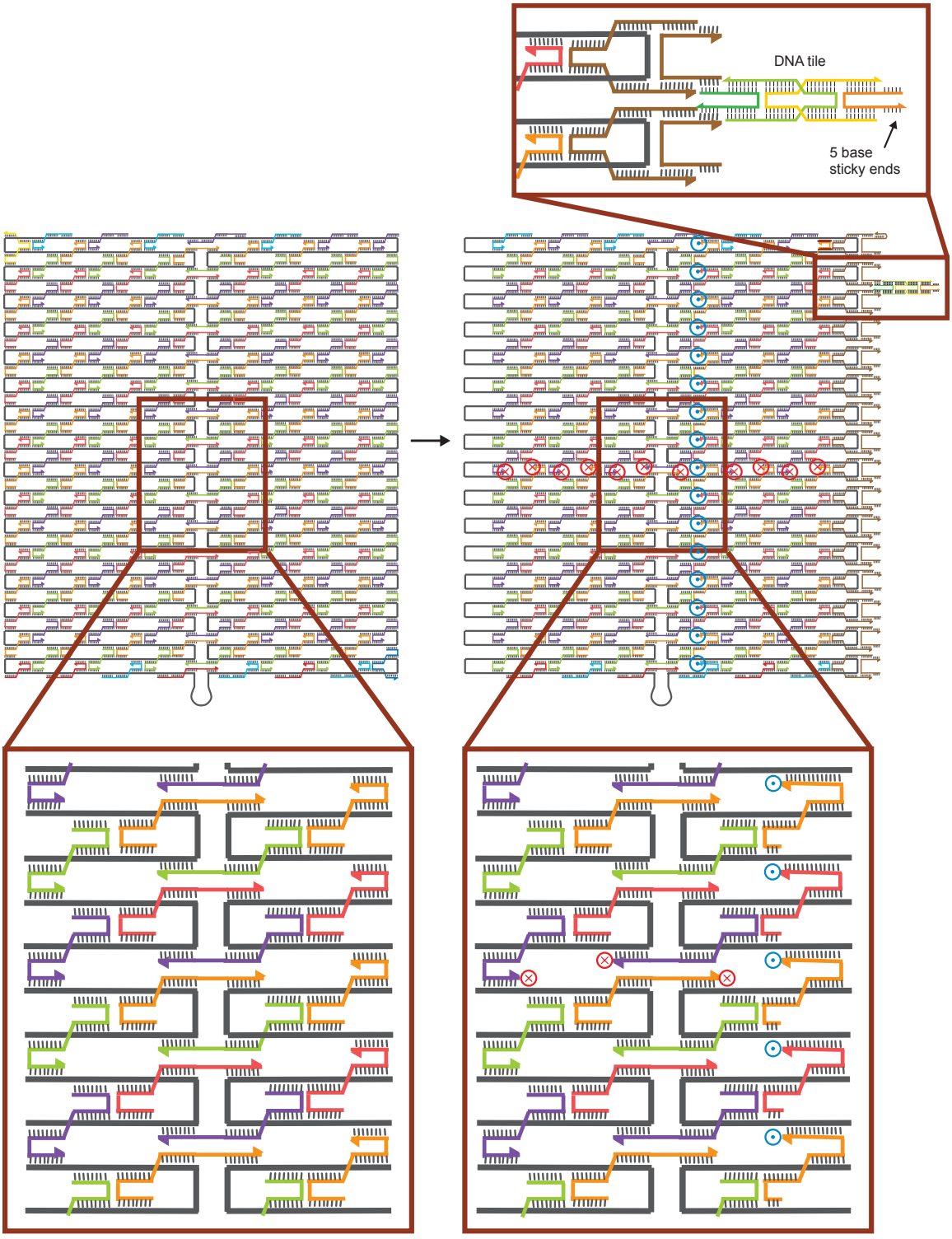

Figure S1: A schematic for the original "tall rectangle origami" (Supplementary Figs. S35 and S48 in (*20*)) is compared with a schematic of the modifie rectangle origami we used as a template, at right. In our new design the leftmost column of staples was removed to decrease origami aggregation. The rightmost column of staples was replaced with tile adapter strands (Fig. S2 and S3) for nucleating zig-zag DNA ribbon growth. Blue dotted circles indicate blue DNA hooks extending out of the page. Red crossed circles indicate red DNA hooks extending into the page.

Plate position	Position and sequence	Sequence
B1	t-5r18e-FHook1	5' - TATATTTTCATACAGGCAAGGCAAAGCTATATTTTTTGTCGGCAAGACCTCGCAAC - 3'
C1	t-3r18e-FHook1	5' - CAACGCAAAGCAATAAAGCCTCAGGATACATTTTTTTGTCGGCAAGACCTCGCAAC - 3'
D1	t-1r18e-FHook1	5' - CTGTAATAGGTTGTACCAAAAACACAAATATATTTTTGTCGGCAAGACCTCGCAAC - 3'
E1	t3r18e-FHook1	5' - TATGTAAAGAAATACCGACCGTGTTAAAGCCATTTTTGTCGGCAAGACCTCGCAAC - 3'
F1	t5r18e-FHook1	5' - TAACCTCCAATAAGAATAAACACCTATCATATTTTTTGTCGGCAAGACCTCGCAAC - 3'
G1	t-5r16f-FHook1	5' - ATATAATGGGGGCGCGAGCTGAAATTAACATCTTTTTGTCGGCAAGACCTCGCAAC - 3'
H1	t-3r16f-FHook1	5' - TGCAACTAGGTCAATAACCTGTTTAGAATTAGTTTTTGTCGGCAAGACCTCGCAAC - 3'
A2	t-1r16f-FHook1	5' - TCCATATATTTAGTTTGACCATTAAGCATAAATTTTTGTCGGCAAGACCTCGCAAC - 3'
B2	t1r16f-FHook1	5' - AGAGGCATACAACGCCAACATGTATCTGCGAATTTTTGTCGGCAAGACCTCGCAAC - 3'
C2	t3r16f-FHook1	5' - TAAAGTACCAGTAGGGCTTAATTGCTAAATTTTTTTTGTCGGCAAGACCTCGCAAC - 3'
D2	t5r16f-FHook1	5' - CCAGACGACAAATTCTTACCAGTAGATAAATATTTTTGTCGGCAAGACCTCGCAAC - 3'

Figure S2: The modifie staples used to display the red ssDNA hooks.

Plate position	Position and sequence	Sequence
A7	t1r0g-FHook2	5' - TGATATAAGTATAGCCCGGAATAGGTG - 3'
B7	t1r2e-FHook2	5' - GTCGGTAATAAGTTTTAACCCGTCGAGAGGGTTTTTCATCCTAACCAGCCCCGTAT - 3'
C7	t1r4e-FHook2	5' - GAGACCCTCAGAACCGCCACGTTCCAGTAAGCTTTTCATCCTAACCAGCCCCGTAT - 3'
D7	t1r6e-FHook2	5' - GAGGTAGCACCATTACCATATCACCGGAACCATTTTCATCCTAACCAGCCCCGTAT - 3'
E7	t1r8e-FHook2	5' - ACGTAAAGGTGGCAACATACCGTCACCGACTTTTTTCATCCTAACCAGCCCCGTAT - 3'
F7	t1r10e-FHook2	5' - AAAGATAACCCACAAGAATAAGACTCCTTATTTTTTCATCCTAACCAGCCCCGTAT - 3'
G7	t1r12e-FHook2	5' - TGCACGCTAACGAGCGTCTGAACACCCTGAACTTTTCATCCTAACCAGCCCCGTAT - 3'
H7	t1r14e-FHook2	5' - CTGACCAAGTACCGCACTCTTAGTTGCTATTTTTTTCATCCTAACCAGCCCCGTAT - 3'
A8	t1r16e-FHook2	5' - TTATTTCGAGCCAGTAATAAATCAATAATCGGTTTTCATCCTAACCAGCCCCGTAT - 3'
B8	t1r18e-FHook2	5' - GAAAATTTCATCTTCTGACAGAATCGCCATATTTTTCATCCTAACCAGCCCCGTAT - 3'
C8	t1r20e-FHook2	5' - AATCGTCGCTATTAATTAAATCGCAAGACAAATTTTCATCCTAACCAGCCCCGTAT - 3'
D8	t1r22e-FHook2	5' - CGTTCGGGAGAAACAATAACAGTACATAAATCTTTTCATCCTAACCAGCCCCGTAT - 3'
E8	t1r24e-FHook2	5' - AATGAACAAAGAAACCACCTTTTCAGGTTTAATTTTCATCCTAACCAGCCCCGTAT - 3'
F8	t1r26e-FHook2	5' - GCAAATCAATATCTGGTCACCCGAACGTTATTTTTTCATCCTAACCAGCCCCGTAT - 3'
G8	t1r28e-FHook2	5' -CAGATACGTGGCACAGACATGAAAAATCTAAATTTTCATCCTAACCAGCCCCGTAT - 3'
H8	t1r30e-FHook2	5' - AGCCCTGAGTAGAAGAACTACATTCTGGCCAATTTTCATCCTAACCAGCCCCGTAT - 3'
A9	t1r32h-FHook2	5'-TACAGGGCGCGTACTATGGTTGCTAATTAACCGTTGTTTTTCATCCTAACCAGCCCCGTAT-3'

Figure S3: The modifie staples used to display the blue ssDNA hooks.

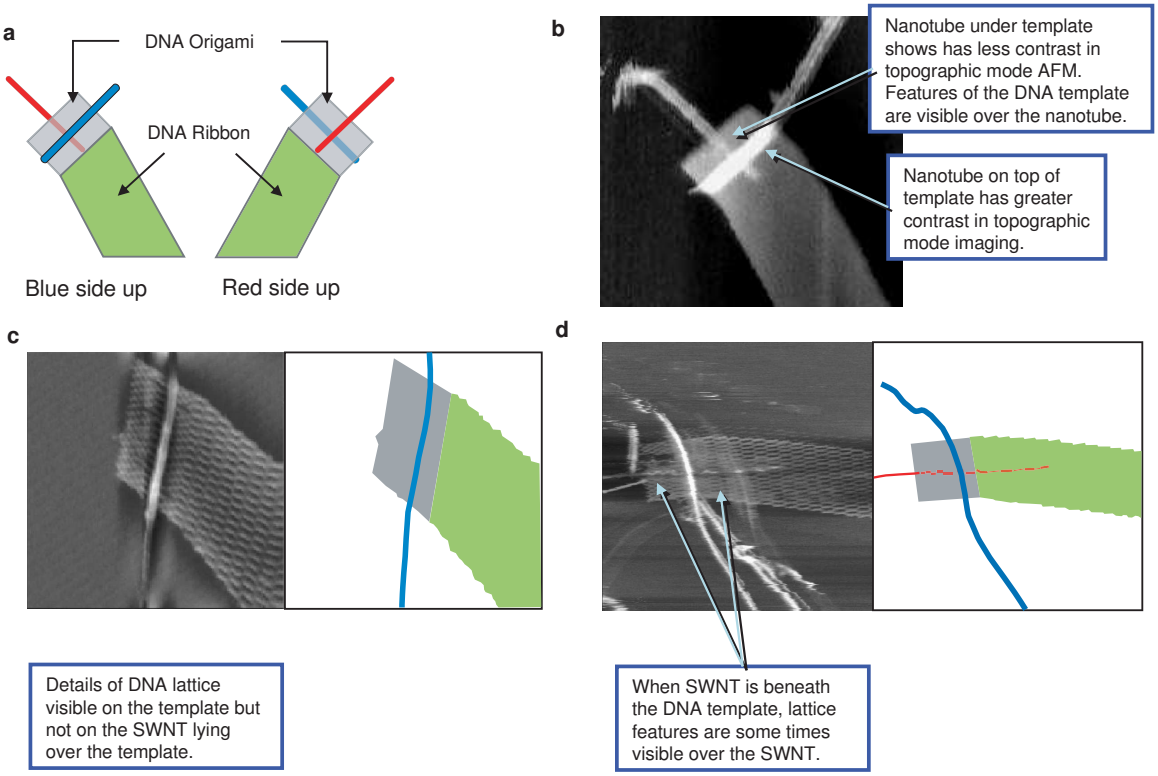

Figure S4: Understanding the orientation of SWNT/origami/ribbon constructs. **(a)** Origami/ribbon constructs have a handedness that allows one to distinguish which face of the origami is facing up, and which is facing down on the substrate. This allows the relative orientation of a SWNT and an origami to be measured over a 180° range rather than the 90° range possible if the origamis were used alone, without further markings. (It turns out that the alignment distributions we measure are roughly symmetric about their peak, and so in the end it would not have changed the conclusions of the alignment data, but this might have not been the case.) **(b)** Another cue which aids in understanding the structure of the cross-junctions is the topograhic height constrast of the two different nanotubes. In general the nanotube under the template images with lower height contrast than the nanotube on top of the origami. **(c)** and **(d)** Still a third cue is the "texture" of the carbon nanotube. Nanotubes that are apparently on top of the origami have a smooth (yet noisy) texture do the blue nanotubes in (c) and (d). When imaged with very high resolution, nanotubes apparently underneath the origami sometimes have a dashed or periodic appearance that seems correlated to the fin pe-riodic structure of the origami or the ribbon, as does the red tube in (d). AFM height contrast and the texture of the nanotube are secondary cues as to the position (over or under the origami) of the nanotubes. They are not always observed but when observed are typically consistent with the position derived by the orientation of the origami/ribbon. Rarely they disagree—this may indicate nonspecifi binding of blue tubes to red hooks or red tubes to blue hooks, which may explain some of the few nanotubes that have an incorrect orientation in the alignment distributions in Fig. 2.

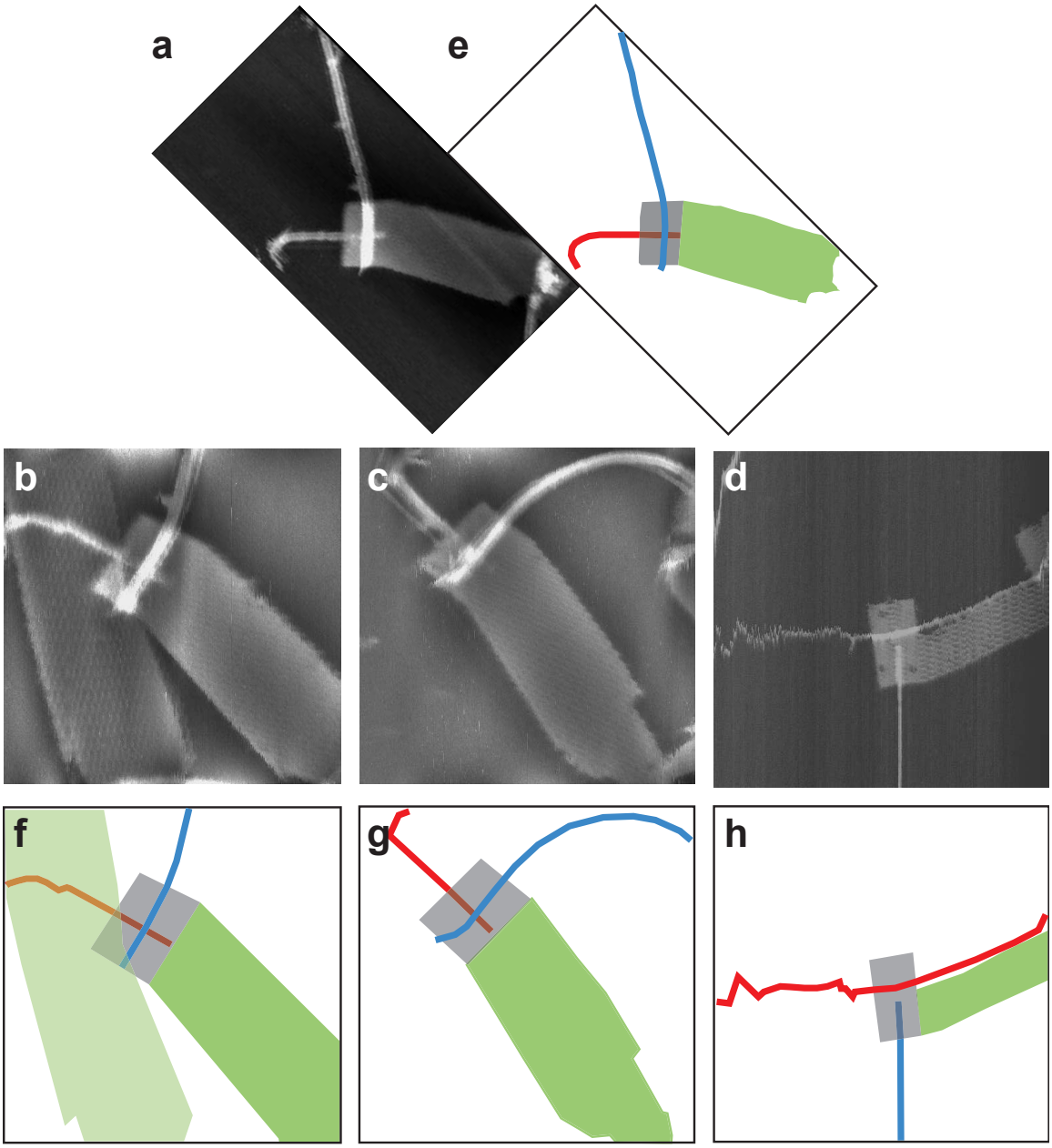

Figure S5: **(a)–(d)** Topographic tapping mode AFM images of the self-assembled SWNT cross-junction deposited on a mica substrate and kept under fluid (a)–(c) show cross-junctions on origami attached to 16-wide tile-wide ribbons. (d) shows a cross-junction on an origami attached to an 8-tile wide ribbon. The blue nanotube is under the origami according to the ribbon orientation; this is consistent with the faint details of the origami fin structure that may be seen on top of it. **(e)–(h)** Interpretations of (a)–(d). Red and blue SWNT are indicated, origami are gray, and ribbons are green. SWNTs that apparently run origami under or ribbons have had their color deemphasized. In (f) a ribbon that has fallen on top of part of the origami and red SWNT is represented in light green. (Details of the light green ribbon can clearly be seen in the AFM coincident with the red nanotube, which is why we interpret it as being on top of the red SWNT.)

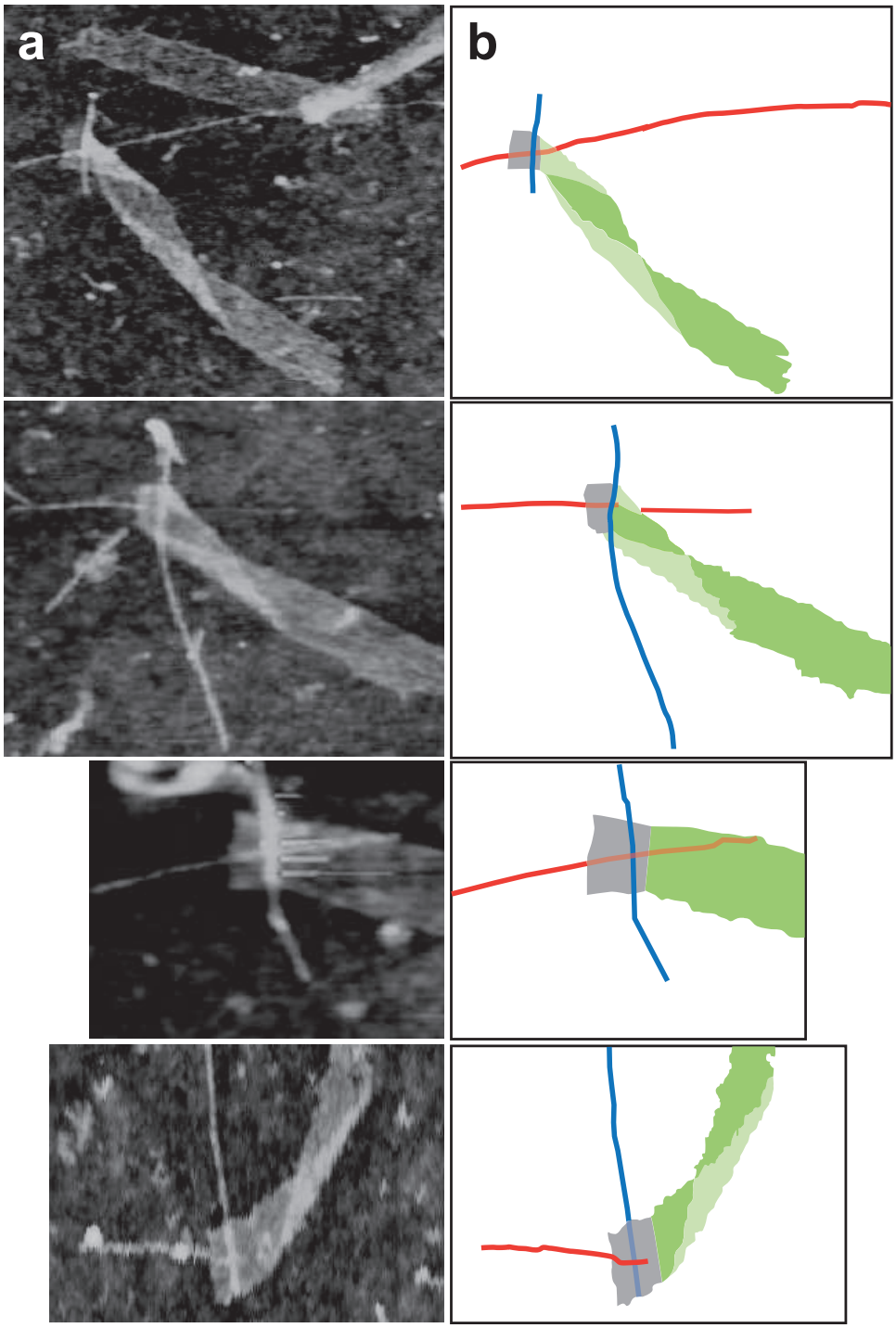

Figure S6: **(a)** topographic AFM images of the self-assembled SWNT cross-junctions deposited on a silicon substrate. The image is taken on a dry substrate in tapping mode. The width of the ribbons is ∼100 nm. **(b)** interpretations of the AFM images in (a). Blue and red SWNT are indicated. Origami are indicated in gray, the ribbon in dark green, and places where the ribbon folds on itself to give a double-width ribbon are in light green. Contours for DNA structures are subjective, it is difficul to tell in these images where the origami ends and the ribbon begins. SWNTs that apparently run under origami or ribbons have had their color deemphasized. For the bottom cross-junction, the position of the blue and red nanotubes (over or underneath the origami), as derived from the ribbon orientation and as suggested by which tube has the greater height contrast are in conflic (see S4). We have interpreted the image as though the ribbon-orientation tells the correct position, but this ribbon is so distorted that perhaps it has been "bent up" in a way that makes its apparent handedness incorrect.

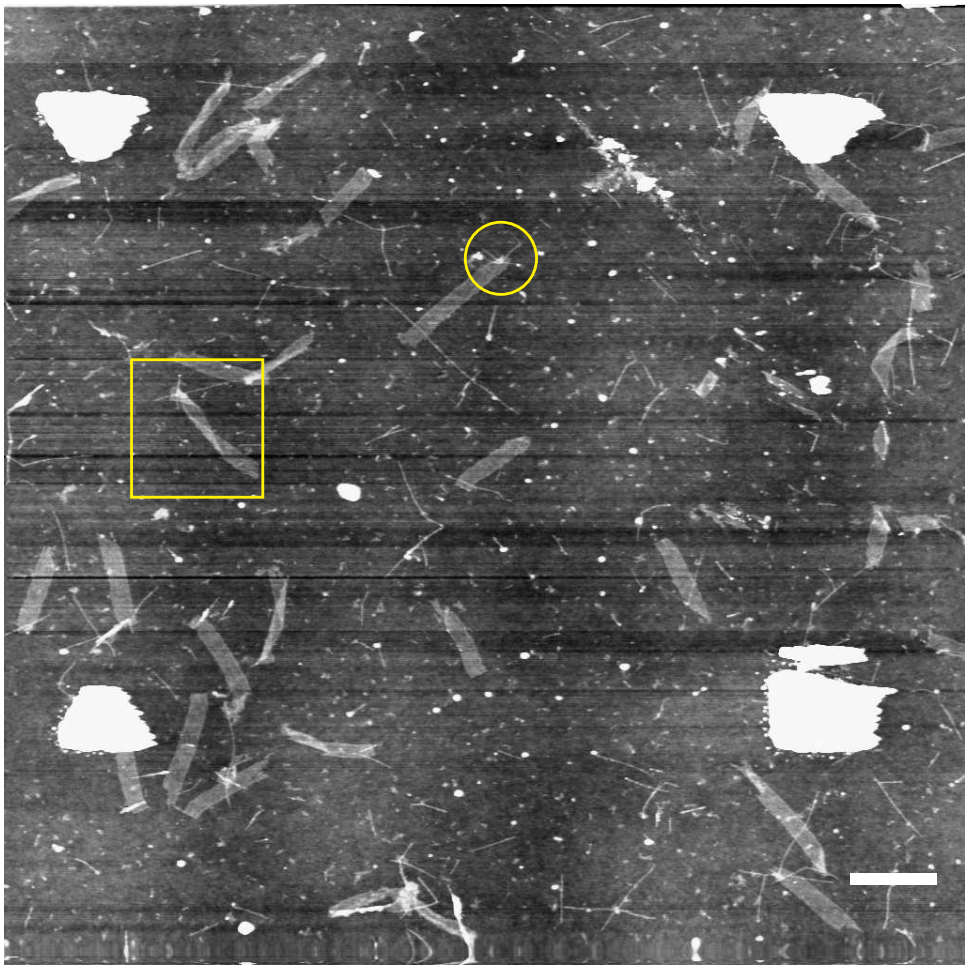

Figure S7: A typical wide-fiel view of cross-junctions on silicon. Two cross-junctions are outlined in yellow. In this particular wide-fiel view roughly 35 distinct DNA structures can be identified 17 have identifiabl origami and ribbon domains. Of these 12 have one or more SWNTs associated with the origami, and of these two have geometry judged to form a cross-junction. The boxed area contains the cross-junction shown at the top of Supplementary Fig. S6. The yield of DNA-templated cross-junctions is not greater, per unit area, than the number of crosses created by randomly associating SWNTs (perhaps a few here). Our measurement of the alignment of SWNTs to the lines of hooks on the origami (Fig. 2), as well as the relative sparsity of individual SWNT/SWNT crosses on ribbons in this image, suggest that the individual SWNT/SWNT crosses associated with the origami in this image are the result of specifi binding rather than random association. Scale bar 500 nm. $\sim$500 nm white features are gold alignment markers.

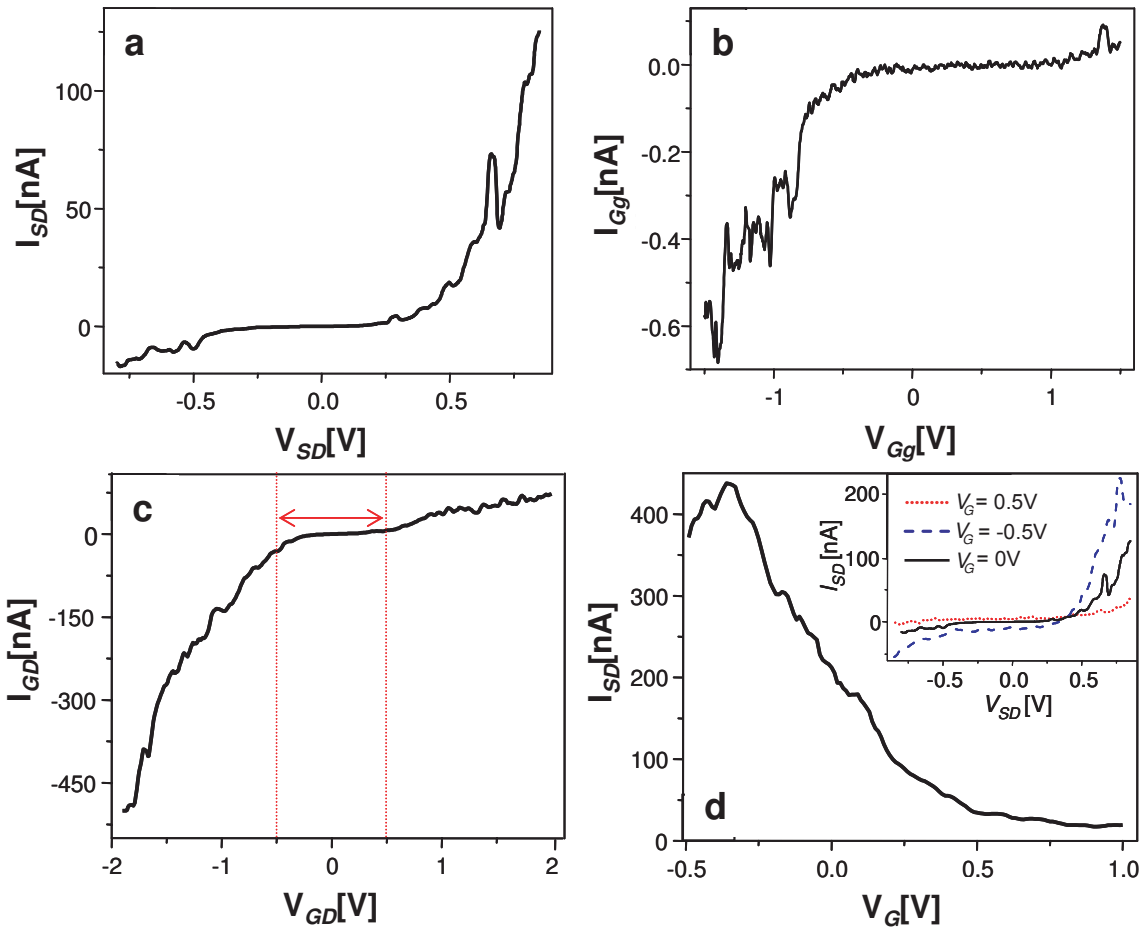

Figure S8: Electrical characterization of the self-assembled SWNT cross-junction in shown Fig. 3. For this particular device, the back-gate was not functioning. **(a)** Electrical measurement for the blue SWNT (source electrode S and drain electrode D) showing a nonlinear behavior suggestive of a p-type semiconductor. **(b)** Electrical measurement for the red SWNT (across gate electrode G and auxillary electrode g) showing high resistance. Lack of a back-gate meant that it was not possible to identity the red SWNT definit vely as a metallic or semiconducting. The apparent bad contact g may be responsible for its nonlinear behavior. **(c)** The inter-tube conductance as measured between electrode G and D. The red arrow marks the insulating region where there is little current leakage between the SWNTs. **(d)** Source-drain current (electrodes S and D) versus SWNT gate voltage (electrode G) for source-drain bias of 0.85 V. Gating of the blue SWNT confi ms it as a p-type semiconductor. The inset shows the source-drain I-V for different SWNT gate biases.

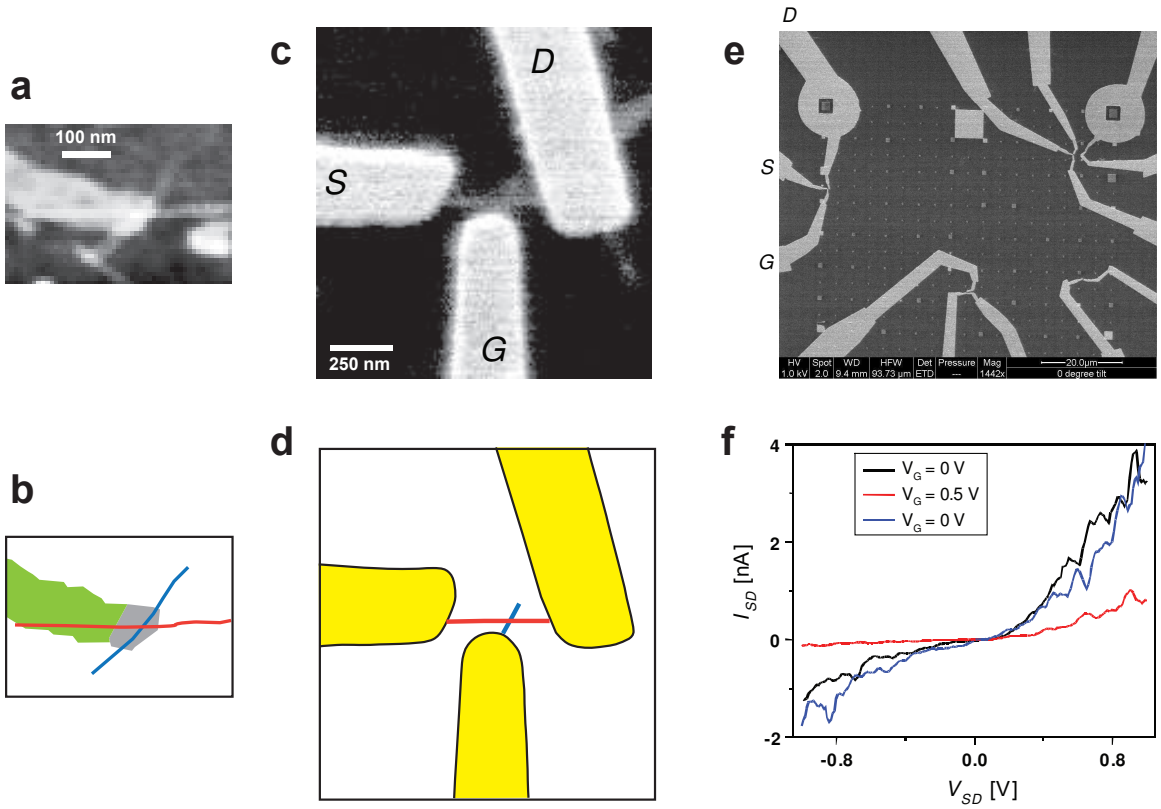

Figure S9: Electrical measurement of a second SWNT cross-junction exhibiting FET-type behavior, although it was only short-lived. **(a)** Dry mode AFM of the SWNT cross-junction on silicon before deposition of electrodes. **(b)** Interpretation of (a) showing red and blue SWNT as well as origami (gray) and ribbon (green). Orientation of the ribbon is uncertain and other cues are not present so it is impossible to tell which SWNT is on top. **(c)** Scanning electron micrograph (SEM) of the device after Pd/Au electrode deposition. **(d)** Interpretation of (c) indicating red and blue SWNTs. The DNA template is not clearly visible and may not be present after electrode fabrication. **e** SEM of large fiel showing electrodes short-lived device, alignment marks, and a variety of contacts to other devices. **(f)** Electrical measurement of gate-dependent switching of a resistive red SWNT, where the blue SWNT is used as the gate. A constant back gate voltage of 10 V is used for this measurement. Observed switching behavior was limited to just these few sweeps.

Chapter 3

DNA-Linker Enforced Surface Assembly of Ultra Dense Parallel Single Walled Carbon Nanotube Arrays

Portions of this chapter will appear in an upcoming paper with Hareem T. Maune, Robert D. Barish, Marc Bockrath and William A. Goddard III

3.1 Abstract

The printing of nanostructured arrays using nanomaterial inks is a challenging and technologically significant problem whose difficulties are accentuated by the geometric anisotropy of materials such as single walled carbon nanotubes (SWNT). We have discovered that multi-domain DNA linkers, which interact asymmetrically and cooperatively with different SWNTs, can disperse SWNTs in aqueous solution but condense them into cohesive parallel arrays on charged surfaces. The arrays have uniform and selectable inter-nanotube spacing from ~20 nm down to < 3 nm, can serve as scaffolds for further nanoscale construction, and are amenable to adhesive layer mediated transfer onto other substrates, thus creating opportunities for production of macromolecular scale device arrays, metamaterials, and electronic interfaces. Our results suggest that DNA Linker Enforced Surface Assembly may be a promising new strategy for low cost printing of diverse nanomaterial arrays.

3.2 Introduction

The self-assembly of solution dispersed single walled carbon nanotubes (SWNT)[1-3] and other geometrically anisotropic colloidal nanomaterials[4,5] into ordered arrays[6,7] requires alignment and orientation of irregularly shaped nanoscale objects along multiple axes to achieve particular desired arrangements. Satisfactory general solutions could enable scalable and economical continuous manufacturing processes that use liquid phase handling[3,8,9] to take bulk synthesized nanomaterials through multiple stages of chemical modification[10] and purification[11,12] before incorporation into real products as high performance nanostructured elements[7,9,13].

An important example of anisotropic nanoassembly is the arrangement of nanoscale wires into monolayer parallel arrays[7], which can maximize packing density without compromising each wire's electrical isolation and accessibility, thus enabling defect tolerant nanofabrics with transformative logic[14], memory[15], communications and sensor[7,9,14] applications. Existing top down methods can create parallel arrays from solution dispersed nanowires or SWNTs by applying alignment forces during deposition[16] or film formation[17], or by creating chemically patterned deposition substrates[18,19], but array densities greater than 30 μm^{-1} (vs ~1000 μm^{-1} maximum possible density for SWNTs) have not been achieved, and control over wire spacing at sub 100 nm scales have proven elusive. Alternatively, we have attached SWNTs to self-assembled DNA templates that can have sub 10 nm feature resolution[20], but this increases complexity and cost; the ordered structure cannot be larger than the limited size of the DNA nanostructure; and the chemical and geometric details of wire-template attachment introduces 10 nm scale uncertainties in wire spacing. Thus, both top down and bottom up methods have notable shortcomings.

3.3 Process Overview

We have discovered a new process, DNA linker enforced surface assembly (LESA), that combines top down and bottom up forces to assemble ultradense parallel SWNT arrays. In the LESA process, pristine SWNTs are gently sonicated in an aqueous salt solution with multi-domain DNA linkers (Figure 1a) that cooperatively disperse each nanotube via non-covalent wrapping of single stranded DNA[3,21] around the nanotube sidewall. The resulting colloid (Figure 1b) can remain stable for weeks under ambient

conditions, but the DNA-SWNTs will deposit onto charged substrates in the presence of divalent counterions, which form salt bridges[22] between nanotube anchored DNA linkers and surface charge groups. When monovalent counterions are then introduced to the deposition droplet, they disrupt the salt bridge interactions[22] sufficiently to allow the DNA-SWNTs to diffuse in 2D along the deposition surface (Figure 1c). Under surface confinement, weak sticky end interactions between DNA linkers on one nanotube and open patches of sidewall on a nearby nanotube can cooperatively induce the two SWNTs to stick together in parallel alignment. The double stranded domains of the DNA linkers then sit between the adjacent nanotubes to keep them at a fixed distance. Multiple such collision events create parallel arrays with uniform pitch (Figure 1d).

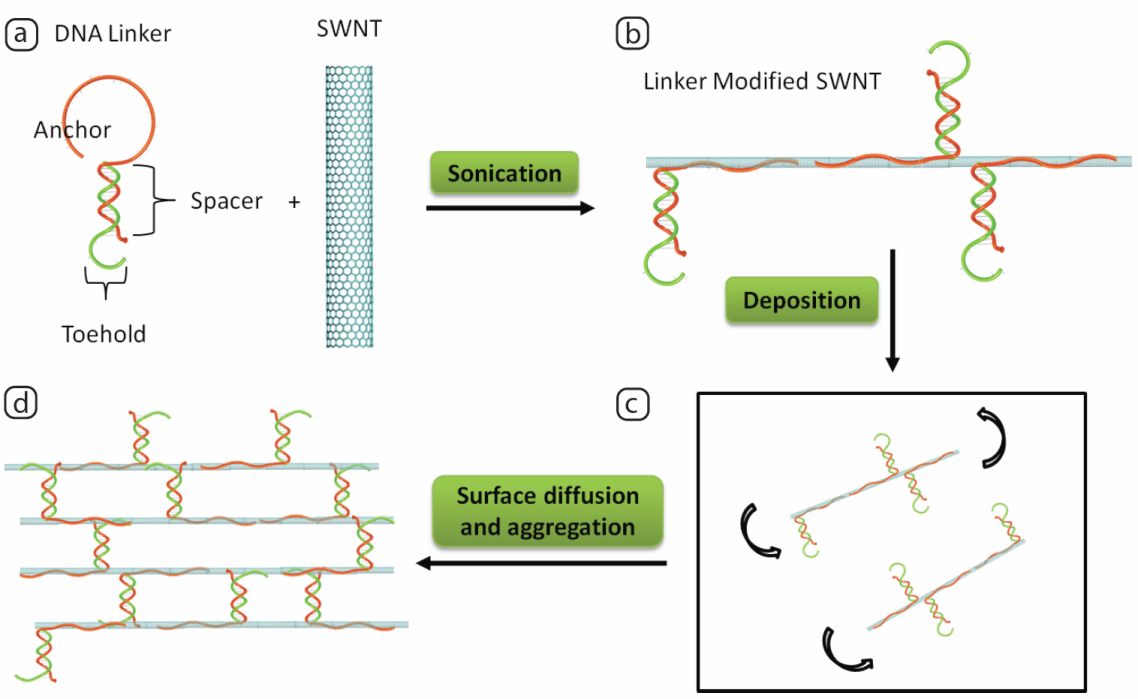

Figure 1 depicts DNA linker-spacers (a), DNA linker-spacer modified SWNTs (b), the surface diffusion assembly process (c) and the structure of the assembled arrays (d).

3.4 Surface Assembly

We first discovered the self-assembly process when we examined SWNTs dispersed using DNA oligonucleotide linkers possessing both single stranded and double stranded domains (fig 1a). Deposition of nanotubes bearing 20 base pair DNA duplexes on Muscovite mica at near monolayer surface coverage under 1x TAE Mg buffer (10 mM Tris Acetate, 1 mM EDTA, 12.5 mM Magnesium Acetate in water) resulted in formation of a large number of dimers and trimers of parallel SWNTs . The inter-nanotube separation appeared to be uniform (~ 7 nm to 9 nm from center to center). When the process was repeated at lower surface concentration of SWNTs or in the presence of 1 mM Ni Acetate (known to inhibit DNA duplex mobility on the mica surface[22]), there were far fewer assembled nanotubes. Since we have observed that DNA dispersed SWNTs under 1x TAE Mg buffer can move on the mica surface as they are imaged by tapping mode AFM, we hypothesized that the dimers and trimers might be forming via association of neighboring SWNTs on the deposition substrate.

To test the surface assembly hypothesis, we experimented with a different procedure that encouraged surface diffusion. Past studies[4] and our experiences have shown that DNA nanostructures adhering to mica under Mg^{2+} solutions can exhibit substantial surface diffusion in the presence of a high concentration of Na^{+}, which disrupts mica-Mg^{2+}-DNA salt bridges. To utilize this effect, we first deposited the DNA-SWNTs using 1xTAE Mg buffer, and then we replaced the solution covering the substrate with phosphate buffered NaCl at 0.75 M to 2 M concentrations. Tapping mode AFM images of deposited SWNTs under these conditions revealed substantial surface movement, while larger multi-nanotube assemblies appeared to have substantially lower

surface mobility than individual SWNTs (figure 2). When mica substrates with SWNTs incubated under NaCl were washed in 1x TAE Mg buffer and imaged with the addition of 1 mM Ni Acetate (known to inhibit DNA surface movement), we found that nearly all nanotubes had assembled into structures composed of two or more parallel SWNTs (figure 3). This occurred regardless of nanotube concentration on the mica surface or the presence or absence of perturbation by tapping mode AFM. Interestingly, varying the NaCl concentration and the surface density of deposited SWNTs seemed to have little effect on the width of the SWNT arrays (2 to 6 SWNTs on mica). We suspect that the non-linear drop in surface mobility observed for multi-nanotube arrays may be a self-limiting mechanism for the array size. Taken together, these observations strongly suggest that SWNTs assemble due to surface diffusion.

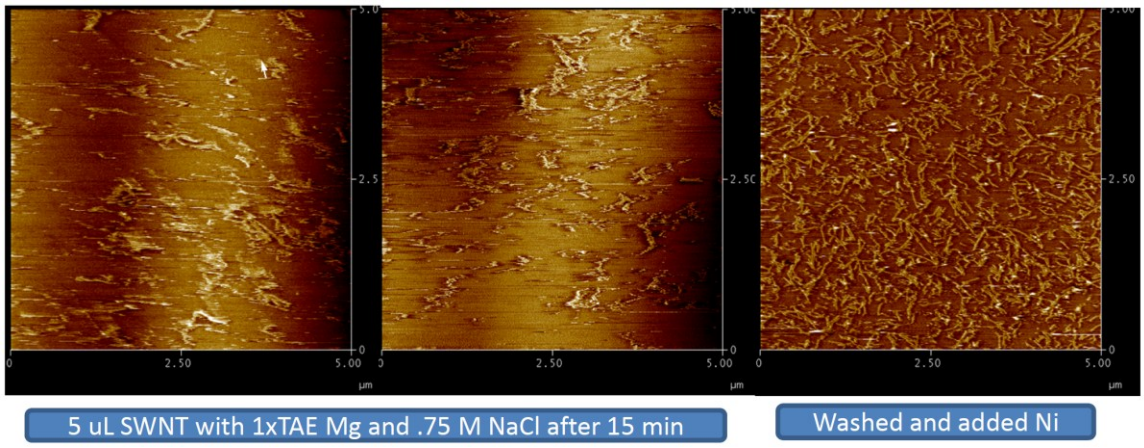

Figure 2 SWNTs were deposited on a mica surface and imaged under 1x TAE Mg with 0.75 M NaCl. Under tapping mode AFM, individual SWNTs cannot be imaged. The visible surface features appear to be clusters of aggregated nanotubes. After washing and buffer exchange to 1xTAE mg with ~1 mM Ni Acetate, numerous assembled carbon nanotube arrays can be seen.

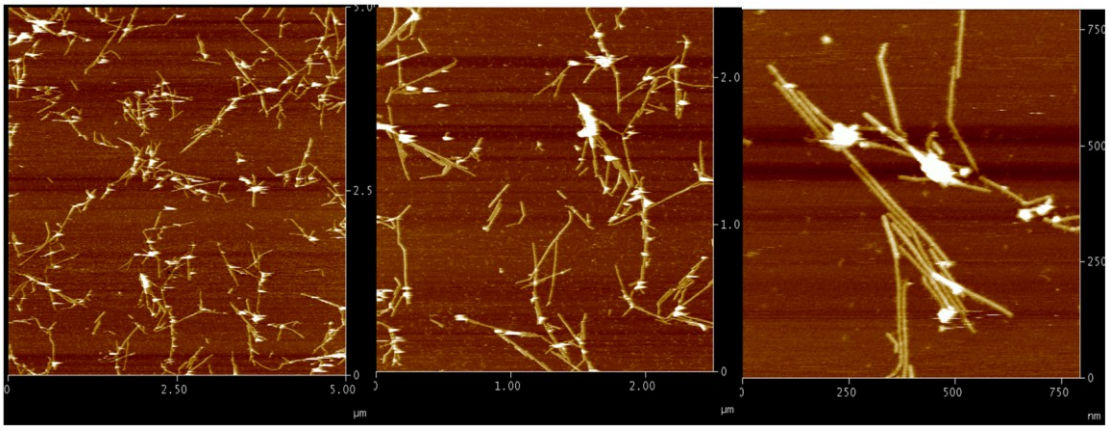

Figure 3 SWNT arrays assembled via surface assembly. For this experiment, the original SWNT solution was diluted 10x using 1xTAE Mg. 5 uL of the diluted solution was placed on a ~1 cm^2 piece of freshly cleave Muscovite mica, followed by 40 uL of 1xTAE Mg buffer. The solution was allowed to sit for 5 min, then the majority of the incubation solution was carefully removed using a 100 uL pipette. 40 uL of 0.75 M NaCl + 0.01 M Na2HPO4 solution was added. This was incubated at room temperature for ~2 hours. 50 uL of 1xTAE Mg was then added to the standing droplet on the mica surface, then 50 uL of solution was removed using a pipette. This was repeated 5 times. Finally, 7.5 uL of 10 mM Ni Acetate solution was added.

In addition to Muscovite mica, we also experimented with array assembly on substrate supported Dipalmitoylphosphatidylcholine (DPPC) lipid bilayers[23]. These bilayers can form on a variety of substrates, are compatible with lithographic patterning, and are frequently used to model biological membranes. At room temperature, DPPC bilayers are in the solid phase (T_m = 41˚C), with a smooth surface composed of densely

packed polar headgroups that allow counterion mediated surface diffusion of DNA modified SWNTs. The adhesion of DNA-SWNTs to the bilayer surface seems very sensitive to NaCl concentration. In the presence of 1xTAE Mg, all SWNTs desorbed from the surface when the solution concentration of NaCl exceeded 0.45 M. This suggests that even relatively large SWNT arrays may have some degree of surface mobility on DPPC at ~ 0.45M NaCl concentrations. This makes it easier to control array diffusion and assemble wider arrays, and we were able to produce parallel SWNT arrays up to 11 nanotubes wide by incubating SWNTs under 1xTAE Mg + 0.35 M NaCl buffer at room temperature (figure 4).

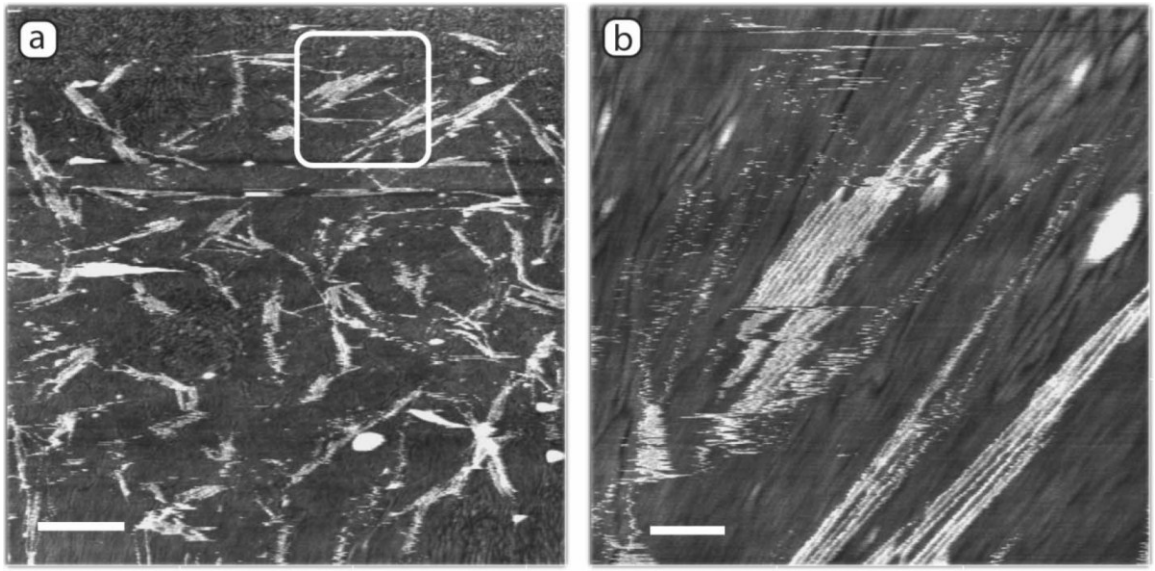

Figure 4 SWNT arrays formed in DPPC bilayer using 20 bp spacers with 9 base toehold. The boxed area in (a) is magnified in (b), showing an array with 11 parallel SWNTs. Scale bar are 500 nm in (a) and 200 nm in (b). (b) shows considerable distortion due to a problem with the AFM fluid cell.

3.5 Contact Printing

Since DNA modified SWNTs adhere to the negatively charged mica and polar DPPC surfaces via relatively weak Mg^{2+} mediated electrostatic interactions, we reasoned that a surface with densely packed positive charges might adhere more strongly to DNA's phosphate backbone groups and out-compete mica and DPPC for retention of assembled arrays. Thus, we clamped (figure 5) mica and DPPC substrates carrying assembled SWNT arrays onto *γ-Amino Propyl Silane* functionalized glass slides (Corning Life Sciences), which had a high surface density of positively charged primary amine groups. To facilitate the transfer, we first added NaCl to the assembly substrates to weaken binding of DNA-SWNTs with the mica surface. After ~2.5 hours, the clamped surfaces were carefully peeled apart. AFM scans showed that a large number of SWNT arrays transferred onto the glass surface and maintained their parallel structure and uniform pitch of ~8.3 nm. While stamping from the DPPC surface resulted in transfer of some DPPC patches along with the nanotubes, transfer from the mica was relatively clean (figure 6). This demonstrates a simple method for transferring assembled arrays onto silica based substrates suitable for lithographic device fabrication.

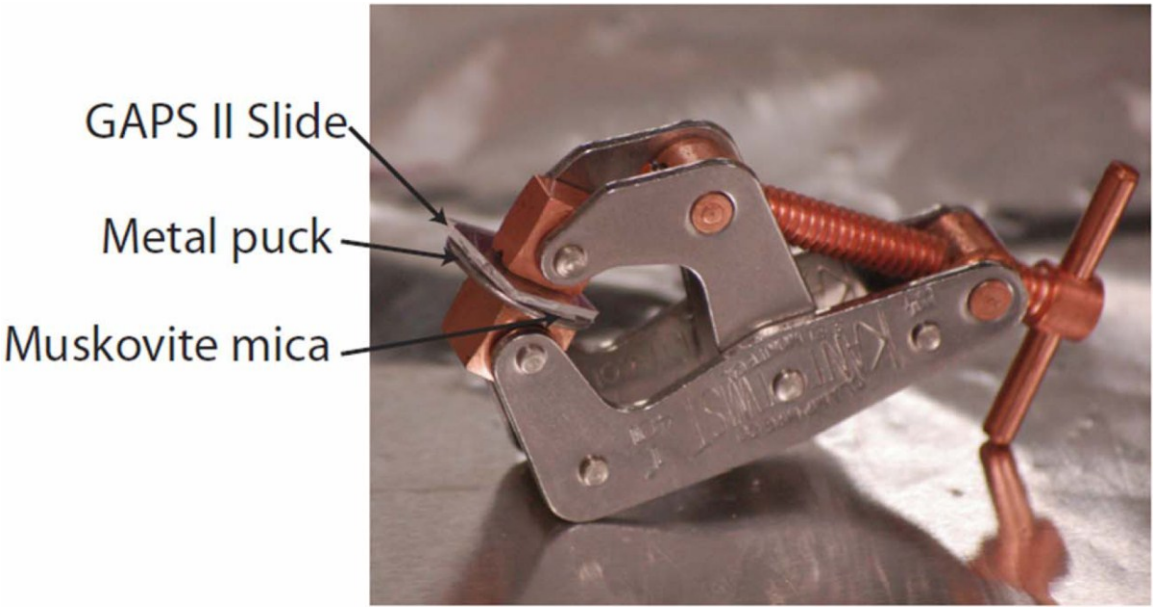

Figure 5 A mica puck carrying assembled SWNT arrays is clamped to a GAPS II (Corning Biosciences) microarray slide. The microarray slide is cleaved, rinsed using MilliQ water and then blown dry using nitrogen. It is then clamped with to the mica puck, which is glued onto a 15 mm metal specimen disk from (Ted Pella, Redding, CA). The clamp is screwed finger tight. The setup is then left for 2 hours at room temperature.

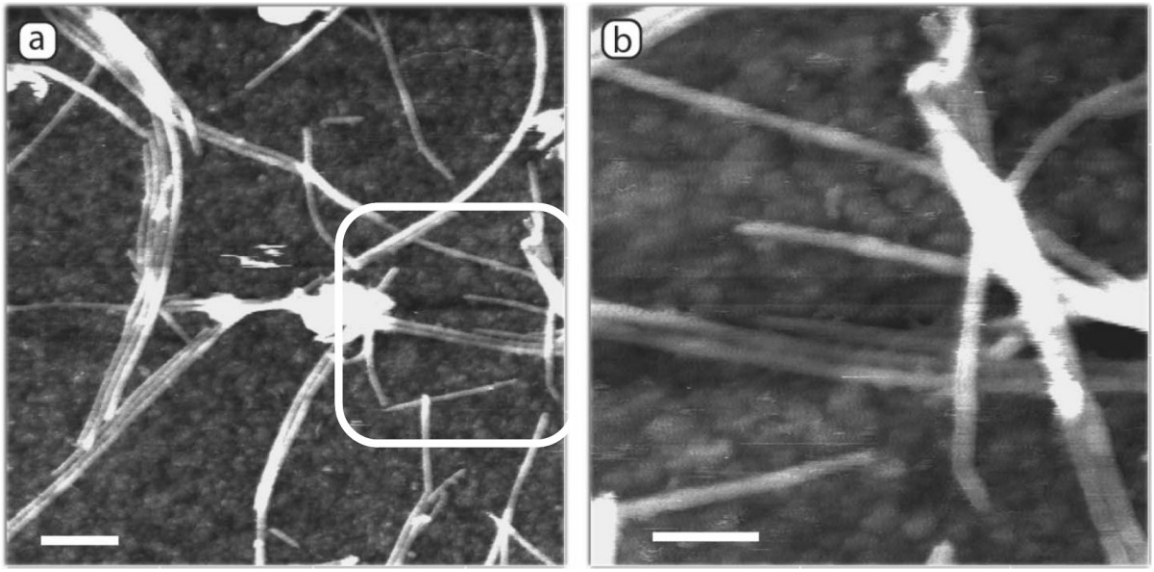

Figure 6 SWNT arrays formed on mica are stamped onto GAPS II microarray slides. (b) is a close up of the boxed area in (a). Scale bars are 100 nm in (a) and 50 nm in (b).

3.7 Array Structure

Figure 7 shows a high-resolution AFM scan of a SWNT dimer assembled using DNA linkers that possessed 20 bp spacer domains. This scan revealed a ladder like structure with dense "rungs" connecting adjacent parallel SWNTs. From our previous work[20] we knew that the 30 nucleotide (nt) long poly-Thymine dispersal domains of our linkers likely adsorbed strongly onto the SWNT surface. We also knew that our duplex spacer and short toehold domains (Fig 1a) likely remained free from the nanotube surface (Fig 1b). Of the two, the duplex is the only one large enough (6.8 nm) to appear as the ladder rungs in figure 7. Thus, we suspected that the DNA duplexes were situated between the SWNTs as rigid spacers while the toeholds adsorbed weakly onto accessible sidewall surfaces on the adjacent nanotube. Together, the rigid separators and sticky ends of numerous DNA linkers along each DNA-SWNT can cooperatively induce the

assembly and alignment of diffusing SWNTs and keep them at a uniform inter-nanotube separation. If true, then the array pitch should closely correlate with the length of the DNA duplexes.

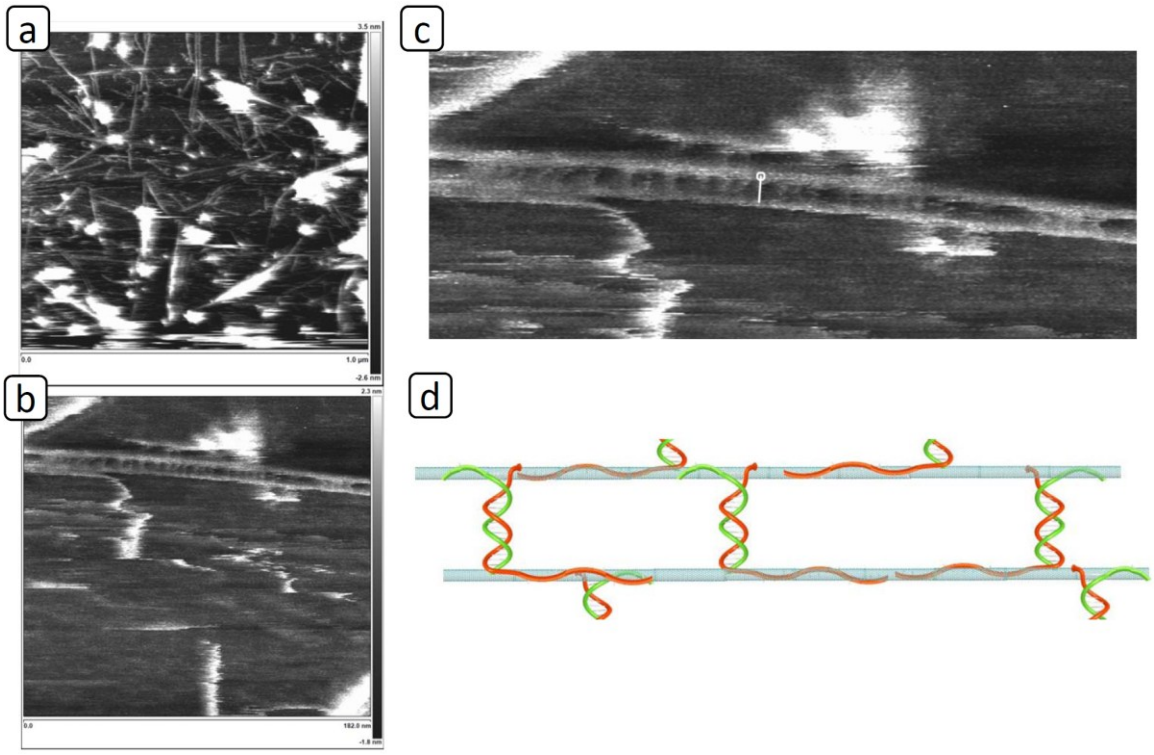

Figure 7 Tapping mode AFM images (topography) of SWNT arrays. (a) A 1 um by 1 um scan of SWNT dimers and trimers formed upon deposition of SWNTs under 1xTAE Mg buffer. (b) A 182 nm by 182 nm closeup of SWNT dimer. (c) Zoomed in view of the dimer in (b). The measurement mark shows a center to center distance of 7.3 nm between the two nanotubes. (d) Proposed structure of the SWNT "ladder".

To test the above hypothesis, we created DNA linkers with 7 bp (2.38 nm), 20 bp (6.8 nm) and 60 bp (20.4 nm) long duplex domains and used them to assemble SWNT arrays (figure 8) (the linker with the 7 bp spacer was formed from a single hairpin DNA due to energetic stability considerations; see methods for detailed explanation).

Remarkably, this resulted in the formation of arrays with ~2.9 nm (figure 8 a, d, h, i), ~8.5 nm (figure 8 b, e), and ~ 22 nm pitch (figure 8 c, f), as measured by AFM. To our knowledge, the ~2.9 nm arrays represent the highest density packing of parallel SWNTs achieved to date (~345 SWNTs μm^{-1}). Although the limitations of our AFM prevented consistent resolution of 7 bp and 20 bp spacers, the 60 bp spacers were clearly imaged (figure 2e). Most spacers between adjacent SWNTs spanned the gap from one nanotube to the next, thus giving strong evidence for the hypothetical structure depicted in Figure 1d.

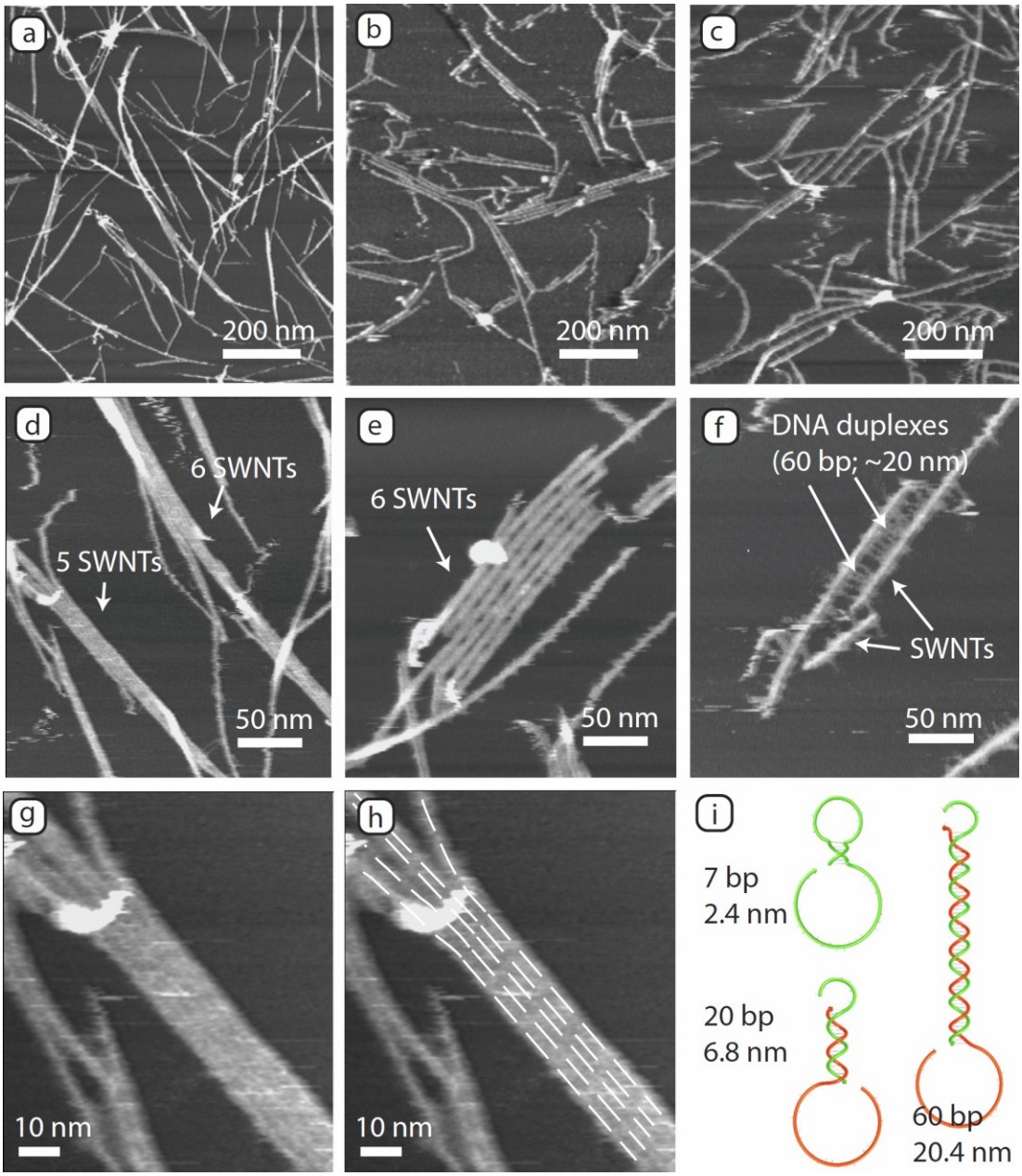

Figure 8 Tapping mode AFM showing topography of SWNT arrays on mica under fluid. **a, d, g,** and **h** show arrays formed with 7 bp DNA spacers. **g** and **h** depict the 5 SWNT array from **d**, with the dashed lines in **h** representing the approximate positions of the SWNTs. The measured array pitch was determined to be less than 3 nm. SWNT arrays with 20 bp (**b**, and **e**) and 60 bp spacers (**c**, and **f**) have array pitch of ~8.5 nm and ~22

nm, respectively. **i** depicts the structure of DNA linkers with 7bp, 20 bp and 60 bp. Notice that the linker with the 7 bp spacer is a hairpin while the larger linkers are constructed from 2 strands.

Interestingly, most of the 60 bp spacers appear to be oriented nearly perpendicularly to the axis of their nanotubes. To better understand the interaction of our DNA linkers with the SWNT sidewall, we assembled arrays using a series of linkers possessing 30 nt anchor, 20 bp spacer and 0, 5, 7, 9, or 11 nt toehold domains. We also attempted to assemble arrays using SWNTs dispersed with single stranded DNA. As expected, the single stranded DNA failed to induce any array assembly. Meanwhile, toehold lengths of 5 to 11 nt produced similar looking SWNT arrays, with the main difference being that 11 nt toeholds resulted in the formation of macroscopic SWNT precipitates in solution after a short period of time. Most surprisingly, however, SWNTs also underwent efficient assembly into parallel arrays when no toehold (0 nt) was used. In this case, three types of sticky end interactions may have contributed to SWNT assembly. First, we did not purify the synthesized oligonucleotides. Thus, linkers composed of truncated DNA strands would have been present in solution, and some of these may have dangling single stranded DNA on the end of the spacer domain. Secondly, the terminal A-T base-pair on the duplex spacer is unstable at room temperature. Thus, one or more base pairs may be able to dissociate and adsorbed onto the sidewall of the SWNT. Lastly, DNA duplex blunt ends should have significant favorable dispersive interactions with the SWNT sidewall. All of the above may contribute to array assembly via the cooperation of multiple linker sticky ends, and the second and third mechanisms may also be partially responsible for the transverse orientation of spacer domains situated between adjacent SWNTs.

With the structures of the arrays known, an unresolved question is why DNA-SWNTs can remain dispersed in solution but assemble after deposition. We do not

currently understand the detailed causes or whether the effect is thermodynamic or kinetic. However, as our experience with the 11 nt toehold linkers demonstrates, a likely significant factor is the weakness of individual toehold-nanotube interactions and the resulting requirement for cooperation between linkers to induce nanotube assembly. On the deposition substrate, the confinement of DNA linkers to the plane of the substrate may then favor the cooperative toehold-sidewall sticky interactions necessary for assembly.

3.8 Attachment of Proteins

DNA spacers in the assembled arrays offer convenient scaffolds for arrangement of heterogeneous molecular, macromolecular, and nanoscale components between parallel SWNTs. We modified the 60 bp spacer by changing one of its internal dTs to a biotin linked dT. The position of this modification (35^{th} base-pair from the base of the toehold) puts it ~12 nm from the toehold side and ~8.5 nm from the anchor. SWNTs with the biotinylated linker assembled on mica without issue. When Streptavidin was added to assembled arrays (~18 nM concentration), they attached to DNA spacers at the designated positions between adjacent SWNTs (figure 9).

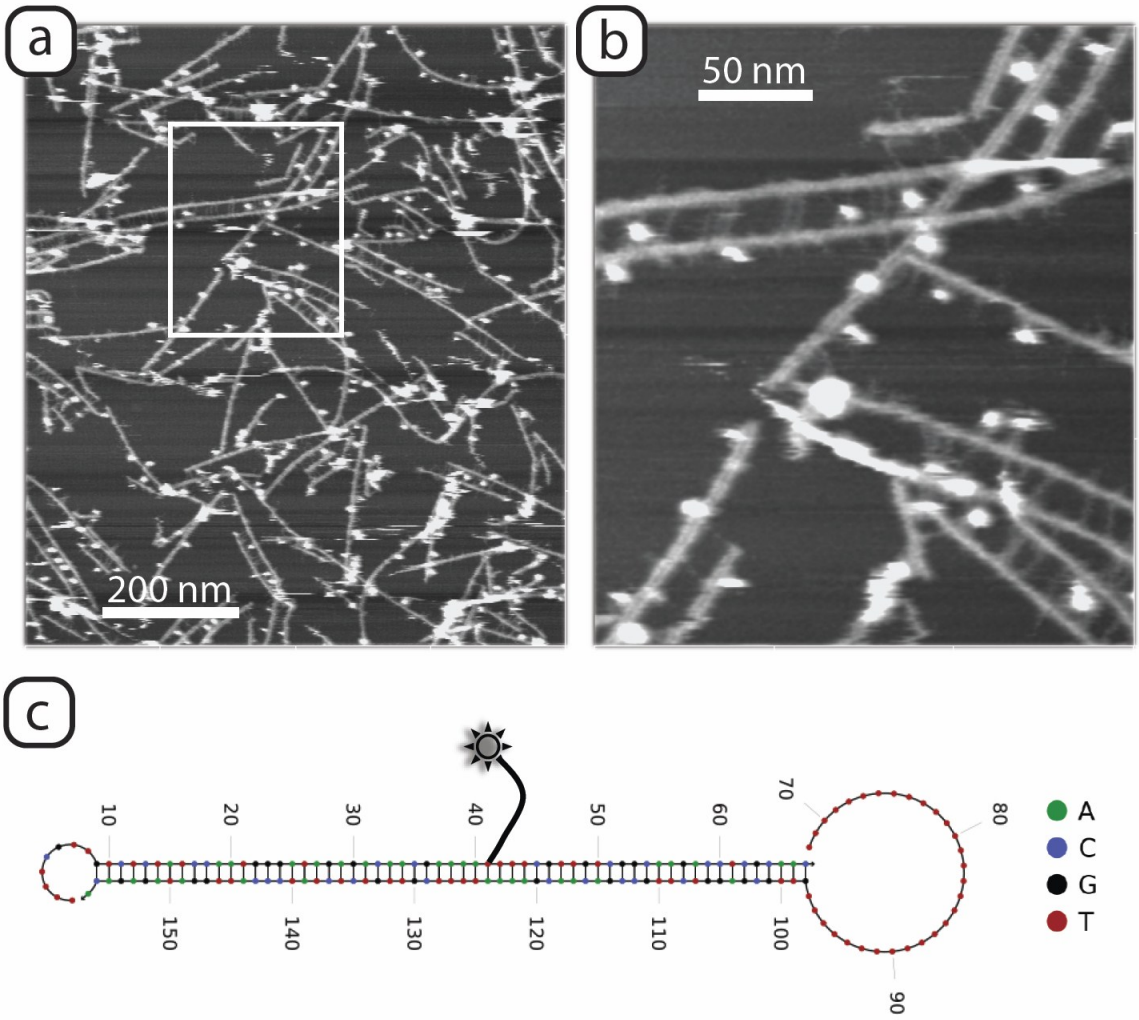

Figure 9 Tapping mode AFM of SWNT arrays with biotin modified 60 bp spacers and attached Streptavidin proteins on mica under salt buffer solution. The boxed area in **A** is magnified in **B**. Streptavidin proteins (bright spots) are seen on DNA duplexes bridging adjacent SWNTs. Note that some Streptavidin proteins are attached to DNA duplexes that are pointing away from the adjacent SWNT. **C** The position of the biotin linker on the modified linker.

3.9 Implications for Colloidal Nanoassembly

Linker enforced surface assembly opens a new route for using colloidal nanomaterials in manufacturing and provides a simple method for making carbon nanotube arrays with diverse applications. Compared to other methods [4,6,24,25], LESA elevates surface diffusion to the role of a central actor in self-assembly. This has two advantages. First, as is the case with SWNTs (a flexible one dimensional rod with extreme length to width ratio), surface confinement can limit the orientation and conformational freedom of anisotropic nanomaterials and their conjugated linkers to allow rapid assembly of arrays not easily obtainable in three dimensions. Second, surface diffusion can be influenced by top-down alignment forces[7,9,16] and meso and microscale surface patterning[18,19,26], which may be able to determine the alignment, placement and overall shape of assembled arrays. This would allow one to use hybrid assembly techniques that leave nanoscale order to self-assembly and microscale integration to top down processes for economical production of complex devices.

A key enabler of the above strategy is the use of structured DNA linkers. Although single stranded DNA has long been used in colloidal nanoassembly[27,28], only recently have we[20] and others[8] begun utilizing rational design of secondary and tertiary structure to create multifunctional chemical interfaces that can achieve dynamic control of assembly kinetics and configurations. The present results demonstrate that structured DNA linkers can (a) respond to surface confinement by qualitatively changing the mutual interactions between colloidal nanomaterials, (b) allow controlled surface diffusion on charged substrates, (c) adopt well defined conformations in assembled arrays, (d) act as integral nanoscaffolds for further nanoscale construction, (e) and mediate contact printing

of assembled arrays. Thus the extra complexity of structured linkers can actually enable greater simplicity and versatility. We believe that it should be possible, in general, to develop LESA like assembly processes for other anisotropic nanomaterials by designing conformational mismatches and entropic barriers that can be alleviated by surface confinement.

3.10 SWNT Array Applications

Besides the general implications for colloidal nanoassembly, the LESA method improves control over the spacing of parallel SWNTs by an order of magnitude over previous techniques[7], resulting in modulation of macromolecular scale distances in nanometer scale increments. As high quality, uniformly metallic or semiconducting SWNTs[11,12] are already available from commercial sources, these can be directly used by our process to create extremely dense, electronically pure SWNT arrays that may substantially improve the performance of SWNT based nanoelectronics[29], or allow the implementation of nanofabric type architectures[15,30,31] at densities on the order of 1 device every 10 nm^{-2}. The use of SWNT arrays to create electronically tunable metamaterials should also be considered, as theoretical calculations have shown[32], for example, that the application of superlattice electrical potentials with 10 nm scale periodicities to graphene could lead to supercollimation of electrons propagating in graphene in the direction of the periodicity. Finally, the macromolecular scale is the operating scale of biological machinery. Recent developments[33-36] suggest an emerging convergence of nanoelectronics and single molecule biology. Carbon nanotubes, which have already been used as electrodes for individual DNA duplexes[34,37], individual

chromophores[38] and sidewall adsorbed proteins[39] and enzymes[40], may be ideal molecular electrodes. Our method now allows construction of arrays where the spacing between adjacent nanotubes can be adjusted to match the size of biomolecules, which can be scaffolded and oriented by structured DNA linkers, and electrically connected to SWNTs via noncovalent[39,41] or covalent means. This may enable bioelectronic interfaces (figure 10) that can sense biomolecules[7] or regulate biological activity [35]. For example, a dense array of SWNTs could be placed over a synthetic nanopore as an electronically connected nanofluidic grating (figure 11) for modulation of ion transport, control of array embedded biological nanochannels, or sequencing of translocating DNA oligonucleotides via measurement of transverse tunneling currents [42,43].

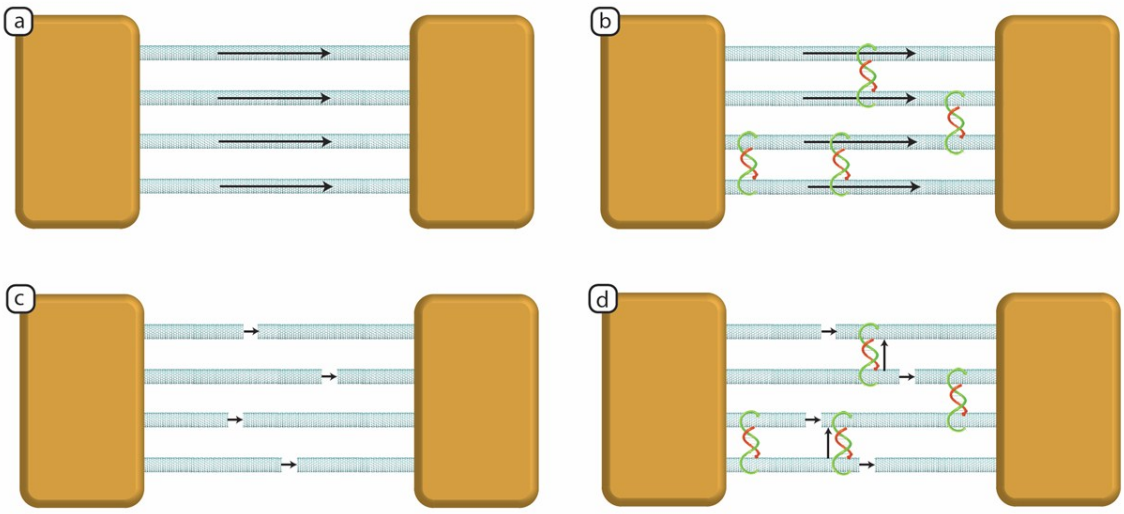

Figure 10 A Electrical current flow through an array of parallel SWNTs contacted by 2 electrodes. B In this configuration, when macromolecules are suspended between adjacent SWNTs, it's still not possible to measure tunneling current through the macromolecules. C an array of SWNTs are broken at random positions by passing a high current through them, creating a number of gaps that destroy the normal conduction pathways. D The new configuration always creates overlaps where it's possible for current to tunnel from left electrode to the right through suspended macromolecules. It's now possible to measure these currents if the currents through the molecular analytes are similar or larger in magnitude compared to the tunneling currents through the gaps in the nanotubes.

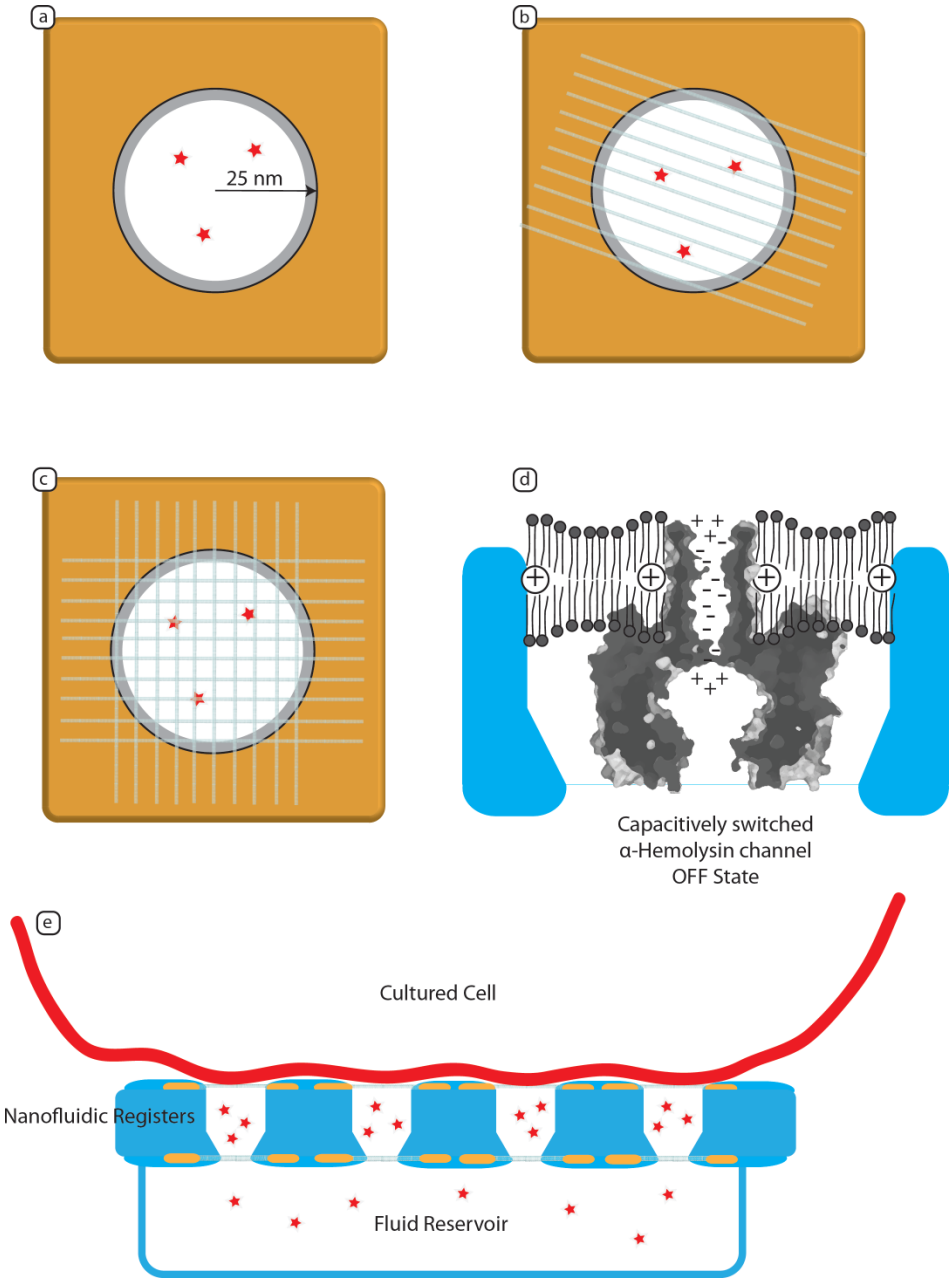

Figure 11 A 50 nm nanopore is unable to modulate the transit of proteins and other molecules (stars) through the pore since Debye length in physiological buffer is ~1 nm (shown by the gray area) B With a grating of randomly oriented parallel SWNTs, biological molecules must now pass between the spaces between adjacent SWNTs, which can be adjusted according to the size of the gated molecule. An electrical potential applied to the SWNTs using the electrode can now effectively modulate the transit of the

biomolecules. C It is also possible to create a mesh or more complicated multilayer structures by printing multiple layers of SWNT arrays. D SWNT embedded within or situated on top of a lipid bilayer can electronically modulate transport through biological nanochannels such as α-hemolysin. In this case SWNTs spaced ~3 nm apart may be able to capacitively modulate ion flow through the α-hemolysin. E An array of "nanofluidic registers". Each register accumulates a precise amount of chemical signals for algorithmic release to a cultured cell. It may eventually be possible to use these types of array interfaces to achieve spatially and temporally resolved *exchange* of chemical information with living systems.

3.11 Methods and Materials

Materials

CoMoCat single walled carbon nanotubes were purchased from Southwest Nanotechnologies (Norman, OK) in powder form and used as received. Alternatively P2 SWNTs can be purchased from Carbon Solutions (Riverside, CA)

Custom DNA was ordered from Integrated DNA Technologies (Coralville, Iowa), dissolved in MilliQ water and kept frozen at -20˚C. Sequences are listed in table 1.

Dipalmitoylphosphatidylcholine (DPPC) was obtained in powder form from Avanti Polar Lipids (Alabaster, Alabama).

GAPS II microarray slides were obtained from Corning Life Sciences (Lowell, Ma).

Formation of DNA linkers

DNA linker strands are added to ~33 μM concentration in 500 μL of 1xTAE Mg buffer (10 mM tris acetate, 1 mM EDTA, 12.5 mM Magnesium Acetate). When 2 strands are used for the linker, the toehold side strand is added at 10% excess to the anchor side.

The linker solution is then partitioned into 100 μL aliquots and annealed in a PCR thermal cycler (95˚C for 1 min, then cool to 20˚C at 1˚C per minute).

Dispersal of SWNTs

The annealed linkers are added to ~0.5 mg to 1 mg of SWNTs in a 1.6 mL PCR tube. This solution is then sonicated for ~60 min in a Branson 2510 bath sonicator until the SWNTs are dispersed. For this operation the water level in the sonicator can be reduced from the standard operating level to increase applied power.

Following sonication, the SWNT linker solution is centrifuged at 16000g at 4˚C for 90 min. The supernatant is recovered and the retenate is discarded.

The dispersed SWNT solution can remain stable at 4˚C for up to 1 month. 100 µL aliquots can be stored indefinitely at -80˚C.

Table 3.1: Sequences of DNA strands

Strand	**Sequence**	**Special instructions**
7 bp hairpin linker	5'-GCCGGGCTTTTTTTTTTTTTTTGCCCGGCTTTTTTTTTTT TTTTTTTTTTTTTTTTTT-3'	Standard Desalting
20 bp anchor side	5'-TTTTTTTTTTTTTTTTTTTTTTTTTTTTTGTTGCGAGGTCT TGCCGACA-3'	Standard Desalting
20 bp toehold side:		
0 base toehold	5'-TGTCGGCAAGACCTCGCAAC-3'	Standard Desalting
5 base toehold	5'-TTCGTTGTCGGCAAGACCTCGCAAC-3'	Standard Desalting
7 base toehold	5-TTTTCGTTGTCGGCAAGACCTCGCAAC-3	Standard Desalting
9 base toehold	5'-TTTTTTCGTTGTCGGCAAGACCTCGCAAC-3'	Standard Desalting
11 base toehold	5'-TTTTTTTTCGTTGTCGGCAAGACCTCGCAAC-3'	Standard Desalting
60 bp anchor side	5'-TTTTTTTTTTTTTTTTTTTTTTTTTTTTTGTTGCGAGGTCT TGCCGACAACGAAAATTTTCGTTGTCTCTATCCCATTGGATAG AGACA-3'	Ultramer, no purifiaction
60 bp toehold side; no biotin	5'-TTTTCGTTGTCTCTATCCAATGGGATAGAGACAACGAA AATTTTCGTTGTCGGCAAGACCTCGCAAC-3'	Ultramer, no purifiaction
60 bp toehold side; internal biotin	5'-TTTTCGTTGTCTCTATCCAATGGGATAGAGACAACGAAAA /iBiodT/TTTCGTTGTCGGCAAGACCTCGCAAC-3'	PAGE purified

Preparation on mica

2.5 to 20 µL of dispersed SWNTs were added to ~4 cm^2 pieces of Muskovite mica, then 1xTAE Mg is added to bring the drop to 20 µL. After 5 min at room

temperature, 80 μL of solution containing 1.5 M NaCl and 0.1 M Na_2HPO_4 is added to the existing droplet. (The exact concentration of NaCl does not seem to significantly affect the assembly process. 0.5M to >2M NaCl with either no buffer, or 1xTAE, or 0.01 M to 0.1 M Na_2HPO_4 will all work).

Incubation conditions can vary. Best results were achieved for 30 min incubations at 40˚C, but room temperature incubations from 15 min to 24 hours will also result in good assembly.

For stable imaging using fluid mode AFM, the buffer is first exchange to 1xTAE Mg by removing 50 μL from the droplet using a pipette, then adding 50 μL of 1xTAE Mg. This is repeated 5x. Finally, 50 μL of the droplet is removed (leaving 50 μL), and a 10 uL drop of 10 mM NiAcetate is then added.

Preparation on DPPC

DPPC was dissolved in 0.2 M NaCl and 0.01 M mono and di sodium phosphate buffer (~pH 7.5) at 25 mg/mL concentration and ~50 nm wide liposomes were formed via either extrusion or sonication using standard methods. The stock solution can be stored at 4˚C for 2 months. Immediately before formation of the bilayer, the stock solution is diluted to 2.5 mg/mL concentration in either 1xTAE mg buffer or in 2 mM $CaCl_2$, 0.2 M NaCl and 0.01 M mono and di sodium phosphate.

For the substrate, glass cover slips or silicon wafers with native oxide are cleaned and cleaved into ~4 cm^2 pieces. Immediately before deposition of lipids, the cover slips are treated to increase their hydrophilicity. (30 μL of spectroscopy grade ethanol is added to each cut piece, ignited with a butane lighter, and allowed to burn. This can be repeated one or two times as needed.)

50 to 100 µL of 2.5 mg/mL DPPC is then added to the piece, which is then sealed in an airtight chamber and incubated in a PCR thermal cycler for 30 min at 50˚C. The temperature is then lowered to room temperature at a rate of 1˚C every 10 seconds. The glass or silicon substrate is then washed with 1xTAE Mg + 0.35 M NaCl buffer without exposing the surface to air (a good method is to remove 50 µL from the droplet with a pipette, add 50 µL of the washing solution, and repeat 5 to 10 times). Finally, 50 µL of 1xTAE Mg + 0.35 M NaCl buffer is left on the substrate.

20 µL of dispersed SWNTs in 1xTAE Mg is added to the 50 µL droplet and the substrate carrying the SWNT solution is allowed to incubate at room temperature in a wet chamber for at least 2 hours. The substrate is then imaged under 1xTAE Mg + 0.35 M NaCl buffer.

Addition of Streptavidin

For Streptavidin binding, substrates with well forced SWNT arrays are washed and covered with 50 µL 1xTAE Mg. A 10 µL droplet of 200 nM Streptavidin in 1xTAE Mg is then added and the mixture is allowed to incubate at room temperature in a wet chamber for 1 hour.

Stamping

For stamping the SWNTs formed on mica are covered with 1.5 M NaCl, 0.1 M Na_2HPO_4 buffer and clamped tightly to a piece of GAPS II microarray slide from Corning Life Sciences for 2 hours.

For stamping the SWNTs formed on DPPC, well formed SWNTs were covered in 1xTAE Mg + 0.35 M NaCl buffer and clamped to GAPS II microarray slides in a similar fashion. (See figure 6).

AFM Imaging

Images were collected by a Veeco (Plainview, NY) Nanoscope III system equipped with a fluid cell and a J scanner. The AFM was operated in tapping mode using Veeco SNL silicon nitride soft contact mode AFM tips (2 nm nominal tip radius, smaller cantilevers used). Amplitude setpoint was typically ~0.4 V, drive amplitude ~50 to 200 mV, integral gain of 0.3 to 0.5, frequency ~10 kHz and scan rate is typically 2 to 6 Hz.

3.13 References

1 McEuen, P. L., Fuhrer, M. S. & Hongkun, P. Single-walled carbon nanotube electronics. *Nanotechnology, IEEE Transactions on* **1**, 78-85 (2002).

2 Avouris, P. & Chen, J. Nanotube electronics and optoelectronics. *Materials Today* **9**, 46-54, doi:Doi: 10.1016/s1369-7021(06)71653-4 (2006).

3 Zheng, M. *et al.* DNA-assisted dispersion and separation of carbon nanotubes. *Nat Mater* **2**, 338-342 (2003).

4 Jones, M. R. *et al.* DNA-nanoparticle superlattices formed from anisotropic building blocks. *Nat Mater* **9**, 913-917, doi:http://www.nature.com/nmat/journal/v9/n11/abs/nmat2870.html#supplementary-information (2010).

5 Glotzer, S. C. & Solomon, M. J. Anisotropy of building blocks and their assembly into complex structures. *Nat Mater* **6**, 557-562 (2007).

6 Nykypanchuk, D., Maye, M. M., van der Lelie, D. & Gang, O. DNA-guided crystallization of colloidal nanoparticles. *Nature* **451**, 549-552, doi:http://www.nature.com/nature/journal/v451/n7178/suppinfo/nature06560_S1.html (2008).

7 Cao, Q. & Rogers, J. A. Ultrathin Films of Single-Walled Carbon Nanotubes for Electronics and Sensors: A Review of Fundamental and Applied Aspects. *Advanced Materials* **21**, 29-53 (2009).

8 Leunissen, M. E. *et al.* Switchable self-protected attractions in DNA-functionalized colloids. *Nat Mater* **8**, 590-595,

doi:http://www.nature.com/nmat/journal/v8/n7/suppinfo/nmat2471_S1.html (2009).

9 Engel, M. *et al.* Thin Film Nanotube Transistors Based on Self-Assembled, Aligned, Semiconducting Carbon Nanotube Arrays. *ACS Nano* **2**, 2445-2452, doi:10.1021/nn800708w (2008).

10 Bahr, J. L. & Tour, J. M. Covalent chemistry of single-wall carbon nanotubes. *Journal of Materials Chemistry* **12**, 1952-1958 (2002).

11 Tu, X., Manohar, S., Jagota, A. & Zheng, M. DNA sequence motifs for structure-specific recognition and separation of carbon nanotubes. *Nature* **460**, 250-253, doi:http://www.nature.com/nature/journal/v460/n7252/suppinfo/nature08116_S1.html (2009).

12 Arnold, M. S., Green, A. A., Hulvat, J. F., Stupp, S. I. & Hersam, M. C. Sorting carbon nanotubes by electronic structure using density differentiation. *Nat Nano* **1**, 60-65, doi:http://www.nature.com/nnano/journal/v1/n1/suppinfo/nnano.2006.52_S1.html (2006).

13 Koleilat, G. I. *et al.* Efficient, Stable Infrared Photovoltaics Based on Solution-Cast Colloidal Quantum Dots. *ACS Nano* **2**, 833-840, doi:10.1021/nn800093v (2008).

14 Lu, W. & Lieber, C. M. Nanoelectronics from the bottom up. *Nat Mater* **6**, 841-850 (2007).

15 Green, J. E. *et al.* A 160-kilobit molecular electronic memory patterned at 1011 bits per square centimetre. *Nature* **445**, 414-417,

doi:http://www.nature.com/nature/journal/v445/n7126/suppinfo/nature05462_S1.html (2007).

16 Huang, Y., Duan, X., Wei, Q. & Lieber, C. M. Directed Assembly of One-Dimensional Nanostructures into Functional Networks. *Science* **291**, 630-633, doi:10.1126/science.291.5504.630 (2001).

17 Li, X. *et al.* Langmuir−Blodgett Assembly of Densely Aligned Single-Walled Carbon Nanotubes from Bulk Materials. *Journal of the American Chemical Society* **129**, 4890-4891, doi:10.1021/ja071114e (2007).

18 Wang, Y. *et al.* Controlling the shape, orientation, and linkage of carbon nanotube features with nano affinity templates. *Proceedings of the National Academy of Sciences of the United States of America* **103**, 2026-2031, doi:10.1073/pnas.0511022103 (2006).

19 LeeM *et al.* Linker-free directed assembly of high-performance integrated devices based on nanotubes and nanowires. *Nat Nano* **1**, 66-71, doi:http://www.nature.com/nnano/journal/v1/n1/suppinfo/nnano.2006.46_S1.html (2006).

20 Maune, H. T. *et al.* Self-assembly of carbon nanotubes into two-dimensional geometries using DNA origami templates. *Nat Nano* **5**, 61-66, doi:http://www.nature.com/nnano/journal/v5/n1/suppinfo/nnano.2009.311_S1.html (2010).

21 Zheng, M. *et al.* Structure-Based Carbon Nanotube Sorting by Sequence-Dependent DNA Assembly. *Science* **302**, 1545-1548, doi:10.1126/science.1091911 (2003).

22 Pastré, D. *et al.* Adsorption of DNA to Mica Mediated by Divalent Counterions: A Theoretical and Experimental Study. *Biophysical journal* **85**, 2507-2518 (2003).

23 Jung, S.-Y., Holden, M. A., Cremer, P. S. & Collier, C. P. Two-Component Membrane Lithography via Lipid Backfilling. *ChemPhysChem* **6**, 423-426 (2005).

24 Macfarlane, R. J. *et al.* Assembly and organization processes in DNA-directed colloidal crystallization. *Proceedings of the National Academy of Sciences* **106**, 10493-10498, doi:10.1073/pnas.0900630106 (2009).

25 Yang, S.-M., Kim, S.-H., Lim, J.-M. & Yi, G.-R. Synthesis and assembly of structured colloidal particles. *Journal of Materials Chemistry* **18**, 2177-2190 (2008).

26 Tsai, J., Sun, E., Gao, Y., Hone, J. C. & Kam, L. C. Non-Brownian Diffusion of Membrane Molecules in Nanopatterned Supported Lipid Bilayers. *Nano Letters* **8**, 425-430, doi:10.1021/nl072304q (2008).

27 Alivisatos, A. P. *et al.* Organization of 'nanocrystal molecules' using DNA. *Nature* **382**, 609-611 (1996).

28 Mirkin, C. A., Letsinger, R. L., Mucic, R. C. & Storhoff, J. J. A DNA-based method for rationally assembling nanoparticles into macroscopic materials. *Nature* **382**, 607-609 (1996).

29 Rutherglen, C., Jain, D. & Burke, P. Nanotube electronics for radiofrequency applications. *Nat Nano* **4**, 811-819 (2009).

30 Rueckes, T. *et al.* Carbon Nanotube-Based Nonvolatile Random Access Memory for Molecular Computing. *Science* **289**, 94-97, doi:10.1126/science.289.5476.94 (2000).

31 Copen Goldstein, S. & Budiu, M. in *Computer Architecture, 2001. Proceedings. 28th Annual International Symposium on.* 178-189.

32 Park, C.-H., Son, Y.-W., Yang, L., Cohen, M. L. & Louie, S. G. Electron Beam Supercollimation in Graphene Superlattices. *Nano Letters* **8**, 2920-2924, doi:10.1021/nl801752r (2008).

33 Hall, A. R. *et al.* Hybrid pore formation by directed insertion of [alpha]-haemolysin into solid-state nanopores. *Nat Nano* **5**, 874-877, doi:http://www.nature.com/nnano/journal/v5/n12/abs/nnano.2010.237.html#supplementary-information (2010).

34 Guo, X., Gorodetsky, A. A., Hone, J., Barton, J. K. & Nuckolls, C. Conductivity of a single DNA duplex bridging a carbon nanotube gap. *Nat Nano* **3**, 163-167, doi:http://www.nature.com/nnano/journal/v3/n3/suppinfo/nnano.2008.4_S1.html (2008).

35 Davis, J. J. *et al.* Molecular bioelectronics. *Journal of Materials Chemistry* **15**, 2160-2174 (2005).

36 Clarke, J. *et al.* Continuous base identification for single-molecule nanopore DNA sequencing. *Nat Nano* **4**, 265-270, doi:http://www.nature.com/nnano/journal/v4/n4/suppinfo/nnano.2009.12_S1.html (2009).

37 Roy, S. *et al.* Direct Electrical Measurements on Single-Molecule Genomic DNA Using Single-Walled Carbon Nanotubes. *Nano Letters* **8**, 26-30, doi:10.1021/nl0716451 (2007).

38 Marquardt, C. W. *et al.* Electroluminescence from a single nanotube-molecule-nanotube junction. *Nat Nano* **5**, 863-867, doi:http://www.nature.com/nnano/journal/v5/n12/abs/nnano.2010.230.html#supplementary-information (2010).

39 Lee, C. Y., Baik, S., Zhang, J., Masel, R. I. & Strano, M. S. Charge Transfer from Metallic Single-Walled Carbon Nanotube Sensor Arrays. *The Journal of Physical Chemistry B* **110**, 11055-11061, doi:10.1021/jp056425v (2006).

40 Wang, J. Carbon-Nanotube Based Electrochemical Biosensors: A Review. *Electroanalysis* **17**, 7-14, doi:10.1002/elan.200403113 (2005).

41 Diehl, M. R. *et al.* Single-Walled Carbon Nanotube Based Molecular Switch Tunnel Junctions. *ChemPhysChem* **4**, 1335-1339 (2003).

42 Meng, S., Maragakis, P., Papaloukas, C. & Kaxiras, E. DNA Nucleoside Interaction and Identification with Carbon Nanotubes. *Nano Letters* **7**, 45-50, doi:10.1021/nl0619103 (2006).

43 Huang, S. *et al.* Identifying single bases in a DNA oligomer with electron tunnelling. *Nat Nano* **5**, 868-873, doi:http://www.nature.com/nnano/journal/v5/n12/abs/nnano.2010.213.html#supplementary-information (2010).